"Sapienza" University of Rome

Transport in complex flows: reactive, multiphase and supercritical jets

XXIV ciclo

Ph.D. student: *Francesco Battista*

Theoretical and Applied Mechanics

Tutor: *Prof. C. M. Casciola* Docente guida: *Dott. F. Picano*

To my girlfriend
and
my family

Abstract

The present work deals with the dynamics of turbulent jet in different configurations and geometries. In particular two aspect, important both in the engineering applications and in the scientific research, are stressed. The first one deals with the mixing in the turbulent jets at near-critical thermodynamic conditions. The second addresses the dynamics of inertial particle in turbulent premixed Bunsen flames. In order to perform a Direct Numerical Simulation (DNS) of a turbulent jet at supercritical conditions a suitable method was developed to mimic the gas thermodynamic behavior. The Van der Waals equation of state has been chosen and an Low Mach number expansion of Navier Stokes equations has been performed. This approach is completely original in the context of real gas equation, and it is considered as useful as the whole Navier Stokes system in the fully compressible formulation especially at very Low Mach number. The new equations are implemented in a numerical code in order to perform the first, in our knowledge, DNS of a fully turbulent coaxial jet in supercritical thermodynamic conditions. The configuration adopted is similar to the coaxial injectors of the liquid rocket engines and consists in an inner jet with liquid-like density and low velocity and in an outer jet characterized by a gas-like density and high velocity. Aim of the simulation is to observe high-density finger-like structures observed in previous experimental visualizations, the so-called "ligaments", and to understand the mechanism of their formation. In particular these finger-like structure formation is ascribed to the joint effects of the jet dynamics and the thermodynamics condition. In fact the Kelvin-Helmholtz structures, which generates by the peculiar jet configuration, contributes to the "ligaments" formation while the thermodynamic conditions allow these high-density structures to persist in low-density field. In the real gas jet the interface between the high and low density fluid is observed to be thinner than the perfect gas jet, hence the diffusion occurs at smaller and smaller scales. The obtained data are considered useful for the study of the mixing and combustion processes in the near critical conditions. In the LES/RANS context, in addition, DNS data are necessary for the evaluation of sub-grid terms and for development of new models. The dynamics of the inertial particles in turbulent premixed flame is addressed with the same code. The DNS of a reactive Bunsen jet laden with inertial particle is performed. The simulation reproduces a lean Methane/Air premixed flame in the "flamelet" regime. The flow is seeded with four particle population of different inertia with the mass density much larger than the fluid one and diameter much smaller than the Kolmogorov length scale. In these conditions, the particle dynamic equation is forced by only the Stokes drag and the one-way coupling regime can be assumed (no fluid-particle or particle-particle interaction occur). A suitable Stokes number is defined as a function of the particle features and of the laminar flame speed and thickness and burned/unburned gas temperature ratio. It is shown that the so-defined "flamelet" Stokes number is the suitable to describe the particle dynamics in the premixed flames. The DNS data are analyzed to address the effects of particle inertia on Particle Image Velocimetry measurements, in particular is observed that the particle inertia induces a time lag in particle to follow the

fluid acceleration across the flame front. This time lag generate a mismatch in the prediction of fluid velocity through the particle velocity. It is shown that the evaluation of high order velocity statistics needs particle with smaller and smaller flamelet Stokes number. The data are analyzed also to address the effects of the interaction between particle inertia and fluctuating flame front on the particle spatial distribution. Two statistical tools are used to this purpose, the Clustering Index, K, and the radial distribution function, $g(r)$. K measures the departure of the actual distribution from the Poissonian distribution, $g(r)$ is the probability to find a couple of particle at a certain distance r. An important outline consists in the presence of particle clusters in the flame brush. In particular also quasi-Lagrangian particles are characterized by not Poissonian spatial distribution as a consequence of the intermittent fluctuation of the instantaneous thin flame front separating two regions with different particle concentration. With the increasing of the Stokes number the cluster intensity increases experiencing a maximum value for order one flamelet Stokes number. All results concerning the particle dynamics are confirmed by experimental measurement on a Bunsen Methane-Air turbulent reacting jet. The obtained results are considered important both for experimental measurements and for soot dynamics and growth strongly influenced by the interaction of particle with the flame front and by their collision.

Contents

List of Figures

Publications

Peer-reviewed Publications

1. *I*ntermittent features of inertial particle distributions in turbulent premixed flames, F. Battista, F. Picano, G. Troiani and C.M. Casciola, Physics of Fluids, 23, 123304, (2011)

2. *Dynamics of PIV seeding particles in turbulent premixed flames.* F. Picano, F. Battista, G. Troiani, and C.M. Casciola, Experiments in Fluids, 0723-4864 **50**, 75-88, (2011)

3. *Particle clustering in turbulent premixed flames*. F. Battista, F. Picano, G. Troiani and C.M. Casciola. Journal of Physics: Conference Series, 33,012002 (2011) Particles in turbulence 2011 International Conference on Fundamentals, Experiments, Numeric and Applications, Potsdam (Germany), 16-18 March 2011.

4. *Bubble-Turbulence Interaction in Binary Fluids*. F. Battista, M. Froio, F. Picano, P. Gualtieri and C.M. Casciola. Advances in Turbulence in the Journal of Physics: Conference Series, in press. Proceedings of European Turbulence conference 13, Warsaw (Poland), 12-15 september 2011.

5. *Transport of inertial particles in turbulent premixed jet flame*. F. Battista, F. Picano, G. Troiani and C.M. Casciola. Advances in Turbulence in the Journal of Physics: Conference Series, in press. Proceedings of European Turbulence conference 13, Warsaw (Poland), 12-15 september 2011.

International and National Conferences

1. *Vorticity Induced Anomalous Effects in Particle Laden Flows* . Casciola C and Battista F. and Sardina G and Picano F and Troiani G and Gualtieri P and Piva R, Proceedings of 5th International Conference on Vortex Flows and Vortex Models, San Leucio, Caserta, Italy, 7 - 10 November 2010.

2. *Inertial particle dynamics in turbulent premixed flames.* F. Battista, F. Picano, G. Troiani and C.M. Casciola, Proceedings of 7th International Conference on Multiphase Flow, ICMF 2010, Tampa, FL, USA, 30 May - 4 June 2010.

3. *Turbulent premixed flame with dispersed inertial particle.* F. Battista, F. Picano, G. Troiani and C.M. Casciola, Proceedings of Euromech Fluid Mechanic Conference 8, Bad Reichenhall (Germany), 13-16 september 2010,

4. *Effects of particle inertia on PIV measurements of turbulent premixed flames*. F. Battista, F. Picano, G. Troiani and C.M. Casciola, Proceedings of 6th International Symposium on

Turbulence, Heat and Mass Transfer, THMT09, Rome (italy), 14 - 18 September 2009. ICHMT DIGITAL LIBRARY ONLINE.

5. *E*ffects of particle inertia on PIV measurements of turbulent premixed flames F. Battista, F. Picano, G. Troiani, C.M. Casciola Atti del XIX Congresso Nazionale AIMETA. Ancona (ITALIA), Settembre, ISBN: 9788896378083, (2009).

Articles in Book Chapter

1. *Inertial particles in turbulent premixed Bunsen flames*. F. Battista, F. Picano, G. Troiani and C.M. Casciola. Proceedings of Interdisciplinary Turbulence Initiative (ITI) conference on turbulence 4, Bertinoro (Italy), 19-23 september 2010.

2. *DNS of variable density jet in the super-critical thermodynamic state.* F. Battista, F. Picano, G. Troiani and C.M. Casciola, Proceedings of Direct and Large-Eddy Simulation VIII, 303–308 (2011) Springer.

Chapter 1

Introduction

Canonical turbulent jets are studied in a number of researches, both for their wide application in engineering and for their importance in turbulence theory comparable to that of homogeneous flows or boundary layers. In many applications, however, the structure of a jet is influenced by thermodynamic conditions, by the presence of dispersed liquid or solid phases, by chemical reactions or phase changes. Despite their relevance these complex jets, such as particle-laden, two-phase, reactive jets or cryogenic jets present yet several non clear features that need to be further investigated. In fact turbulent "complex" jets are characteristic of many engineering applications where a deepened understanding of their behavior is certainly necessary, given the substantial differences with the known dynamics of the canonical case. In this vast context, the attention is here focused on two prototypal cases namely a reactive jet seeded with inertial particles, and a supercritical turbulent jet discharging into a high pressure environment.

The particle-seeded, reacting turbulent jet is addressed by means of a Direct Numerical Simulation (DNS) of a cylindrical turbulent jet reproducing a Bunsen premixed lean methane/air flame and by experimental PIV/OH-LIF measurements. The flow is seeded with inertial particles mimicking Alumina particles like those usually employed in Particle Image Velocimetry (PIV). Actually, particle inertia is crucial in PIV measurements of reacting flow, where it may strongly affect the accuracy of the measurement in the region of the flame.

In a reacting jet the abrupt acceleration induced by heat release due to the combustion leads to the particle density decreasing across the flame. Besides, depending on their inertia, the particles follow the fluid acceleration with a certain time lag, quantified by the particle relaxation time τ_p which depends on particle size and mass density. The proper parameter to study the dynamics of the particles in these conditions is found to be the *flamelet Stokes number*, $St_{fl} = \tau_p/\tau_f$ which compares the smallest characteristic time scale of the flow τ_f – determined by the thermo-chemical characteristics of the flame – with the particle relaxation time τ_p. When the particles are used to check more delicate aspects of the flow, like for getting information on flame-conditioned fluid velocity fluctuations, the limit on the *flamelet Stokes number* becomes extremely stringent to the point that the particle may get so tiny to reach the limit where thermophoresis – defined as transport induced by thermal gradients – may be significant.

The flame induced turbulent dynamics of the particles is characterized by rather peculiar particle distributions. Recently, the issue of the anomalous spatial arrangement of inertial particles has been studied in a certain detail for simple incompressible flows. They are known to accumulate in intermittent aggregates, the clusters, which are separated by voids. The typical dimensions of the clusters depend on the characteristics of the turbulent field and on the parti-

cle inertia. For the present case, we were interested in understanding how the fluctuating flame front, across which the sudden fluid acceleration occurs, influences particle segregation. Two different phenomena emerged. The first one occurs also for the quasi Lagrangian particles with vanishing inertia and is due to the intermittent instantaneous fluctuation of the thin flame front separating the unburned and burned regions with different particle concentration. The second one is the actual formation of clusters due to the interaction of the wrinkled turbulent flame front with the particle inertia. Though aimed at the fundamental understanding of particle dynamics in a turbulent flame, the results we found are noteworthy and may be of interest for studying soot growth in order to understand the mechanisms of pollutant emission and for addressing accuracy issues in optical techniques for fluid flow measurement in combustion.

Concerning the cryogenic jet, the influence of the thermodynamic conditions on the jet behavior is addressed again by means of a Direct Numerical Simulation. As shown in the literature through experimental analysis, the thermodynamic state close to the critical point has strong influence on the dynamics of turbulent mixing which changes considerably with respect to both the classical cases of completely gaseous and liquid jets. Actually the supercritical state, which in a sense combines liquid and gaseous features, is observed to promote the formation of high density 'ligaments' which persist in low density regions. Such persistence is explained by the absence of the strong diffusion pertaining to the gaseous phase and occurs without formation of droplets, typical of liquid jet break-up where the surface tension acts at the liquid/gas interface. In such conditions the mixing takes place by a slower diffusion process by which the persistent ligaments slowly mix to the lighter gaseous environment. In order to address this intriguing phenomenon by DNS, a suitable *Low Mach number* expansion of the Navier-Stokes equation had to be developed to take care of the proper set of thermodynamic equations (e.g. Van der Waals state equation) and transport properties (e.g. viscosity and thermal diffusion). The geometrical configuration reproduces, with strong simplifications, the main features of space propulsion coaxial injectors. A relatively slow, cryogenic (liquid-like, high density and low temperature) fluid is injected through the inner nozzle while a gaseous fluid is injected through the external annulus with higher velocity. The pressure of the external environment is such that the high density fluid is expected to be in a supercritical thermodynamic state. The fluid properties are selected to reproduce those of nitrogen, to allow comparison with the few available experimental results concerning supercritical cold mixing. 'Ligaments' are indeed observed in the numerical simulation, as expected from the experiments. The high velocity low density flow tends to stretch the inner high density fluid promoting the formation of the "ligaments". Due to the peculiar thermodynamic state, in which temperature gradient are smaller than density gradients, the thermal diffusion promoting the mixing is slowed down. 'Ligament' formation mechanisms and the detailed study of the correlation between their shape, dimension and the distribution and the fluid dynamic structures are the topic of work and will be discussed in the present thesis.

Part I

Theoretical background

In this part a general overview on the main phenomena involved in the "complex" jet dynamics is provided. The first chapter is dedicated to the turbulence theory, from the Richardson energy cascade to the Kolmogorov $K41$ theory. The second chapter deals with the thermodynamic features of the gases at high pressure and high density conditions at which the ideal gas model fails. In the third chapter the general theory of combustion is summarized with particular attention to the turbulent combustion. Then the classical theory of the incompressible ideal turbulent jet is presented. The last two chapters deal with the nowadays knowledge pertaining the supercritical liquid turbulent jets and the dynamics of inertial particle in turbulent premixed flames.

Chapter 2

Turbulence theory

Turbulence is a non stationary and complex phenomenon occurring in the fluid dynamics. The wake beyond a body, the flow in a combustion chamber or in the water pipe, the atmospheric and marine streams, the volcanic eruptions are all characterized by a fluid being in a turbulent regime.

We consider a fully turbulent flow with U_∞ and L the characteristic velocity and length scale respectively. The non dimensional number describing the fluid dynamics in this conditions is the Reynolds number, $Re_\infty = U_\infty L\rho/\mu$ (with U_∞, L and μ the fluid characteristic velocity, length and dynamic viscosity, respectively), defined as the ratio between the inertial and viscous effects.

In the 1922 Richardson was the first to provide a physical description of the turbulent flows [10]. He speculates that turbulent flows are characterized by the occurrence of eddies of different dimensions. The larger eddies are of ℓ_0 size and are characterized by a turn velocity $u_0 = u(\ell_0)$. The main idea is that these eddies are characterized by a large Reynolds number, of order of Re_∞, hence being the viscous effects negligible these eddies are unstable and break up into smaller and smaller eddies. This phenomenon is hence characterized by a transfer of energy from the larger to the smaller eddies. Actually the *energy cascade* continues until the eddies Reynolds number reaches small value hence the viscosity effects are significant and their dynamics is stable. In this condition, Reynolds number order unity, the molecular viscosity rules the eddy dynamics and produces the kinetic energy dissipation. The main idea of the Richardson theory is that the kinetic energy is introduced in the turbulent flow at large scale through the production mechanism, it is then transferred from large scale to smaller and smaller scales through non viscous processes. Richardson argued that the dissipation occurs at the smaller scales of the process where the viscous effects are important.

The Richardson theory provides a qualitative explanation of the turbulent phenomena, but does not allow to evaluate the dissipation length scale or the variation of the eddies characteristic velocity and time scales, $u(\ell)$ and $\tau(\ell)$ respectively, as a function of the length scale. A further improvement at the turbulence theory was provided by Kolmogorov in the 1941 [11, 12] when a quantitative approach to the turbulence phenomena was employed. Kolmogorov argued that since the large eddies are influenced by the boundary or initial condition of the flow, they are strongly anisotropic. The isotropy is reached at smaller scale during the scale-deceasing mechanism induced by the energy transfer to smaller and smaller scale. He introduced the length scale at which the anisotropy is lost and a sort of small scale isotropy is reached, ℓ_{EI}. In addition Kolmogorov argued that also the geometry information is included in the large eddies,

hence the mean flow field dynamics are lost at small scales. This means that the statistics of the small scales are universal, i.e. high-Reynolds turbulent flows at small scales are similar regardless the boundary conditions or the mean flow features.

The important assumption is that in the range $\ell < \ell_{EI}$, also called *universal equilibrium range* the energy cascade is influenced only by the rate of energy transfer T_{EI} from the large to the small scale and by viscous dissipation, represented by the kinematic viscosity ν. Since the intermediate scale are characterized by only the energy cascade, the dissipation rate at the smallest scale is determined by the transfer rate i.e. $\varepsilon \sim T_{EI}$.

In this framework the characteristic length, velocity and time scales can be defined using only the dissipation rate ε and the kinematic viscosity ν,

$$\eta \equiv \left(\frac{\nu^3}{\varepsilon}\right)^{1/4} \qquad u_\eta \equiv (\nu\varepsilon)^{1/4} \qquad \tau_\eta \equiv \left(\frac{\nu}{\varepsilon}\right)^{1/2}.$$

These are the so called Kolmogorov scales. The Kolmogorov scale η denotes the smallest eddy size, and in fact the Reynolds number based η equals the unity, $\eta u_\eta/\nu = 1$, consistently with the hypothesis that the energy cascade stops at the scales with high molecular viscosity influence.

Since the energy introduced in the turbulent flow through the large eddies is dissipated only by the smallest eddies, the dissipation rate can be defined as a function of the large scales features, $\varepsilon \sim u_0^3/\ell_0$. With this definition, it is possible to express the ratio between the smallest and largest scale features as a function of the Reynolds number,

$$\frac{\eta}{\ell_0} \sim Re^{-3/4} \qquad \frac{u_\eta}{u_0} \sim Re^{-1/4} \qquad \frac{\tau_\eta}{\tau_0} \sim Re^{-1/2}$$

From previous relations, we highlight that the ratios η/ℓ_0, u_η/u_0 and τ_η/τ_0 decrease with Reynolds increasing, i.e. once assumed a certain phenomenon, with its boundary conditions, hence fixing the largest scales, then the increase of the Reynolds number results in the formation of smaller and smaller eddies, i.e. η decreases. This means that at very high Reynolds number there are some scale which are much smaller than the larger scale ℓ_0 and much larger than the Kolmogorov scale, $\ell_0 \gg \ell \gg \eta$. In this framework the range $\ell < \ell_{EI}$ can be divided in the *inertial subrange* and the *dissipation range*. In the *inertial subrange* the statistics of turbulence are influenced only by ε or equivalently by inertial effects consisting in the energy transfer rate determined by the greatest scales, and is independent of ν. The previous definition of characteristic velocity and time scale is not appropriate for this range of scale due to the dependence on ν, hence new relations in term of ε and ℓ are necessary,

$$u(\ell) = (\varepsilon\ell)^{1/3} \sim u_0 \left(\frac{\ell}{\ell_0}\right)^{1/3} \tag{2.1}$$

$$\tau(\ell) = \left(\frac{\ell^2}{\varepsilon}\right)^{1/3} \sim \tau_0 \left(\frac{\ell}{\ell_0}\right)^{2/3} \tag{2.2}$$

This highlights that in the *inertial subrange* the velocity and time scale pertain to the vortices of ℓ size decrease as their value decreases. On the other hand the *dissipation range* is the only at which the dissipation occurs, in other words the dissipation scales are characterized by viscous

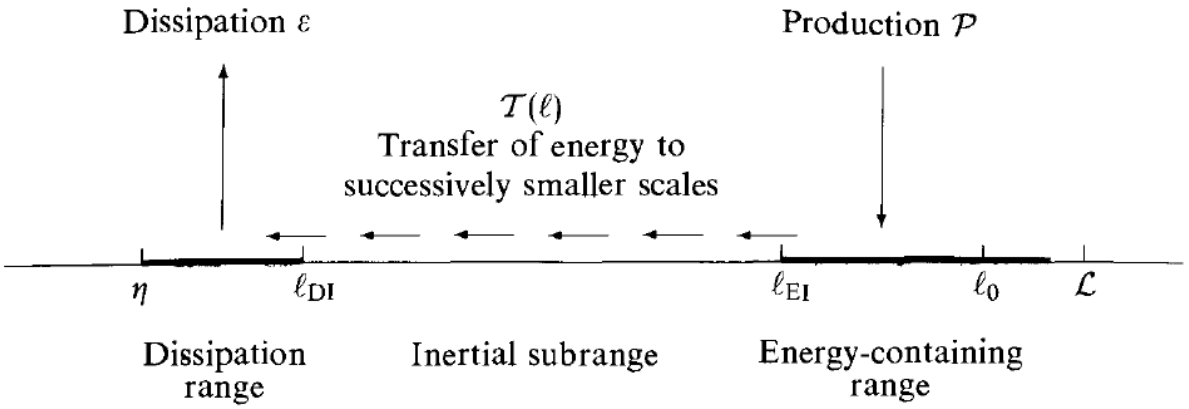

Figure 2.1 Diagram of the energy introduction, cascade and dissipation in a turbulent phenomenon at very high Reynolds number [1].

effects non negligible with respect to the inertial ones. The length scale ℓ_{DI} is the boundary between the *inertial subrange* and the *dissipation range*.

Figure 2.1 provides a diagram of the energy cascade at high-Reynolds number. Actually, the bulk of the energy is contained at the large scales where the energy is introduced in the turbulent flow. Through the mechanism physically explained by Richardson, the energy is transferred at the smaller and smaller scale in the *inertial subrange*. This energy transfer occurs until the viscous effects become significant: the *dissipation range* in this context results to be the only range of scales at which the energy is dissipated.

Here we have recall the main results on the turbulence provided first by Richardson and secondary Kolmogorov. In particular, the Kolmogorov theory here presented is based on two similarity hypotheses, the first is on the small scale motion isotropy in the *universal equilibrium range* and the second is on the dependence of the *inertial subrange* scale only on the energy transfer rate. The complete theory developed by Kolmogorov can be found in [1, 11, 12].

Chapter 3

Thermodynamics of real gas

Although the "perfect gas laws" do a remarkably good job of describing the behavior of a large number of substances as they exist in the gaseous state under ordinary environmental conditions, roughly around $1atm$ pressure and a temperature of $300K$, the ideal gas model have to be abandoned in order to explain such properties as

- the average distance between colliding molecules (the molecules really do take up space!),
- the high-pressure and low-temperature thermodynamic conditions characterized by the increase of intermolecular attractions;

Under ordinary environmental conditions (moderate pressures and above 0^oC), the isotherms of gaseous substances do not appear to differ very greatly from the hyperbolic form

$$\frac{pv}{\mathcal{R}\vartheta} = constant\,, \tag{3.1}$$

where p,v, ϑ are the pressure, the volume and the temperature of the gas, respectively, while R is the universal gas constant equal to $\mathcal{R} = \forall.\exists\infty\triangle\mathcal{J}\mathcal{K}^{-\infty}\Updownarrow\updownarrow^{-\infty}$. On other hand over a wider range of conditions, the fluid thermodynamic behavior begins to get more complicated. To extend the usefulness of the perfect gas equation of state over a greater range of temperatures and pressures, more phenomena should be considered.

Boyle's law prescribes that the product pv is a constant at any given temperature. This implies that any increase in the pressure of the gas is exactly counteracted by a decrease in the volume as the molecules are crowded closer together. This phenomenon is counteracted by the finite volume of particles hence a lower limit on the volume into which they can be squeezed exists. In this framework Boyle's law is valid only in the negligible pressure limit while under high pressure conditions both repulsive and attractive intermolecular forces become important:

- Repulsive forces: as a gas is compressed, the individual molecules begin to interact, giving rise to a very strong repulsive force, which acts to oppose any further volume decrease.
- Attractive forces: while at very close distances, all molecules repel each other as their electron clouds come into contact, at greater distances, brief statistical fluctuations in the distribution of the electron clouds give rise to a universal attractive force between all molecules. The more electrons in the molecule (and thus the greater the molecular weight), the greater is this attractive force. As long as the energy of thermal motion dominates this attractive force, the substance remains in the gaseous state, but at sufficiently low temperatures the attractions dominate and the substance condenses to a liquid or solid.

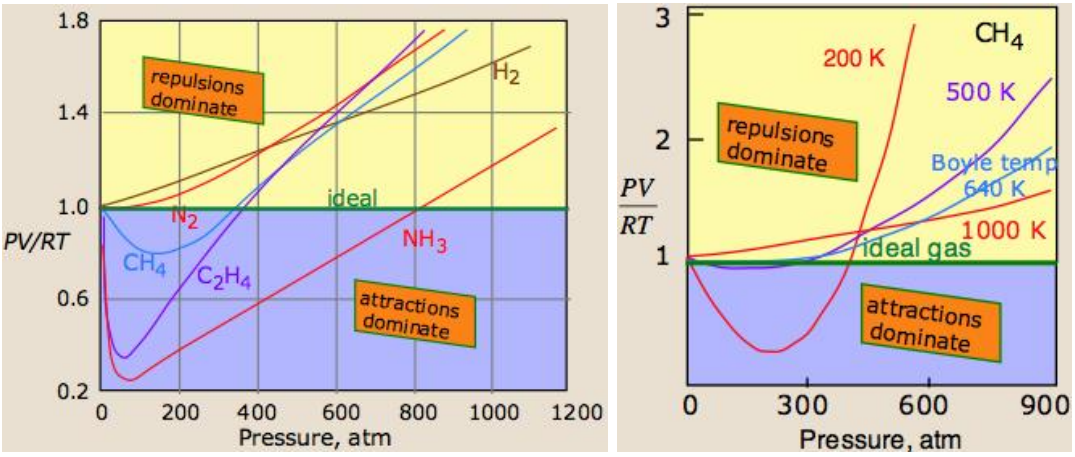

Figure 3.1 Variation of $PV/\mathcal{R}\vartheta$ as a function of pressure parametrized with chemical element, left panel, and temperature, right panel.

The universal attractive force described above is known as the dispersion, or London force.

The ratio of equation (3.1), constant for a perfect gas, depends on the temperature and the nature of the element considered, namely the physical dimension and molar weight, for a real gas. The plot of $Pv/\mathcal{R}\vartheta$ as a function of pressure is a very sensitive indicator of deviations from perfect gas behavior, since such a plot is just constant for an perfect gas, see figure 3.1.

Intermolecular attractions, which generally increase with molecular weight, cause the pv product to decrease as higher pressures bring the molecules closer together and thus within the range of these attractive forces: the volume decreases more rapidly than in the ideal gas case. On the other hand as the molecules begin to be very close, the stronger repulsive forces cause the curve to bend upward.

Also the temperature influences the real gas behavior; right panel figure 3.1. At higher temperatures, increased thermal motions overcome the effects of intermolecular attractions which normally dominate at lower pressures. So, all gases behave more ideally at higher temperatures.

The overall behavior of general chemical species at different pressures, temperatures and volumes is summarized in the phase diagram. The phase diagram is a 3D plot of the occurrence of distinct thermodynamic phases; see figure 3.2. The plot 3.2 highlights particular fluid thermodynamic states. The green zone, called condensation region, marks the conditions under which multiple phases equilibrium occurs and at which phase transitions occur. The solid lines are the isothermal plots experiencing a constant pressure in the condensation region. The critical isotherm which separate gas/liquid and supercritical fluid conditions is highlighted. The critical point, marked in figure, is a peculiar thermodynamic condition characterized by a non-analytic free energy relation. In particular the free energy derivatives with respect to temperature or pressure present a discontinuous behavior [13, 14]. The *critical point* represents the "limit" of the liquid-gaseous transition line, that is the projection of the condensation region on the $p - \vartheta$ plane.

As a matter of fact, at very high pressure and temperature above the critical point, the difference between liquid and gaseous phase vanishes and the fluid becomes the so called supercritical fluid.

The critical thermodynamic state, in particular, is characterized by peculiar features that influence the fluid behavior both in physical and chemical field. The first observation is that it is possible to obtain the phase transition crossing the liquid-gas line or experiencing the path

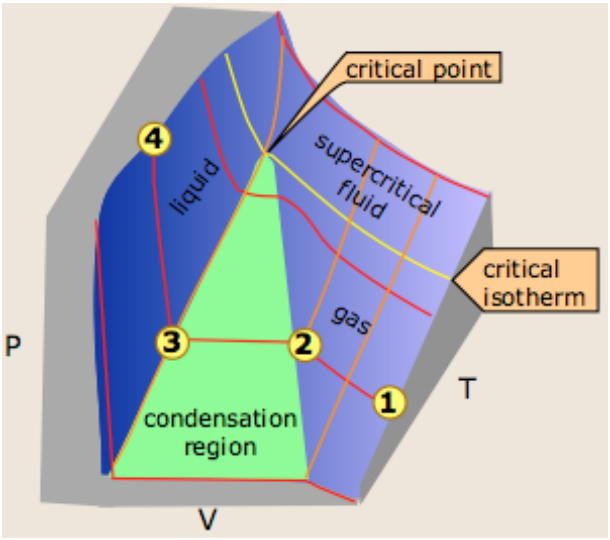

Figure 3.2 Phase diagram of a generic fluid in the pressure-volume-temperature space. Red lines: isotherm, yellow line: critical isotherm.

through the supercritical fluid on the right of the critical point. Actually, under subcritical pressure conditions the liquid-gas interface exists due to the surface tension, hence crossing the liquid-gas coexistence line the phase transition occurs. In the supercritical pressure conditions there is not a precise transition point because liquid and gas can blend continuously into each other.

Near the critical or the transcritical condition, fluids exhibit large variation in thermodynamic and transport properties, in particular they suffer strong variation in density, viscosity and thermal conductivity with temperature at constant pressure, while the heat capacity becomes very large being mathematically infinite at critical point. Moreover liquid-like density and gas-like diffusion coefficients are observed.

In these cases, the hypothesis of ideal gas is not suitable to modeling the thermodynamic behavior of fluid, so it is necessary to introduce an equation of state that reproduces the feature of the fluid in the transcritical conditions. Beginning in the 70s, the increasing interest in the supercritical fluid led to researches improving equations of state to better model the fluid behavior, in particular near the critical point.

The equations proposed to improve models dealing with thermodynamic fluid behavior are presented in the following sections.

3.1 Van der Waals equation

The Van der Waals equation of state reads:

$$p = \frac{\rho \bar{R} \vartheta}{1 - b'\rho} - a'\rho^2 \,, \tag{3.2}$$

where p, ρ and ϑ are pressure, density and temperature, respectively, while $\bar{R} = \mathcal{R}/\mathcal{M}$ is the ratio between the ideal gas universal constant ($\mathcal{R} = 8.314 J/(mol\, K)$) and the molar mass of the considered gas $\mathcal{M}$ and $a' = a/\mathcal{M}$ and $b' = b/\mathcal{M}$ where "a" and "b" are substance-specific constants. They can be calculated from the critical properties ρ_c, ϑ_c and p_c as:

$$a' = 3\frac{p_c}{\rho_c^2} = \frac{27(\bar{R}\vartheta)^2}{64 p_c} \qquad b' = \frac{1}{3\,\rho_c} = \frac{0.125\bar{R}\vartheta}{p_c}. \tag{3.3}$$

Van der Waals proposed equation (3.2) in (1873). Equation (3.2) was one of the first to include phenomena omitted by the perfect gas law. Two coefficients introduced in the equations taking into account two new phenomenologies: a' measures the attraction force between fluid particles, and b' is the so-called "excluded volume" i.e. real volume occupied by particles that becomes non negligible at high pressure and density.

All the following equations can be seen as an improvement of Van der Waals' equation of state (EOS), hence they are all obtained by the Van der Waals EOS including the dependence on the temperature or/and density of the Van der Waals constant. These equations differ from Van der Waals' equation, which has a rigorous derivation from statistical mechanics [13], because of their semi-empirical nature.

3.2 Soave-Redlich-Kwong equation

The Soave-Redlich-Kwong was introduced by Redlich-Kwong in the (1949) [15] and modified in (1972) by Soave [16],

$$p = \frac{\rho\bar{R}\vartheta}{1 - b'\rho} - \frac{a'\,\alpha(\omega,\vartheta)\,\rho^2}{1 - b'\,\rho}\,, \tag{3.4}$$

the additional parameter $\alpha(\omega,\theta)$ is included to improve the prediction of the mixture properties [17] and reads

$$\alpha = \left\{1 + \left(0.48 + 1.574\omega - 0.176\omega^2\right)\left[1 - \left(\frac{\vartheta}{\vartheta_c}\right)^{0.5}\right]\right\}. \tag{3.5}$$

ω is the *acentric factor* introduced by Pitzer in (1955) [18] and provides a measure of the non-spherical shape of the molecules. Coefficients "a" and "b" computed as a function of the critical quantities read as

$$a' = \frac{0.42748(\bar{R}\vartheta)^2}{p_c} \qquad b' = \frac{0.08664\bar{R}\vartheta}{p_c}. \tag{3.6}$$

$$\tag{3.7}$$

The Soave-Redlich-Kwong state equation is found to be very useful in the prediction of the pure fluid or mixture thermodynamic behavior, particularly in the supercritical region while it performs poorly with respect to the liquid phase and thus cannot be used for accurately calculating vapor-liquid equilibrium.

3.3 Peng-Robinson equation

The Peng-Robinson equation was developed in (1976), see [19],

$$p = \frac{\rho \bar{R} \vartheta}{1 - b' \rho} - \frac{a' \, \alpha(\omega, \vartheta) \, \rho^2}{1 + 2b' \, \rho - b'^2 \, \rho^2} \,, \tag{3.8}$$

In this case the coefficients a', b' and α read, respectively, as

$$a' = \frac{0.457235(\bar{R}\vartheta)^2}{p_c} \qquad b' = \frac{0.077796 \bar{R} \vartheta}{p_c} \tag{3.9}$$

$$\alpha = \left\{ 1 + \left(0.37464 + 1.54226\omega - 0.26992\omega^2\right) \left[1 - \left(\frac{\vartheta}{\vartheta_c} \right)^{0.5} \right] \right\} . \tag{3.10}$$

The present state equation ensures a reasonable accuracy near the critical point, particularly for calculations of liquid density. For large range of temperatures and pressures the Peng-Robinson equation exhibits performance similar to the Soave equation, although it is generally more accurate in the prediction of the liquid densities of many fluids, especially non-polar ones.

Since thermodynamic conditions are proved to have strong influence on the fluid behavior and on the structures of the flows where real gas is employed, one of the previous equation of state should be used in the numerical simulation. Although the Van der Waals' equation is nowadays obsolete and is not considered the best equation to model the fluid behavior in the supercritical conditions, in this work the Van der Waals' equation is used. The main reason is that the Van der Waals' equation provides reasonable results while it displays the analytical simplicity. Moreover, unlike the Soave-Redlich-Kwong and Peng-Robinson equations, it has a rigorous derivation from the statistical mechanics [14] providing analytical relations for enthalpy, internal energy and specific heat coefficients. The very simple analytical form is useful for the *Low Mach number expansion*, as proved in the Results part.

Chapter 4

Reactive flow: combustion

Combustion is a chemical reaction occurring between oxygen and fuel and producing an intense heat release. The complexity of the detailed combustion mechanism implies that in practical calculations one must use simpler but still chemically realistic models. Considering the most simple reaction, i.e. hydrogen-oxygen, the detailed simulation of chemistry coupled with the fluid dynamics without turbulence model is very CPU time expensive. In this context, reduced mechanisms are then necessary, hence in last decades numerous methodologies for chemical kinetic reduction were employed to obtain suitable models for different thermodynamic conditions.

Two typical regimes can be distinguished: premixed flames, where a mixture of reactants burns in the combustion process and diffusive flames, where the combustion occurs depending on the mixing of reactants originally separated.

Figure 4.1 shows the conical characteristic shape of the laminar Bunsen premixed flame. Different zones can be distinguished in particular the burned and unburned regions separated by the thin premixed conical flame. The fresh mixture is discharged in the ambient where the

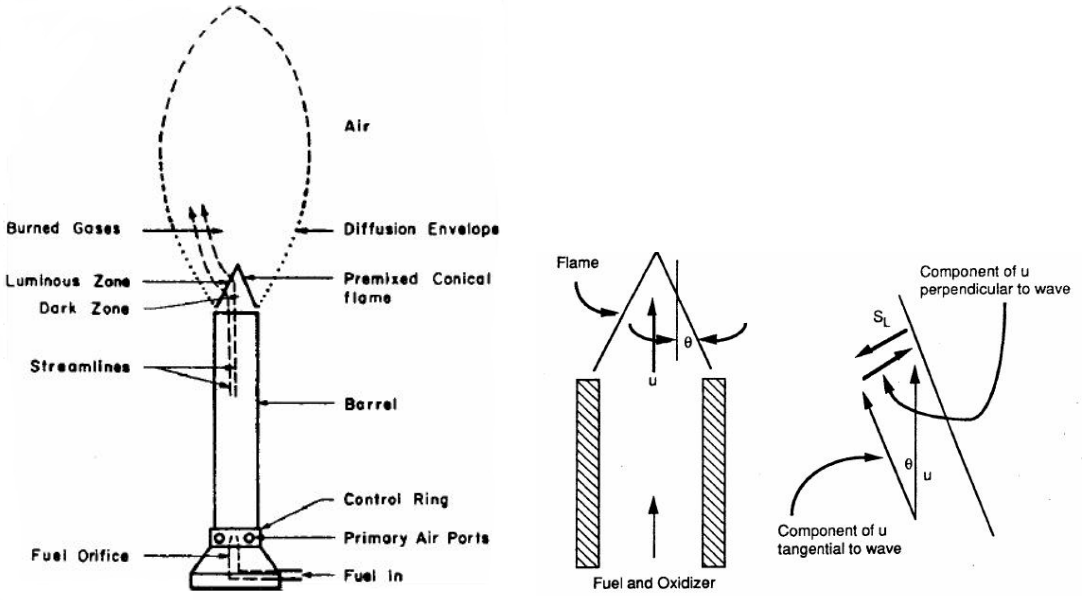

Figure 4.1 Schematic configuration of the turbulent premixed Bunsen flame. Left panel: experimental setup of Bunsen, with highlighted different flame regions, right panel: classical conical shape of laminar Bunsen flame with fluid velocity vector u, laminar flame velocity vector S_L and angle θ between mixture flow and flame front.

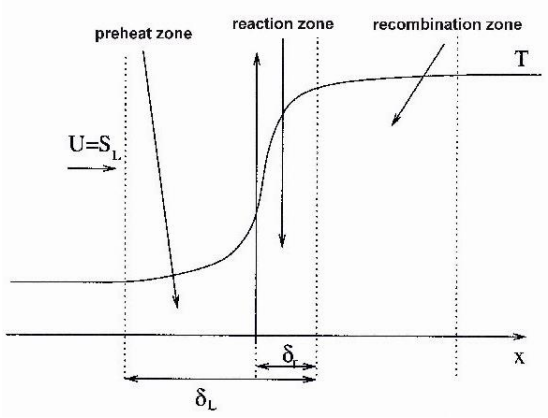

Figure 4.2 Laminar flame structure with highlighted the preheat, reaction and recombination regions. δ_L and δ_r are the laminar flame and reaction zone thickness, respectively.

combustion process occurs across the flame, right panel of figure 4.1. In the laminar configuration the combustion speed S_L can be calculated in relation with the inlet fresh mixture velocity u and the angle θ of the conical shape,

$$S_L = u \, \sin(\theta) \, .$$

To describe the combustion phenomena from the chemical point of view, the chemical reaction can be in general represented as,

$$\sum_{i=1}^{N} M_i \nu_i' \rightarrow \sum_{i=1}^{N} M_i \nu_i'' \tag{4.1}$$

where N is the number of chemical species involved in the reaction and ν_i' and ν_i'' are the stoichiometric coefficient of reactants and products, respectively. The main parameter of the chemical reaction is the production/consumption rate of the i-th species,

$$r_i = -k \prod_{i=1}^{N} [M_i]^{\nu_i'} \tag{4.2}$$

where the square bracket indicates the concentration of M_i and k is the reaction rate described by the Arrhenius law,

$$k = B\vartheta^{\alpha} \exp -\frac{E_a}{R\vartheta} \tag{4.3}$$

In the premixed laminar flame regime the region where the combustion occurs is the so-called flame front, and three different zones can be distinguished: the preheat, the reaction and the recombination zone; see figure 4.2. The preheat zone is characterized by the temperature of the reactants increase due to the heat coming from the reaction zone and by the formation of the radicals triggering the combustion. The reaction zone is the region where the actual chemical reaction, strong heat release and intense temperature gradient, occurs. The recombination zone is characterized by the formation of the chemical products by the radicals coming from the reaction zone.

Two important parameters are introduced to characterize the flame front: the laminar flame thickness, and the laminar flame speed. The laminar flame thickness is here defined as a function

of the temperature gradient,

$$\delta_L = \frac{\vartheta_b - \vartheta_u}{\nabla\vartheta|_{max}} \tag{4.4}$$

where the subscripts of ϑ stand for unburned 'un' and burned 'b' gas temperature. We highlight that this definition provided the smallest size prevision of the flame front size. The laminar flame speed S_L is the velocity of reactant consumption and is proportional to the thermal diffusion α and reaction rate k, $S_L = \sqrt{\alpha k}$.

4.1 Turbulent combustion

The characterization of turbulent combustion is mainly based on the comparison of turbulent scales with the typical scales of combustion. To this purpose two additional number are introduced, the Damköler and Karlovitz numbers. The former one is the ratio between the integral characteristic turbulent time and the chemical time (we highlight that the hypothesis of a global reaction ensures the presence of a unique chemical time). Defining the turbulent time as a function of the velocity fluctuation u' and the integral length scale ℓ_0, and the chemical time with the laminar flame speed and thickness, we obtain,

$$Da = \frac{\ell_0}{\delta_L}\frac{S_L}{u'}\,. \tag{4.5}$$

The Karlovitz number, which compares the chemical time scale τ_c with the Kolmogorov time scale τ_η, reads,

$$Ka = \frac{\tau_c}{\tau_\eta} = \frac{\delta_L}{\eta}\frac{u_\eta}{S_L}\,. \tag{4.6}$$

The flame/turbulence interaction exhibits different regimes in relation with the order of magnitude of the previous parameters; see figure 4.3. The different regimes were identified and rationalized by Borghi *et al.*; see [2, 3, 20] for detail. In particular, depending on the Karlovitz number they identify three fundamental regimes; figure 4.4: the wrinkled thin flame regime also called "flamelet", the thickened-wrinkled flame and the thickened flame. The flamelet regime is characterized by a locally laminar flame wrinkled by the turbulent vortices that do not influence the flame structures. The thickened-wrinkled flame occurs when the turbulent structures are small and strong enough to influence the preheat zone, but do not interact with the reaction region. The thickened regime consists instead in a flame completely changed by the turbulent vortices incoming in the reacting zone.

This classification comes from several hypotheses recently considered not necessary valid especially in the high Karlovitz number range. The turbulence is assumed to be not influenced by the heat release, while in recent studies turbulent fluctuation and anisotropy increase due to the combustion are observed. The influence of a 3D flame shape and anomalous diffusion phenomena, as occurring in the hydrogen-air combustion [3], are not considered. The assumption that the small scale structures of turbulence are able to penetrate the flame front reacting zone is in contrast with recent studies which demonstrate that their weakness due to viscous dissipation inhibits their effects on the flame front [21].

In this context we consider a simple global reaction, the reaction rate of which is modeled with the Arrhenius law. It is useful to define the instantaneous flame front which is the thin wrinkled region in which heat release occurs, and the "flame brush" i.e. the region spanned by the instantaneous flame front.

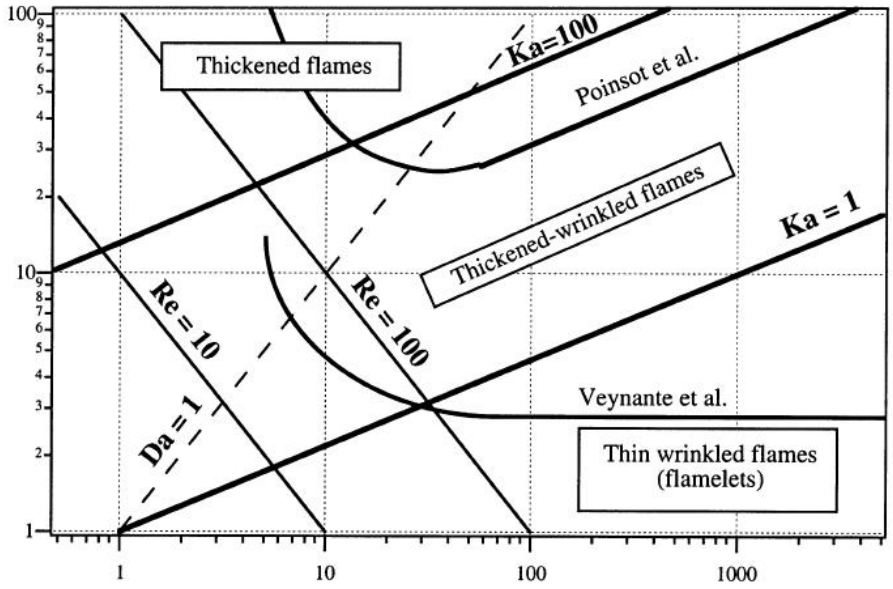

Figure 4.3 Borghi diagram [2] classifying the different flame regimes. abscissa axis: velocity fluctuation normalized with the laminar flame speed, u'/S_L, ordinate axis: fluid dynamics characteristic scale normalized with the laminar flame thickness. The figure is taken from [3].

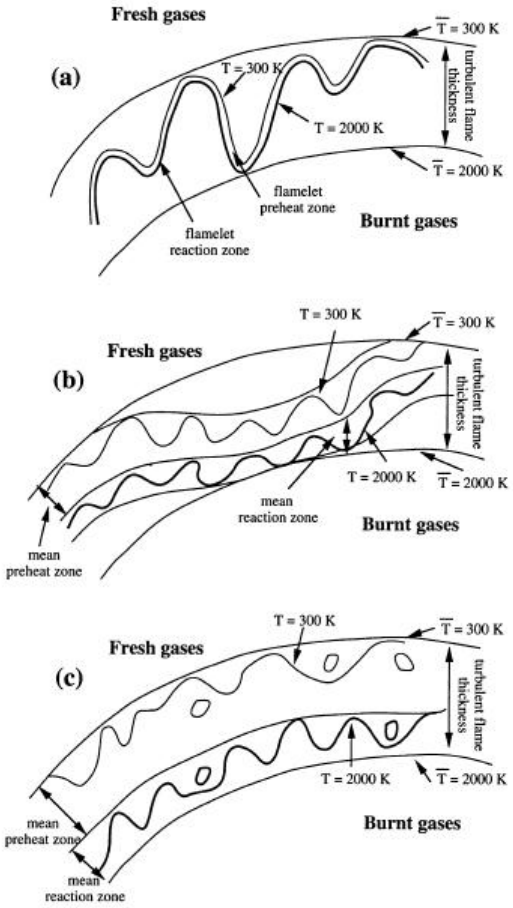

Figure 4.4 Turbulent instantaneous premixed flame regimes, classification provided by Borghi *et al.* [2]: (a) flamelet i.e. wrinkled thin flame (b) thickened-wrinkled flame (c) thickened flame. The figure is taken from [3].

Chapter 5

Turbulent free jets

Jet dynamics is the topic of several studies in the last decades because of its wide range of application in engineering devices and natural phenomena. Moreover, turbulent jet flow, homogeneous isotropic turbulence, homogeneous turbulent shear, turbulent pipe and channel flows are studied as fundamental flows. The turbulent round jet is a spatially evolving flow statistically stationary and axial-symmetric. An example of round free jet is provided in figure 5.1 where also the polar coordinate system is highlighted. As a matter of fact the only parameter characterizing the ideal jet behavior is the Reynolds number, defined as the ratio between the viscous and the convective force:

$$Re = \frac{U_{jet}\, D\, \rho}{\mu} \tag{5.1}$$

where U_{jet} is the mean velocity of jet inflow, D the jet diameter. Since the turbulent round jet is statistically stationary and axial-symmetric, the statistics only depend on the radial and axial coordinate, and velocities present some specific features: the mean axial velocity is greater than the mean radial one, $\langle u_r \rangle \ll \langle u_z \rangle$, while the mean circumferential velocity is zero, $\langle u_\theta \rangle = 0$. According to the axial velocity profile evolution in the streamwise direction, the incompressible jet dynamics can be divided in two parts: the near-field, $z < 25\, D$, where the axial velocity radial profiles are strongly dependent on the inlet conditions, and the far-field, $z > 30\, D$, where the memory of the inlet conditions is lost hence universal behavior is reached.

Starting from the mean axial velocity, $U_z(r, z) = \langle u_z(\theta, r, z; t) \rangle$, two important observables of

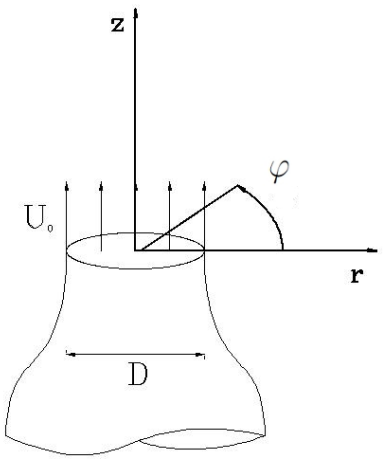

Figure 5.1 Experimental round-jet example, with spatial coordinate system: azimuthal θ, radial r and axial z coordinate. Figure taken from [4]

jet can be defined: the jet decay, which is the decrease of the centerline axial velocity, $U_c(z) = U_z(r = 0, z)$, and the half-width of jet $r_{1/2}(z)$, defined as the radial coordinate at which the mean axial velocity equals the half centerline speed,

$$U_z(r_{1/2}(z), z) = \frac{1}{2}U_z(0, z) = \frac{1}{2}U_c(z)\,. \tag{5.2}$$

Both experimental and numerical data confirm that in the far-field, the centerline velocity decays linearly with $1/z$ and the jet half-width is proportional to z. In particular the following relations are verified,

$$\frac{U_z(r, z)}{U_c(z)} = \frac{B\,D}{z - z_0} \qquad r_{1/2}(z) = (z - z_0)\,S \tag{5.3}$$

where z_0 is the virtual origin, while the constants B and S denote the decay rate and the spreading rate of jet, respectively.

In the far-field region, although the centerline velocity decays and the half-width increases, the shape of the axial velocity profile seems to be almost the same; see figure 5.2. To confirm the self-similar behavior, the quantity $U_z(r, z)/U_c(z)$ can be plotted as a function of radius normalized with the jet half-width, $r/r_{1/2}(z)$. In plot 5.3 it is shown that the profiles collapse on a unique function, hence the shape of velocity profile is not a function of the axial coordinate but depend only on the normalized radius.

The self-preserving behavior of the constant-density turbulent jet in the far field is a concept generally accepted. In fact, both experimental and numerical studies [22, 23, 24], demonstrated that mean, root mean square, and probability density function of passive scalar concentration follow similarity relations. An extensive overview on this self-similar behavior, also from the theoretical point of view, is provided in [1] with some experimental results showing the described behavior.

The important observation is that the spreading rate S and the centerline velocity decay B are not affected by the Reynolds number, as showed by experimental measurements. When increasing the Reynolds number the flow, smaller and smaller structures occur in all turbulent flows, but the mean axial velocity profiles and the spreading rate are independent on the Reynolds number.

5.1 Variable-density turbulent jet

The increasing interest on variable-density turbulent jets induces the researchers to look for a sort of self-similar law in the behavior of this more complex flow. *Richardson & Pitts* (1993) [25] stated that self-similar behavior can not be reached if the density variation across the flow is appreciable, because "self-presenting solutions do not exist for the governing equations". The explanation provided in [25] consists in the observation that when the density ratio is negligible the Bussinesq approximation allows to assume that only the buoyancy term is influence by the density variation. In these conditions the continuity and momentum Navier-Stokes equations coincide with the incompressible one plus the buoyancy term. They show that the far-field of slightly variable-density jet, in which buoyancy and coflow effects can be neglected, is essentially identical to the constant-density turbulent jet. They demonstrate the existence of self-similar behavior through the mean and root mean square of the passive scalar and the velocity, showing that centerline decay and spreading rates are independent on initial and inlet conditions.

Sauter & Stepowski (1995) [26] studied both experimentally and analytically the near-field of a variable-density turbulent jet in which buoyancy and coflow effects on jet structure are not

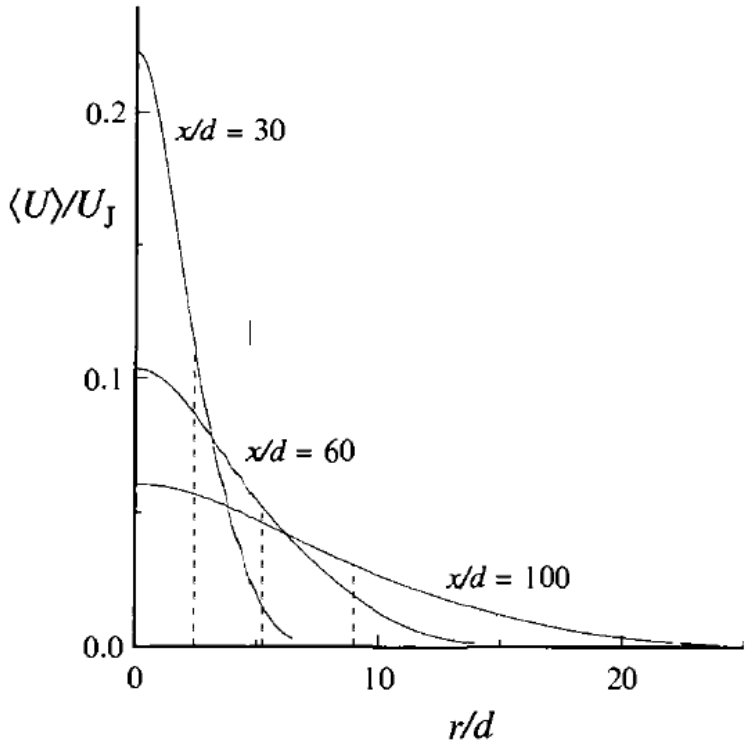

Figure 5.2 Radial profiles of the mean axial velocity $U_z(r, z)$ as a function of r/D of a round turbulent jet at $Re = 95500$. Dashed lines indicate the jet half-width $r_{1/2}(z)$ of profiles. The profiles are obtained by data provided by *Hussein et al.* [5]. Figure taken from [1].

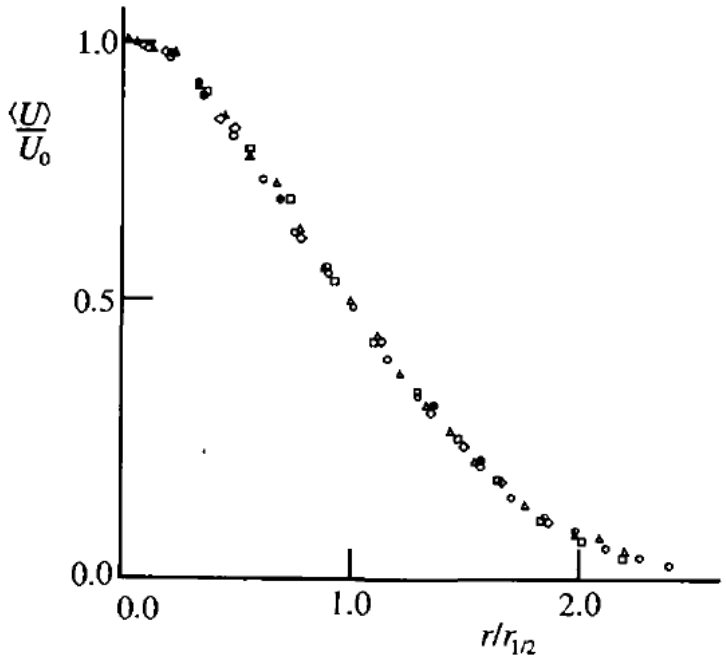

Figure 5.3 Radial profiles of the normalized mean axial velocity $U_z(r, z)/U_c(z)$ as a function of $r/r_{1/2}(z)$ of a turbulent round jet at $Re \sim 10^5$. Data are provided by experimental measurement of *Wygnanski & Fiedler* [6]. The symbols denote different axial distances. ○ : $x/D = 40$, △ : $x/D = 50$, □ : $x/D = 60$, ◇ : $x/D = 75$, ● : $x/D = 97.5$. Figure taken from [1].

negligible. They demonstrate the existence of a self-similar behavior through the use of a local effective diameter in which the local strong density ratio is taken into account. With a similar procedure used in the characterization of the incompressible turbulent jet, the effective diameter is defined using the momentum flux in order to normalize the centerline velocity decay and the length scales.

Chapter 6

Supercritical turbulent jets

Cryogenic rocket engines, advanced gas turbines and diesel engines are characterized by the injection of a liquid fuel into a high temperature and high pressure chamber. Typically, the fuel is injected at high enough pressure to be close or above the critical pressure. In these conditions the behavior of the fluid differs strongly from that of a perfect gas. It exhibits large variations of thermodynamic and transport properties for small temperature changes, with significant effects on mixing and combustion processes. In this context, an appropriate numerical simulation should take into account such thermodynamic phenomena through a suitable state equation and transport properties.

High pressure environments, characteristic of the combustion chamber, induce different evolution of turbulent variable-density jets. In particular, the thermodynamic conditions at which the reactants are injected in the combustion chamber and the injectors' geometry influence the mixing process and the combustion efficiency.

Modern engine injectors discharge high density fluid in high pressure environment. Under these conditions, the injected fluid experiences a pressure greater or smaller than its critical pressure, hence its supercritical or liquid phase, respectively.

The liquid injection occurs in particular in the gas turbines, reciprocating engines and liquid rocket engines before the ignition, when the pressure is low. Under these conditions the liquid jet breaks up in several droplets of various diameters evaporating in the air stream due to the high temperature produced by the combustion process [27, 28, 29]. The supercritical fluid occurs in particular after the ignition when the chamber pressure overcomes the critical one. Dealing with the liquid rocket engines, the reactants are injected through co-axial jets in the combustion chamber. Environment pressure is higher than the critical one hence one of the reactants experience its supercritical state. Actually for technical reasons both reactants, generally hydrogen H_2 or methane CH_4 and oxygen O_2, are stored in liquid phase. The oxygen is injected at supercritical state through the inner part of the co-axial injector and presents liquid-like density and gas-like viscosity and diffusion. On the other hand, since fuels are employed to cool the combustion chamber and nozzle walls, they are injected at low-density state through the outer jet. The supercritical jets are characterized by specific structures the dynamics of which strongly differs from the liquid jet breakup. The interaction between low-density and high density fluid induces the formation of high-density finger-like structures similar to those produced in liquid jets break up, the so-called 'ligaments'. At these thermodynamic since the distinction between liquid and gas phases disappears with the relative interface and surface tension, droplet formation is inhibited and ligaments disappear due to the turbulent and molecular diffusion.

The main effects of the environment pressure on the turbulent jet evolution is presented in figure 6.1 provided in [7]. Figure 6.1 shows images of a cold, $\theta \simeq 90 - 110\,K$, N_2 jet injected into warm N_2 at a fixed supercritical chamber temperature $\theta = 300\,K$ but at various pressures ranging above and below the critical pressure. The reduced pressures, $P_r = P_{chamber}/P_c$, shown in the figure caption, are given with respect to the critical pressure of the injectant (pure N_2) The images show a demarcation of regions where changes in the index of refraction occur due to density variations. At the lowest subcritical chamber pressure in figure 6.1, $P_r = 0.23$, the jet is liquid-like with surface instabilities that grow downstream to where it has a twisted appearance. At $P_r = 0.43$, all instabilities are further amplified until at $P_r = 0.63$ when many surface ligaments and drops are seen to be ejected from the jet. At $P_r = 0.83$, very fine drops are seen and the jet's spanwise dimension noticeably grows away from the injector exit plane (i.e., the jet diverges). At $P_r = 1.03$, the N_2 jet enters into a supercritical temperature and pressure environment and drastic changes in the details of the interface are seen. There are no detectable drops under this condition, even with the highest software magnification used to view these high resolution images. There are threader finger-like entities that emerge from the jet but are not broken up into droplets as before. They are seemingly dissolved at a spectrum of distances from the dark central core region. This, in a sense, forms a mixing layer in which phase transition and/or large local density nonuniformities occur. A further increase of the chamber pressure decreases the length and the thickness of the internal dark core, and images progressively resemble the injection of a gaseous turbulent jet into a gaseous environment (single-phase turbulent jet).

The supercritical behavior is described in several publication presenting both experiments and numerical simulations, in both reactive and non reactive flows.

An assessment of the state of the art up to 2000 is provided by *Yang* in [30]. In this field the injection of liquid jets in thermodynamic conditions close to the critical ones is the topic of both experimental papers [7, 31, 32, 33] and numerical simulations, in particular Large Eddy Simulation (LES) and Reynolds Averaged Navier-Stokes (RANS), [34, 35]. To our knowledge, the first Direct Numerical Simulations (DNS) in literature were performed and presented by *Bellan et al.* in [36, 37, 38, 39]. Several other studies address the influence of the thermodynamic conditions on the mixing process in gaseous and supercritical state or the occurrence of atomization and break-up of a liquid jets [40, 27].

Experimental studies [7, 31, 41] deal with the injection of a liquid nitrogen simple jet and of a liquid nitrogen and gaseous helium co-axial jet discharging both in an high pressure nitrogen environment. Shadowgraph images highlight strong changes in jet mixing mechanism with the increasing of the chamber pressure above the critical injected gases pressure. The break up of the ligaments into several droplets occurring in the subcritical thermodynamic conditions disappears close and above to the critical pressure. The jet in the supercritical state presents the same behavior of the variable density ideal gas jet [32] The less standard trans-critical injection of both reactants has also been investigated [41] emphasizing the effects on the combustion process. In the case where both reactants are trans-critical, the flame structure is strongly different compared to the characteristic injection of the liquid rocket engines. In fact, two flame fronts are apparent, one close to the liquid oxygen boundary and the other near the liquid methane one experimentally showed by two conical region of light emission. These experimental studies are useful both to understand the mixing process and to optimize the design of co-axial injectors.

In the same studies [7, 31, 32] the flame dynamics of co-axial injectors using liquid oxygen

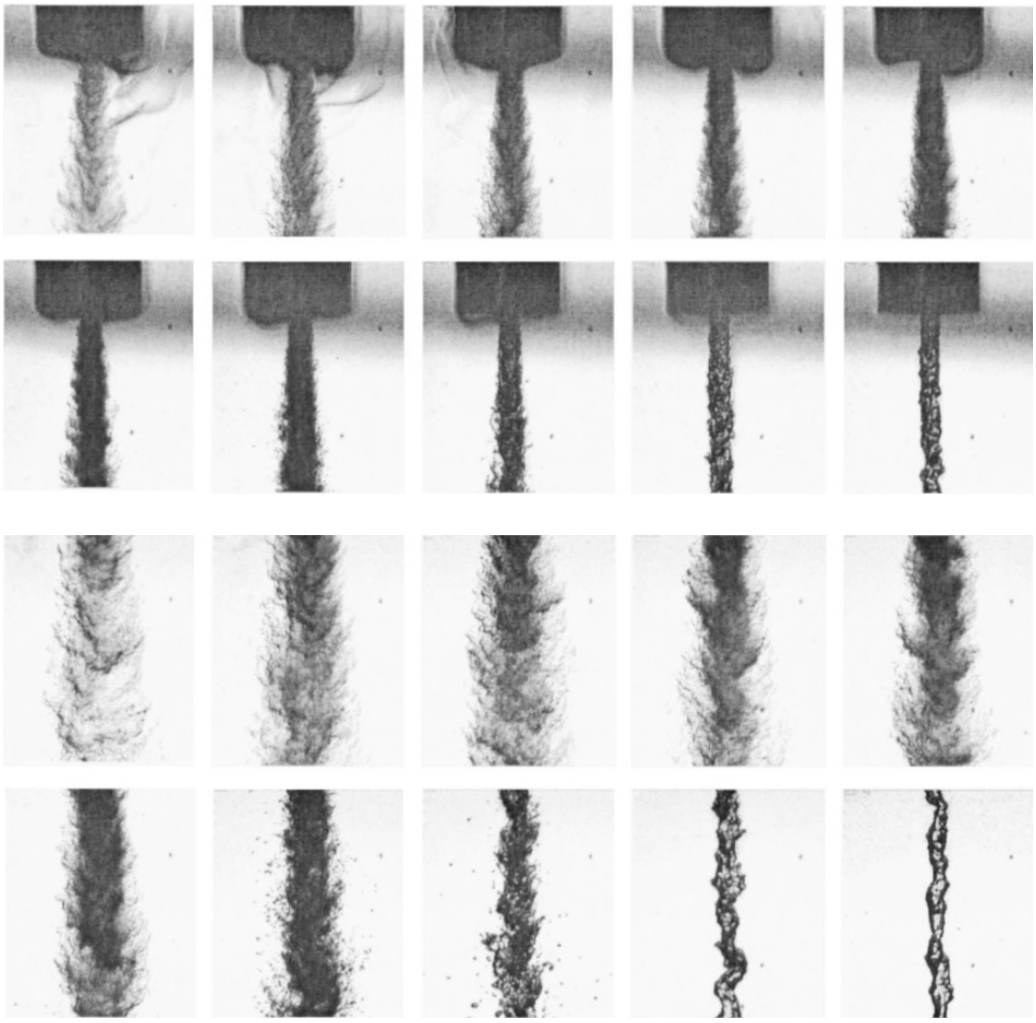

Figure 6.1 Experimental images of a turbulent jet at supercritical temperature, 300K, discharging in a nitrogen environment at different pressure. The first two rows are the near field the last two are the corresponding far field. From top-left to bottom-right the pressure is decreased from supercritical to subcritical pressure, in particular $P_r = P_{chamber}/P_c = 2.74, 2.44, 2.03, 1.64, 1.23, 1.03, 0.83, 0.63, 0.43 and 0.23$, respectively. For more detail see [7]

and gaseous hydrogen are systematically investigated. LES and RANS simulations are performed to study the influence of the geometry of injectors and mass flow ratio on the mixing process, combustion efficiency and flame stability. The sub-grid models for numerical simulation are validated ensuring the matching with the experimental results. The main issue in this context is the sub-grid models for the terms reproducing the specific thermodynamic conditions such as the equation of state and the specific transport properties such as viscosity and thermal diffusion. Although the sub-grid terms are expected to be relevant at high pressure conditions the presented simulations do not employ turbulence models [42]. DNS performed by *Bellan et al.* reproduces supercritical heptane/nitrogen [36, 37] and oxygen/hydrogen [39, 38] turbulent mixing layer. The effects of the specific thermodynamic state on turbulent mixing layer structures were investigated. The presented results are judged useful to develop proper models for turbulence phenomena influenced by real gas features. DNS data are also employed to evaluate models for sub-grid terms necessary for LES simulation [43, 44, 45, 46]. The authors identify additional sub-grid terms deriving by filtering momentum and energy equation. In these works the authors identifies additional subgrid terms by deriving the filtered momentum and energy

equations and analyzing their DNS database. The analysis shows that new terms are important in these equations due to the non linearity of state equation which leads to strong density gradients occurring in supercritical mixing layers.

Other numerical simulations concerning supercritical conditions address the effects on combustion of liquid oxygen and gaseous methane or hydrogen [35, 33]. The flame stability is stressed in order to optimize the injectors design to enhance mixing and combustion efficiency. The additional terms belonging from real gas state equation filtering, are not modeled.

Zong & Yang (2007) [30] perform the Large Eddy Simulation of the liquid oxygen and gaseous methane co-axial injector at supercritical pressure. They study the near-field mixing and combustion dynamics addressing the the flame-stabilization mechanism provided by the trailing edge of the two concentric tube of the injector. Due to the high density ratio between dense oxygen and gaseous methane, the chemical reaction is dominated by oxygen diffusion. The large vortices generated from the trailing-edge increase the reactants mixing. The effects of the momentum-flux ratio between oxygen and methane flows are investigated, obtaining a shortened oxygen jet potential core and an enhanced mixing process with the increasing of the methane momentum-flux.

Chapter 7

Particle dynamics in turbulent flow

Fluid/particle interaction consists in mutual forces between fluid and particle, in inter-particle collisions and interactions and in hydrodynamic coupling between particles. Depending on particle and flow features, different interactions can be neglected or should be considered if their effects are significant. If it is necessary to consider all effects, the model assumed for the numerical simulation is called four-way coupling [47, 48]. The model where inter-particle collisions and interactions are negligible is called the two-way coupling [47, 48]. While the simplest model is the one-way coupling regime in which only the fluid forces acting on particles are considered.

While in the unladen flow the only non-dimensional parameter used to characterize the fluid dynamics is the Reynolds number, in the particle laden flow three further parameter are introduced: the density ratio, the volume fraction and the Stokes number. The density ratio is obviously the ratio between the material density of the particles and fluid density ρ_p/ρ_f, which in the results presented in the following is considered of order of 10^3. The volume fraction, Φ, is the ratio between the volume of the two phase. The Stokes number is the ratio between the particle and fluid characteristic time $St = \tau_p/\tau_f$. While the fluid characteristic time depend on the flow features and on the faster fluid time scale occurring in the phenomenon [49, 50, 51], the particle characteristic time, also called relaxation time, depends on particle physical properties,

$$\tau_p = \frac{\rho_p}{\rho_f}\frac{d_p^2}{18\nu} \tag{7.1}$$

with ρ_p and d_p the particle density and the particle diameter (in this context particles are considered of spherical shape), and ρ_f the density of the carried fluid. The Stokes number is known to be the proper parameter to describe the particle dynamics. When $\tau_p \to 0$, hence $St \to 0$, the particle tends to follow all fluid fluctuation showing a Lagrangian tracer behavior. In this regime particles can be considered passive scalars without molecular diffusion. At the opposite limit $\tau_p \to \infty$, corresponding to $St \to \infty$, which is characterized by a ballistic behavior of particles not being influenced by fluid fluctuation. Intermediate values of Stokes number induce non trivial particle dynamics: they deviate from fluid trajectories and are ejected from vortex structures due to their inertia. In this last regime particles, depending on their relaxation time, tend to follow the slow fluid fluctuation and to filter the faster fluid structures, see figure 7.1.

These parameters influence the choice of the correct model for the numerical simulation of the particle laden flow. In particular, if the particle diameter is typically smaller than the Kolmogorov scale, the particles are assumed to be Lagrangian spherical points; on the other hand a fully resolved simulation is necessary if the particle diameter is comparable to the characteristic flow length scale, see [52, 53]. The volume fraction increase makes necessary the introduction

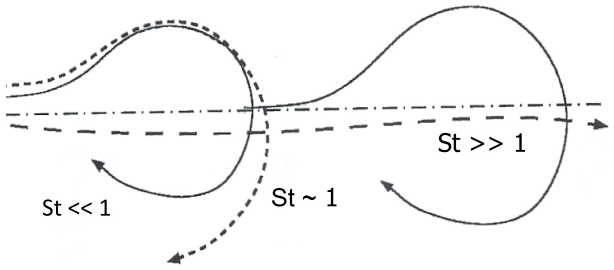

Figure 7.1 Particle behavior depending on Stokes number. Solid lines: fluid structures, dashed lines: particle trajectories

of particle collision and hydrodynamic interaction employing the two-way or four-way coupling model. In addition to address the effects of particle on fluid flow, i.e. turbulence modulation, two-way of four-way coupling are necessary.

In order to address the particle dynamics in a viscous turbulent flow, numerous models were developed for the dynamic equation of a rigid sphere, see [54, 55, 56]. The most commonly used today was developed by *Maxey & Riley* [57] in 1983, with the hypothesis of a rigid sphere in non-uniform flow,

$$
\begin{aligned}
m_p \frac{dv_i}{dt} = {} & (m_p - m_F)\, g_i + m_F \left.\frac{Du_i}{Dt}\right|_{\boldsymbol{x}(t)} + \\
& - \frac{1}{2} m_F \frac{d}{dt}\left\{ v_i(t) - u_i\left[\boldsymbol{x}(t), t\right] - \frac{1}{10} r_p^2 \left.\nabla^2 u_i\right|_{\boldsymbol{x}(t)} \right\} + \\
& - 6\pi r_p \mu \left\{ v_i(t) - u_i\left[\boldsymbol{x}(t), t\right] - \frac{1}{6} r_p^2 \left.\nabla^2 u_i\right|_{\boldsymbol{x}(t)} \right\} \\
& - 6\pi r_p^2 \mu \int_0^t d\tau \left(\frac{\rho_f}{\sqrt{\pi\mu(t-\tau)}} \frac{d\left\{ v_i(t) - u_i\left[\boldsymbol{x}(t), t\right] - \frac{1}{6} r_p^2 \left.\nabla^2 u_i\right|_{\boldsymbol{x}(t)} \right\}}{d\tau} \right)
\end{aligned}
\tag{7.2}
$$

where $r_p = d_p/2$, m_p, v_i and $\boldsymbol{x}(t)$ are the radius of the particle, mass, velocity and position, respectively. $u_i\left[\boldsymbol{x}(t), t\right]$ is the fluid velocity at the particle position $\boldsymbol{x}(t)$, while $Du_i/Dt|_{\boldsymbol{x}(t)}$ is the time derivative following the fluid element at particle position. The left-hand-side of equation (7.2) describes the inertial force of the particle, while on the right-hand-side the external forces acting on particles are apparent. The first term on right-hand-side is the mass and buoyancy force, the second is the fluid acceleration, then the added mass force appears accounting the fact that, moving through the fluid, particles have to move some volume of surrounding fluid. The fourth term is the drag force taking into account the viscous force of fluid on particle, the Stokes drag for small particle Reynolds number $Re_p = U_\infty d_p/\nu$ (where U_∞ is the fluid velocity) is used, while for high Re_p the correction factor should be introduced $c_f = 1 + 0.15\, Re_p^{0.687}$. The last term is the Basset history force that accounts for the temporal delay of particle boundary layer development with the relative velocity variations. Since the particle is not rotating here, the lift force due to the shear and Magnus effect is not considered. Added mass, Stokes drag and Basset history terms present additional term proportional to the velocity Laplacian accounting the Faxen correction taking into account the non-uniformity of the fluid velocity.

In this context, the density ratio ρ_p/ρ_f is assumed equal to 4000 that coincides with the ratio between Alumina particle used commonly in the Particle Image Velocimetry (PIV) measurements and fluid. Besides we assume small Φ, hence inter-particle collision and hydrodynamic interaction are neglected. Gravitational and buoyancy force are not considered. Under these assumptions

equation (7.2) reduces to

$$\frac{dv_i}{dt} = \frac{u_i - v_i}{\tau_p} \tag{7.3}$$

while to compute the particle position the trajectory equation reads

$$\frac{dx_i}{dt} = v_i \,. \tag{7.4}$$

7.1 Particle dynamics in reactive turbulent flows

Reacting flows laden with particles of different inertia and dimensions are common in many fields of engineering and physics. Dispersed aluminum particles are found in solid-fueled rocket engines [58]. They are embedded in the fuel matrix and, after ablation, released in the flow where they are oxidized, thus increasing the propulsion performance of the system. Undesirable particles are also found in reciprocating engines where carbon soot may form due to pyrolysis of the fuel droplet and its incomplete combustion [59, 60]. They also find application as transducers in Particle Image Velocimetry (PIV), where the fluid velocity field is measured by the displacement of small seeding particles [61, 62].

Particle behavior in a variety of flows, i.e. homogeneous and isotropic flows, shear, pipe and channel flows, is the topic of many papers which aim at understanding localized phenomena such as turbophoresis in wall bounded flows, or preferential accumulation and clustering in the small scales of turbulence, see [63, 64, 65, 66, 67, 68, 49, 69] among others. In all these flows, the interaction between the multi-scale turbulent structures and the particle has a strong influence on the particle behavior and distribution. In particular, numerical and experimental data of turbulence simulations show the tendency of particles to leave the center of vortical structures and to congregate in high strain regions where clusters take form. This tendency strongly depends on the particle relaxation time, which is the particle delay to follow fluid velocity fluctuation. In particular, the maximum clustering occurs for particles matching the characteristic Kolmogorov time scale [50, 70, 49]. In wall turbulence the congregation of particles at the wall is observed and ascribed to the specific turbulent structures in the wall bounded flow interacting with the particles [51, 67].

Inertial particle behavior in turbulent free jet is investigated in [70, 67]. It is shown [67] that the particle behavior is strongly dependent on the local fluid dynamical characteristic time which in the free turbulent jet varies along the axial direction. The particle behavior spatially evolves, depending on the flow features towards a tracers-like behavior, with inertia influencing the time to achieve this condition.

Particle clustering has a strong influence on droplets growth in clouds via coalescence [71, 72], on particle settling [73] and on inter-particle collisions [74]. The spatial distribution of droplets in jets is a topic of several works [75, 76, 77, 78, 79] since it may influence combustion processes and temperature distributions in flames [80].

In presence of spatial temperature variations, the temperature gradient may influence the particle spatial distribution, as discussed in [81]. Due to thermal diffusion the mean particle distribution is not uniform, with increased localization near the minimum of the mean temperature. The authors demonstrate that the accumulation induced by the thermal gradient is stronger than the turbulence- induced accumulation found in isothermal conditions.

In addition to the more familiar effects observed in cold flows, e.g. ejection from persistent vortical structures and concentration in large strain regions, particles present further interesting

peculiarities in turbulent premixed combustion. Some of these are more or less known, or expected, e.g. thermophoresis as unbalanced thermal drift in presence of extreme temperature gradients, or abrupt mean concentration decrease, induced by the strong thermal expansion across the flame front. Others are new, or at least much less discussed in the scientific literature, and associated with the sudden acceleration across the thin fluctuating turbulent front.

In the context of particle seeding suited for premixed combustion, several papers addressed the impact of thermophoresis and that of the non homogeneity of refractive index, e.g. [82, 83, 84, 85]. Thermophoresis amounts to a force that influences tiny particle motions within the reacting zone: the steep temperature gradient between reactants and products generates an unbalanced migration of particles driven by Brownian forces which results in a drift towards the cold gases [86, 87].

Part II

Methodology

In this section the methodology employed for data acquisition is presented. Both numerical and experimental simulations are performed in particle laden reactive flow to stress the specific phenomena originating from the inertial particle/turbulent combustion interaction. The numerical simulations are performed by means an in house code developed in previous years in the Department of Mechanics and Aeronautics [22]. The experimental simulations are performed in C.R. ENEA Casaccia where the setup has been made in the previous year [8, 9]. The experimental facility allow the Particle Image Velocimetry (PIV) and the Laser Induce Fluorescence (LIF) of a Bunsen premixed flame of turbulent methane/air mixture with variable fuel/oxidizer ratio.

Chapter 8

Numerical methodology

The algorithm of the numerical simulation is the discretized Low-Mach number expansion of the Navier Stokes equations in cylindrical coordinates. As will be explained in the results, this Navier-Stokes equation formulation allows the description of a low Mach number flow characterized by an arbitrary density variation neglecting the acoustic effects [88, 89]. In the present context the density variation is due to the boundary condition because two different density values are enforced at the inflow, one for he central jet and the other for the flow around it, and to the combustion reaction causing the heat release into the flame front. Further detail on the Low-Mach number expansion and on the simulation features will be provided in the results part.

The numerical code used for the numerical simulation has been developed in the Department of Mechanics and Aeronautics of the Sapienza university. The FORTRAN 77 language is used and it is able to perform both Direct Numerical Simulation (DNS) and Large Eddy Simulation (LES) thanks to the implementation on several sub-grid model [90]. In addition the numerical code allows to simulate both reactive, with several model for the combustion reaction, and non-reactive flow with or without Lagrangian particles seeding.

The Eulerian algorithm discretizes the Low-Mach number formulation of the Navier-Stokes equations [88] in a cylindrical domain, which describes a low Mach number flow with arbitrary flame-induced density variations neglecting acoustics effects,

$$\frac{\partial \rho}{\partial t} + \boldsymbol{\nabla} \cdot (\rho \boldsymbol{u}) = 0 \tag{8.1}$$

$$\begin{aligned}\frac{\partial \rho \boldsymbol{u}}{\partial t} + \boldsymbol{\nabla} \cdot (\rho \boldsymbol{u}\boldsymbol{u}) = \\ - \boldsymbol{\nabla}\mathcal{P} + \frac{\infty}{\mathcal{R}\rceil}\boldsymbol{\nabla} \cdot \left[\mu \left(\boldsymbol{\nabla}\boldsymbol{u} + \boldsymbol{\nabla}\boldsymbol{u}^{\mathcal{T}}\right)\right] + \frac{\infty}{\mathcal{F}\nabla^{\in}}\rho \boldsymbol{f}\end{aligned} \tag{8.2}$$

$$\frac{\partial \rho Y_R}{\partial t} + \boldsymbol{\nabla} \cdot (\rho Y_R \boldsymbol{u}) = \frac{1}{ReSc_R}\boldsymbol{\nabla} \cdot (\rho D_R \boldsymbol{\nabla} Y_R) - \omega_R \tag{8.3}$$

$$\boldsymbol{\nabla} \cdot \boldsymbol{u} = \frac{1}{\mathcal{P}}\left[\frac{1}{RePr}\boldsymbol{\nabla} \cdot (\alpha \boldsymbol{\nabla} T) + \frac{\gamma - 1}{\gamma} Ce\, \omega_R\right] \tag{8.4}$$

$$\vartheta = \frac{p}{\rho} \tag{8.5}$$

with ρ, $\mathbf{u}$ and $\mathcal{P}$ the density, the velocity and the dynamic pressure, respectively- T, p Y_R and ω_R are the temperature, the thermodynamic pressure, the reactant concentration and its global reaction rate, respectively. $Re = \rho_0 U_0 L_0/\mu_0$ is the Reynolds number and $Pr = \mu_0/(\rho_0 \alpha)$ is the Prandtl number giving the ratio between thermal diffusion and viscosity of the mixture (here $Pr = 0.6$). The ratio between the heat capacity coefficient is denoted by γ (here $\gamma = 1.33$) and the ratio between mass and momentum transport reactant coefficient is given by the Schmidt number $Sc_R = \mu_0/(\rho_0 D_R)$ (here $Sc_R = 0.6$).

Spatial discretization is based on central second order finite differences in conservative form on a staggered grid. The convective terms of the relevant reaction-advection-diffusion equations for the scalars are discretized by a bounded central difference scheme designed to avoid spurious oscillations [91]. This non-linear scheme imposes the boundness property characteristic of the convection terms without introducing a large extra-dissipation as in classical TVD schemes. Temporal evolution is performed by a low-storage third order Runge-Kutta scheme [4].

Time evolving Dirichlet data (prescribed velocity) are enforced at the inflow to simulate a turbulent inlet. A cross-sectional plane extracted from a companion DNS of a turbulent pipe flow serves the purpose. Convective and traction-free conditions are adopted at the outflow and at the side boundary (mantle in figure 8.1), respectively. The traction-free conditions are useful to allows the entrainment effects characteristic of the jet dynamics, they consist in a sort of no-shear conditions at the side boundary. The numerical domain is showed in figure 8.1 where the all boundaries are highlighted and the periodic pipe (green lines) is included. More details on the code and tests for incompressible jet and pipe flows can be found in [22, 67].

8.1 Reactive jet

Chemical kinetics is assumed in the form of a global Arrhenius irreversible reaction transforming a premixed fresh mixture R into exhaust combustion products P.

The simulation reproduces a premixed Bunsen flame with fully developed turbulent inflow and Reynolds number $Re_D = U_0 D/\nu_\infty = 6000$, with U_0 the bulk velocity and $D = 2R$ the nozzle

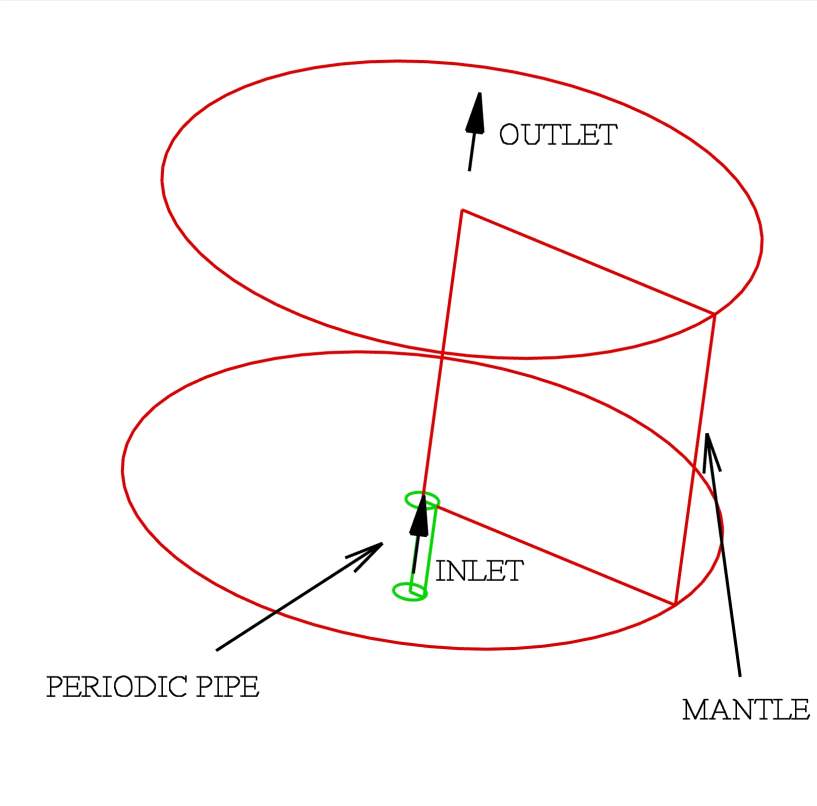

Figure 8.1 Schematic representation of the numerical domain. Red line highlights the edge of the open environment in which the free jet evolves, green line shows the edge of the cylindrical pipe.

diameter. The simulation reproduces a lean premixed methane/air Bunsen flame (equivalence ratio $\phi \sim 0.7$, temperature ratio $\vartheta_b/\vartheta_u = 5.3$). Under these conditions the ratio of laminar flame speed to bulk velocity is $S_L/U_0 \simeq 0.05$, with a laminar flame thickness $\delta_L \simeq 0.019\,D$. The specific heat capacity ratio is assumed constant, $\gamma = c_p/c_v = 1.33$, and the dynamic viscosity is proportional to the square root of temperature, $\mu \propto \vartheta^{1/2}$. Initial conditions in the open environment are tuned in order to have standard thermodynamic conditions ($p = 1\,atm$, $\vartheta = 300\,K$) and stationary fluid. The computational domain, $[\varphi_{max} \times R_{max} \times Z_{max}] = [2\pi \times 6.2D \times 7D]$, is discretized by $N_\varphi \times N_r \times N_z = 128 \times 201 \times 560$ grid points.

The grid is designed to assure optimal accuracy in the region where the instantaneous flame turns out to be confined, with a typical grid size everywhere below three times the Kolmogorov scale.

A snapshot of axial fluid velocity and flame front position is reproduced in figure 8.2, top panel, to provide an overall view of the instantaneous configuration of the flame. The bottom panel displays the reactant concentration profile across the instantaneous front at three axial distances. From the symbols, corresponding to the actual positions of the related grid nodes, an impression on the spatial accuracy of the simulation can be obtained. The solid line is the concentration profile for the corresponding laminar, unstretched 1D flame. The comparison validates the flamelet regime for the present flame: in fact in the flamelet regime the flame, although strongly corrugated, is expected to be locally still laminar.

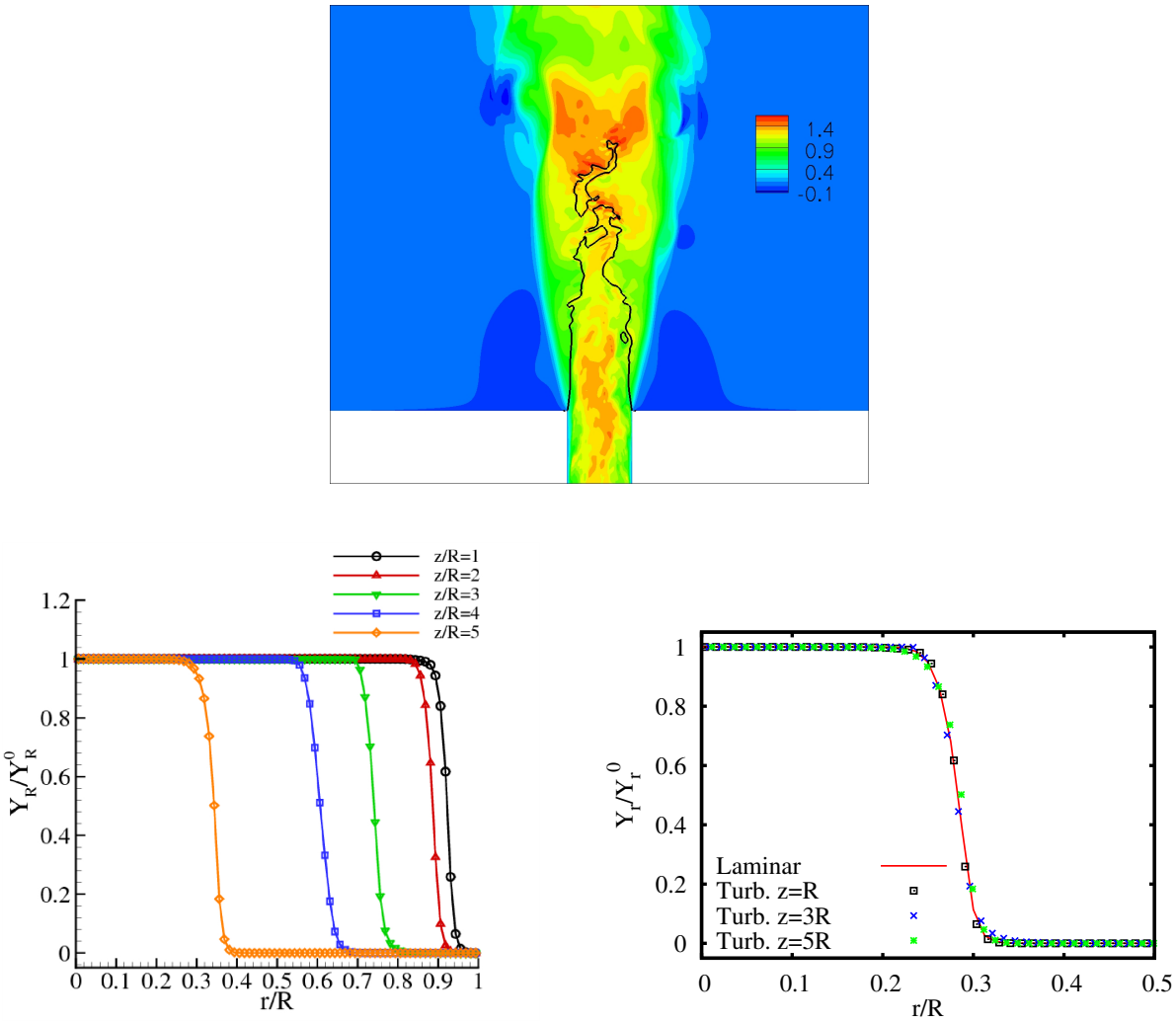

Figure 8.2 Top: instantaneous 2D cut of axial velocity (contours) and iso-level of reactants at $Y_r/Y_r^0 = 0.5$ (solid line). Bottom:left panel, instantaneous profiles of reactant concentration vs r/R at different axial distances. Right panel, radial concentration profiles across the instantaneous flame front at three axial distances, $z/R = 1, 3, 5$ (symbols). The continuous line is the corresponding laminar 1D profile.

8.2 Particle evolution

Particles are followed using Lagrangian tracking by integrating equations (7.3) and (7.4) with the same Runge-Kutta scheme used for the fluid phase. Fluid velocities are interpolated at particles positions with second order Lagrangian polynomials, see [67] for details. Particles do not act on the flow (one-way coupling) and inter-particle collisions are neglected, as appropriate for the typical seeding used in PIV. Four particle populations are considered with flamelet Stokes numbers $St_{fl} = 0.022$, $St_{fl} = 0.54$, $St_{fl} = 2.16$, $St_{fl} = 8.65$, respectively, to mimic a laboratory Bunsen premixed flame ($U_0 = 4.5\,\mathrm{ms}^{-1}$ and $D = 20\,\mathrm{mm}$) seeded with Alumina particles ($\rho_p \simeq 4000$ kg/m^3) with diameters $d_p = 1\,\mu$m, $d_p = 5\,\mu$m, $d_p = 10\,\mu$m, $d_p = 20\,\mu$m, respectively. The corresponding time constants τ_p of the particle populations ranges from $\sim 9\,\mu$s for $d_p = 1\,\mu$m to $\sim 3.5\,$ms for $d_p = 20\,\mu$m (the reference temperature is $T_m = (T_u + T_b)/2$), see e.g. [85, 92, 93, 94]. We remark that the particle relaxation time depends quadratically on the diameter and linearly on the density ratio.

Particles are introduced in the field at fixed rate, about 33 particles for $\Delta t = 2 \times 10^{-3} D/U_0$,

with homogeneous distribution at the inlet section of the jet where their assigned velocity equals that of the local fluid. Overall about six millions particles are used in the simulation.

8.3 Code Validation

The numerical code has been extensively validated both in the incompressible [22, 50] and reactive conditions [95], both with dispersed particles [95, 50] and without [22, 50].

8.3.1 Coaxial jet validation

Dealing with the real gas co-axial jet the domain extends up to $R_{max} = 8\,D$ and is discretized with 281 nodes. The mesh is uniform up to $r = .7\,D$ and is stretched quadratically up to the external boundary. In this conditions the typical number of grid points across the instantaneous shear layer between the high density jet core and the coaxial low density jet is about 5 as shown by the figure 8.3, where symbols are associated with the actual positions of the computational nodes.

Since the Kolmogorov scale is of order of $\eta = 0.01\,D$ and increases with the axial coordinate, the radial grid size of $0.00625\,D$ is appropriate for the Direct Numerical Simulations of the studied phenomenon [96, 97].

8.3.2 Reactive jet validation

A critical aspect of both the studied phenomenologies is the spatial resolution especially in the radial direction. Dealing with the DNS of the reactive Bunsen jet seeded with inertial particle the domain extends up to $R_{max} = 6.2D$ and is discretized with 201 nodes. The instantaneous flame turns out to be confined within a maximum radial extension of $r \simeq 0.5\,D$. The mesh was tuned to be uniform up to $r = 0.6\,D$ with a grid spacing of $0.00625\,D$ to successively stretch linearly up to the external boundary. In these conditions the typical number of grid points across the instantaneous front is 6 as shown by the plots in figure 8.2, where the symbols are associated with the actual positions of the computational nodes. An estimate from below of the

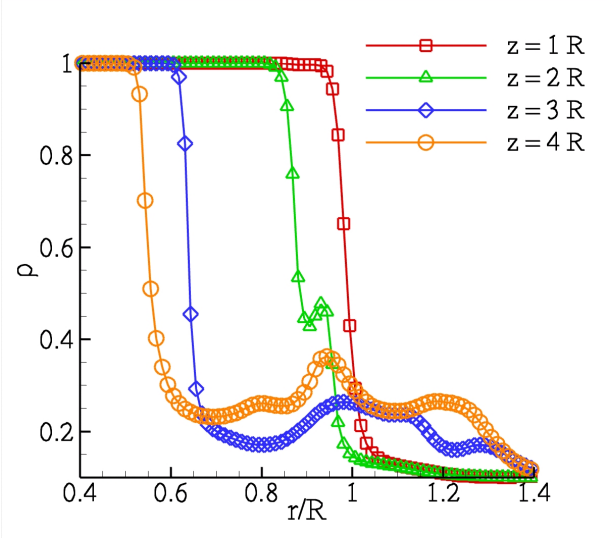

Figure 8.3 Instantaneous profiles of non dimensional density ρ vs r/R at different axial distances.

instantaneous flame thickness is based on the maximum temperature gradient in the flame, here corresponding to $\delta_L = 0.019D$. This would give order of 3 points across the flame. In fact, the actual thickness is significantly larger than such lower bound as apparent from figure 1, living space for at least 6 points across the instantaneous flame. More explicitly figure 8.2 provides a few examples of reactants concentration profiles at several axial distances (see legend) taken from an instantaneous realization of the field randomly chosen along the simulation. Actually, we carefully analysed the stored data to confirm that the situation depicted in figure 8.2 is actually generic. The figure is completed with a laminar flame profile to show that we are actually dealing with a genuine flamelet regime.

The Kolmogorov scale is typically of the order of $0.5 \times 10^{-2} D$ in the unburned region to become $0.5 \times 10^{-1} D$ in the burned gas. A radial grid size of $0.625 \times 10^{-2} R$ is certainly complying with the most stringent requirements of a proper DNS [96, 97].

Figure 8.4 concerns axial-symmetric, laminar Bunsen-flames with the same chemical model used in the reactive DNS, to provide the dependence of the laminar flame height on Prandtl number, Pr. These kind of results are strongly affected by numerical diffusion and by any inaccurate treatment of the reaction term. As such they provide a significant benchmark for the overall combustion model.

As a matter of fact starting from the fully three-dimensional code, a laminar inlet profile is enforced and the Reynolds number is reduced to keep laminar conditions in the flame. Two cases differing only in the Prandtl number ($Le = 1$), $Pr = 0.6$ and 0.15, respectively are investigated.

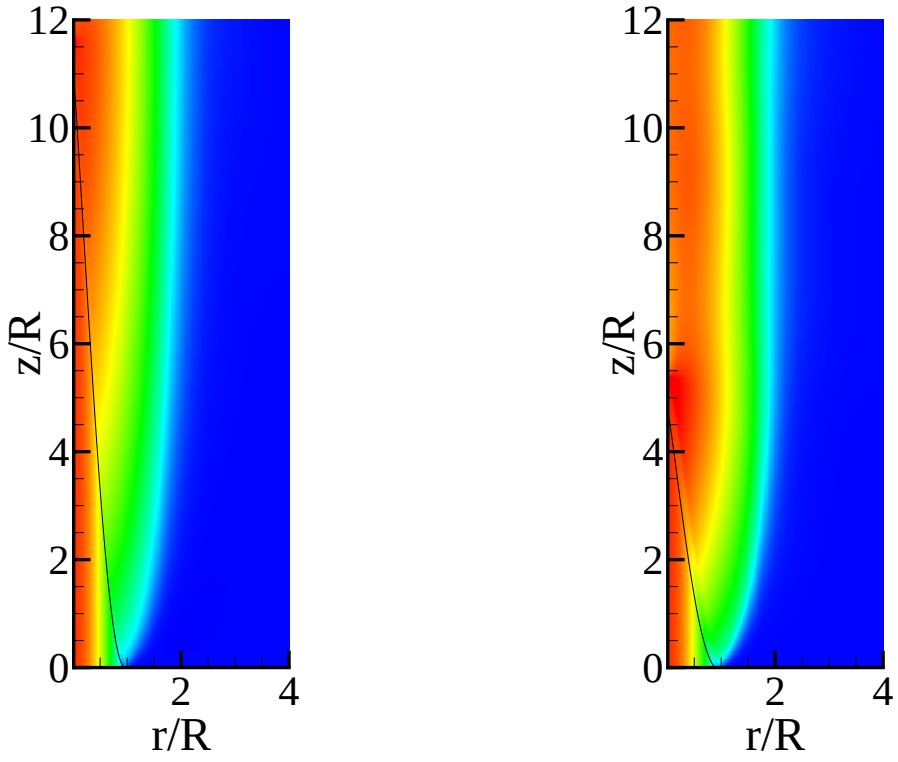

Figure 8.4 The same code used for turbulent flames is here employed to simulate Bunsen laminar flames at unit Lewis number Le, $Re_D = 3000$. Left panel, $Pr = 0.6$, $S_L/U_0 \simeq 0.1$; right panel $Pr = 0.15$, $S_L/U_0 \simeq 0.2$. Contours, isolevels of axial velocity. Solid line, isolevels of reactant concentration $Y_R = 0.99 Y_R^0$.

From the mass balance

$$\rho_u U_0 \pi R^2 = \rho_u S_L \pi R^2 \sqrt{1 + \left(\frac{H}{R}\right)^2},$$

where ρ_u is the unburned gas density, U_0 the bulk velocity at the inlet, R the nozzle radius, S_L the laminar flame speed and H the flame height, we find, for $(H/R)^2 \gg 1$ and negligible curvature effects,

$$\frac{H}{R} \simeq \frac{U_0}{S_L} .$$

Given the Prandtl number dependency of the laminar flame speed ($Le = 1$),

$$S_L \propto \frac{1}{\sqrt{Pr}},$$

for the lower Prandtl number case the flame height is expected about half the other. This behavior is confirmed in figure 8.4, reporting results from the two simulations, where the flame height may be estimated as the intercept along the axis of the isolevel $Y_R = 0.99 Y_R^0$, with Y_R^0 the inflow reactant concentration.

In addition, the ratio S_L/U_0 (0.1 and 0.2, for the two Prandtl numbers) is evaluated by independent 1D simulations of laminar flames in the same conditions. Taking the height from figure 8.4 and the flame speed from the corresponding 1D simulation, in both cases, we find $(H/R)(S_L/U_0) \simeq 1$, confirming once more the behavior expected from the mass balance equation and the scaling of S_L with the Prandtl number.

Chapter 9

Experimental apparatus

The experimental setup, used to perform the experiments, is located in C.R. ENEA Casaccia. It is made of a Bunsen burner, see figure 9.1, discharging in a open chamber the walls of which are far enough to not influence the jet dynamics. The chamber allows the optical access to provide experimental data acquisition while the Bunsen pipe ensures the homogeneous particle introduction in the jet flow. A proper system of pipes and valves allows the variation of the methane/air ratio and the entire mass injected through the jet; in this way, the Reynolds number and the equivalence ratio of the mixture can be tuned to match the desired conditions. The exhaust gases are ejected through a very long pipe to avoid the influence of the external environment on the experimental acquisition.

The facility allows to perform Particle Image Velocimetry (PIV) and Laser Induced Fluorescence (LIF) measurements in the same time; figure 9.2 shows a schematic representation of the apparatus.

Velocity measurements are performed with a commercial PIV system based on a 532 nm 54 mJ Nd:YAG LASER and a camera equipped with a lens whose focal length is 60 mm. The f-stop ranges between 4 and 5.6 to accommodate the scattering signal of different sized particles

Figure 9.1 Bunsen pipe used to obtain the reactive jet.

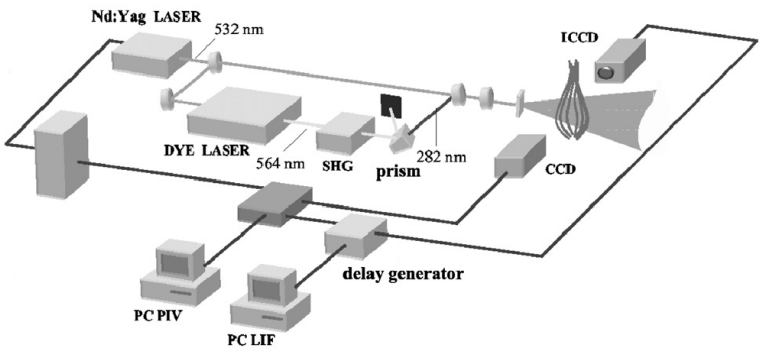

Figure 9.2 Schematic representation of the PIV/LIF apparatus used for the experimental data acquisition.

avoiding saturation of the detector. The resolution of the CCD is 1280×1024 pixels with a field-of-view of $110.7\,\text{mm} \times 88.52\,\text{mm}$. The set-up guarantees a pulse-to-pulse delay of $70\,\mu$s with a maximum particle displacement less than one-quarter of the interrogation window (32×32 pixels with an overlap of 50% and spatial resolution of 2.7mm). Alumina particles are used to seed the flow. The particles have a diameter of order of $5\,\mu\,m$ and density equal to $4000 kg/m^3$. A proper circuit is used to dry the particles, due to the humidity, and to inject them in the flow.

Defining the progress variable $c = 1 - Y_R/Y_R^0$, where Y_R and Y_R^0 are the local and the inlet reactant concentrations, respectively, the mean progress variable ranges from 0 to 1 in the flame brush region moving from the fresh mixture towards the exhaust gases. The instantaneous progress variable is assumed to jump from 0 to 1 across the thin instantaneous flame front the position of which is detected by the LASER induced fluorescence of the OH radical, OH-LIF [9].

In more details, the flame front position is deduced by recording the fluorescent emission of the OH radical stimulated by a 282 nm LASER source obtained by pumping a tunable dye-laser with the Nd:YAG source. The OH emission is acquired by a 1024×1024 pixel ICCD equipped with a 78 mm Nikon quartz lens providing a resolution of 160 μm/pixel, with a 2×2 pixel binning. A narrow pass-band filter, 10 nm wide and centered at 310 nm, avoids spurious signals originated by other ultraviolet sources, more details in [9]. A maximum gradient criterion has been adopted to extract the flame front position from the fluorescence signal. The estimated position of the instantaneous flame front is used to define the instantaneous field of progress variable c, taken to be one in the burned gases and zero in the fresh mixture (flamelet assumption). From the instantaneous configurations the mean field $C = \langle c \rangle$ is evaluated by standard ensemble averaging.

Part III

Results

This last part is dedicated to the main results obtained in the field of the turbulent jet. The first part deals with the supercritical fluid jet discharging in a high pressure environment. First, the generalization of the Low Mach number expansion, provided by Majda & Sethian [88] for perfect gas, is presented in the case of the real gas equation of state. Then the effects of the near critical thermodynamics conditions on the structures of the variable density jet is addressed. The second chapter is devoted to the study of the dynamics of the coaxial turbulent jet discharging in an ambient at a pressure weakly supercritical, where the geometry and conditions employed mimic the cryogenic injectors of liquid rocket engines for spatial propulsion.
In the second part the dynamics of inertial particles in a turbulent premixed flame is addressed. It is shown that due to their inertia particles follow fluid fluctuation with a certain delay time. To describe the particle dynamics a proper Stokes number is defined. This Stokes number is the ratio between the particle relaxation time and the fastest time scale of fluid. In turbulent premixed flames the smaller time scale is imposed by the chemical kinetics, so the "flamelet" Stokes number is defined. In the first chapter, the particle partial distribution is emphasized. It is shown as the interaction between the particle inertia and the fluctuating wrinkled flame front influences cluster formation especially in the flame brush and burned gas region. In the second chapter, the effects of particle inertia on PIV measurements is stressed. The seeding particles are employed as transducers in the velocity field measurements, i.e. the particle velocity is assumed equal to the fluid one. It is proved that the validity of the latter assumption depends strongly on the "flamelet" Stokes number which is proved to be the only parameter to describe the particle dynamics in turbulent premixed flame.

Chapter 10

Low-Mach number formulation for real gas: supercritical turbulent round jet

Modern energy production engines are all characterized by two important features: the high pressure occurring in the combustion chamber necessary to increase the provided power, and the controlled velocity of injection in order to avoid the occurrence of the flame blow-off in the high velocity condition or the flame flash-back when the velocity injection is small compared with the flame speed. In particular according to the high temperature in the combustion chamber the Mach number results to be of order of $10^{-2} - 10^{-1}$ [30, 35]. Cryogenic rocket engines, advanced gas turbines and diesel engines are all examples of devices characterized by these injection conditions. Typically the reactants are injected in an environment with pressure close or above their critical pressure. In these conditions the behavior of the fluid differs strongly from that of a perfect gas, see for details § II. It exhibits large variations of thermodynamic and transport properties also for small temperature changes, with significant effects on mixing and combustion processes. In this context an appropriate numerical simulation should take into account such thermodynamic phenomena via suitable equations of state and transport relations.

While the fully compressible numerical methods are most suitable for transonic and supersonic simulations, from the numerical point of view approaching the Mach number to zero they loss efficiency and accuracy [98], because of the fluid dynamics time scales are extremely different from the acoustic ones. In this framework the *Majda & Sethian* developed *Low Mach expansion* [88].

The aim of this chapter is to present the generalization of the Low-Mach expansion to the real gas conditions and to apply the new equation system to the simple configuration of variable-density turbulent jet at a pressure slightly above the critical point. The first part, § 10.1, is dedicated to the derivation of the equations employed to reproduce the real gas jet dynamics at low-Mach number. In section § 10.2 the variable-density turbulent jet simulations are presented. Three different conditions are compared: the first turbulent jet discharges in an ambient at weakly supercritical pressure, and the other two consist of perfect gas jets matching the jet/environment density and temperature ratio of the real gas jet. At the end of the chapter the main conclusions are presented.

10.1 Real gas Low Mach number expansion

In order to neglect acoustic phenomena from numerical simulation with density variation induced by combustion or phase changes the *low Mach number expansion* of the Navier-Stokes equations was introduced by *Majda & Sethian* [88].

The complete system used by *Majda & Sethian* in their original derivation assumes that the evolving gas could be considered perfect and thus they employed the well known perfect gas equation of state. Here the Navier-Stokes equation system is coupled with the Van der Waals equation to mimic the fluid behavior near the critical thermodynamic conditions,

$$\frac{\partial \rho^*}{\partial t^*} + \boldsymbol{\nabla}^* \cdot (\rho^* \boldsymbol{u}^*) = 0\,, \tag{10.1}$$

$$\frac{\partial (\rho^* \boldsymbol{u}^*)}{\partial t^*} + \boldsymbol{\nabla}^* \cdot (\rho^* \boldsymbol{u}^* \boldsymbol{u}^*) = \boldsymbol{\nabla}^* \cdot \boldsymbol{\tau}^* - \boldsymbol{\nabla}^* p^* + \boldsymbol{f}^*\,, \tag{10.2}$$

$$\begin{aligned}\frac{\partial (\rho E^*)}{\partial t^*} + \boldsymbol{\nabla}^* \cdot (\rho^* \boldsymbol{u}^* H^*) = {} & \boldsymbol{\nabla}^* \cdot (\boldsymbol{\tau}^* \cdot \boldsymbol{u}^*) + \boldsymbol{\nabla}^* \cdot (k^* \boldsymbol{\nabla}^* \vartheta^*) \\ & - \sum_\alpha \Delta H^*_\alpha \, \omega^*_\alpha + \boldsymbol{f}^* \cdot \boldsymbol{u}^*\,,\end{aligned} \tag{10.3}$$

$$\frac{\partial (\rho^* Y^*_\alpha)}{\partial t^*} + \boldsymbol{\nabla} \cdot (\rho^* \boldsymbol{u}^* Y^*_\alpha) = \boldsymbol{\nabla} \cdot (\rho^* D^*_\alpha \boldsymbol{\nabla} Y^*_\alpha) + \omega^*_\alpha \tag{10.4}$$

$$\frac{p^*}{\rho^*} = \frac{\bar{R}^* \, \vartheta^*}{1 - b'^* \rho^*} - a'^* \rho^*. \tag{10.5}$$

All dimensional variables are denoted by superscript $*$, hence t^*, ρ^*, p^*, ϑ^*, $\boldsymbol{u}^*$ denote time, density, pressure, temperature and velocity vector, respectively. The vector differential operators $\boldsymbol{\nabla}^* \cdot$ and $\boldsymbol{\nabla}^*$ are the divergence and the gradient. The viscous forces for the Newtonian fluid are given by the divergence of the shear stress tensor $\boldsymbol{\tau}^* = \mu^* [(\boldsymbol{\nabla}^* \boldsymbol{u}^* + (\boldsymbol{\nabla}^* \boldsymbol{u}^*)^T) - \frac{2}{3} (\boldsymbol{\nabla}^* \cdot \boldsymbol{u}^*) \, \boldsymbol{I}]$, where μ^* is the dynamic viscosity depending on temperature, while $\boldsymbol{f}^* = -\rho^* g^* \boldsymbol{e}_z$ take into account the gravitational force (with $\boldsymbol{e}_z$ the vertical unit vector). In the energy equation the total internal energy E^* and enthalpy H^* are apparent in left-hand-side, while in right-hand-side the different terms represent the viscous stress work, the heat flux due to flow inhomogeneity modeled with the Fourier law (k^* is the thermal diffusion) [1], the heat release due to chemical reaction where ω^*_α and ΔH^*_α are the consumption/production rate and the formation enthalpy of the α-th species, respectively. Equation (10.4) is the continuity equation for the generic species α where D^*_α is the species diffusion [2] the consumption/production terms due to the combustion is introduced, last term on right-hand-side. Here the terms taking into account combustion phenomena are included even if in the simulation presented chemical reactions are neglected.

Although in the literature several state equations [16, 19] suitable for different ranges of pressure and temperature are present, the Van Der Waals state equation is here considered

[1] the Dufour effect is not considered because only one chemical species is employed in our simulations

[2] the Soret effect is not included because we will consider only one chemical species in particular the nitrogen, with strong density and temperature variations

the proper model to mimic the supercritical thermodynamic state due to the unquestionable simplicity in conjunction with the rigorous derivation from statistic dynamics theories. The statistical mechanics (see [99] for the complete derivation) provides the specific internal energy $e^* = U^*/\rho^*$:

$$e^* = \frac{1}{\gamma - 1}\bar{R}^*\vartheta^* - a^*\rho^* \,, \tag{10.6}$$

where $\gamma = c_p^*/c_v^*$ is the ratio of the specific heat coefficient at constant pressure and volume. Considering equations (10.5), (10.6) and the total internal energy relation $E^* = e^* + |\boldsymbol{u}^*|^2/2$ the state equation reads

$$p^* = \frac{\gamma - 1}{1 - b^*\rho^*}\rho^* E^* - \frac{\gamma - 1}{1 - b^*\rho^*}\frac{|\rho^*\boldsymbol{u}^*|^2}{\rho^*} + \frac{\gamma - 1}{1 - b^*\rho}a^*\rho^{*2} - a^*\rho^{*2} \,. \tag{10.7}$$

To perform the *Low Mach number* approximation the non-dimensionality of the whole system (10.1)-(10.5) is recommended. The reference quantities, indicated with the subscript '∞', consist in a characteristic length ℓ_∞^*, velocity u_∞^*, pressure p_∞^* and density ρ_∞^*. They allow to determine all the other reference quantities,

$$t_\infty^* = \frac{l_\infty^*}{u_\infty^*}, \quad E_\infty^* = e_\infty^* = H_\infty^* = \frac{p_\infty^*}{\rho_\infty^*}, \quad \vartheta_\infty^* = \frac{p_\infty^*}{\bar{R}_\infty^*\rho_\infty^*} \,.$$

The normalization of the entire system (10.1) coupled with the state equation (10.7), provide hence the non-dimensional equations,

$$\frac{\partial\rho}{\partial t} + \boldsymbol{\nabla}\cdot(\rho\boldsymbol{u}) = 0 \tag{10.8}$$

$$\frac{\partial(\rho\boldsymbol{u})}{\partial t} + \boldsymbol{\nabla}\cdot(\rho\boldsymbol{u}\boldsymbol{u}) = \frac{1}{Re}\boldsymbol{\nabla}\cdot\boldsymbol{\tau} - \frac{1}{\tilde{M}a^2}\boldsymbol{\nabla}p - \frac{1}{Fr^2}\rho\boldsymbol{e}_z \tag{10.9}$$

$$\begin{aligned}\frac{\partial(\rho E)}{\partial t} + \boldsymbol{\nabla}\cdot(\rho\boldsymbol{u}H) = \frac{\tilde{M}a^2}{Re}\boldsymbol{\nabla}\cdot(\boldsymbol{\tau}\cdot\boldsymbol{u}) + \frac{\gamma}{(\gamma-1)RePr}\boldsymbol{\nabla}\cdot(k\boldsymbol{\nabla}\vartheta) + \\ + \sum_a Ce_\alpha\, Da_\alpha\,\omega_\alpha + \tilde{M}a^2\boldsymbol{f}\cdot\boldsymbol{u}\end{aligned} \tag{10.10}$$

$$\frac{\partial(\rho Y_\alpha)}{\partial t} + \boldsymbol{\nabla}\cdot(\rho\boldsymbol{u}Y_\alpha) = \frac{1}{ReSc_\alpha}\boldsymbol{\nabla}\cdot(\rho D_\alpha\boldsymbol{\nabla}Y_\alpha) + Da_\alpha\,\omega_\alpha \tag{10.11}$$

$$p = \frac{\rho\vartheta}{1 - b'\rho} - a'\rho^2 \tag{10.12}$$

where the classical non-dimensional numbers manifest

$$\tilde{M}a = \frac{u_\infty^*}{\sqrt{\frac{p_\infty^*}{\rho_\infty^*}}} = \sqrt{\gamma}\,Ma, \quad Re = \frac{u_\infty^*\,\ell_\infty^*\,\rho_\infty^*}{\mu_\infty^*}, \quad Pr = \frac{c_{p_\infty}^*\mu_\infty^*}{k_\infty^*},$$

$$Fr = \frac{u_\infty^*}{\sqrt{\ell_\infty^* g^*}}, \quad Ce_\alpha = -\frac{\rho_\infty^*\Delta H_\alpha^*}{p_\infty^*}, \quad Da_\alpha = \frac{\omega_{\alpha\infty}^*}{\rho_\infty^* t_\infty^*}, \quad Sc_\alpha = \frac{\mu_\infty}{D_{\alpha\infty}\rho_\infty^*}.$$

We highlight that the thermal diffusion k_∞^* and the dynamic viscosity μ_∞^* are evaluated at the reference temperature ϑ_∞^*.

To obtain the *Low Mach number* formulation, Mach number $\tilde{Ma}$ is the proper parameter for the asymptotic power expansion. In order to separate the acoustics and fluid dynamics time scales, all variables are represented as the sum of the first three terms of the Taylor expansion in terms of the Mach number,

$$\boldsymbol{f}(\boldsymbol{x},t) = \boldsymbol{f}_0(\boldsymbol{x},t) + \boldsymbol{f}_1(\boldsymbol{x},t)\,\tilde{Ma} + \boldsymbol{f}_2(\boldsymbol{x},t)\tilde{Ma}^2 + O(\tilde{Ma}^3)\,.$$

The power expansion is then substitute in the equations (10.8), (10.9), (10.10) and (10.12). Applying the expansion to the product between two variable $(f\,g)$, occurring in the convective terms of the conservative form of Navier Stokes equations, we obtain

$$\begin{aligned}(f\,g) &= (f\,g)_0 + (f\,g)_1\,\tilde{Ma} + (f\,g)_2\tilde{Ma}^2 + O(\tilde{Ma}^3) = \\ &= [f_0 + f_1\,\tilde{Ma} + f_2\tilde{Ma}^2 + O(\tilde{Ma}^3)]\cdot[g_0 + g_1\,\tilde{Ma} + g_2\tilde{Ma}^2 + O(\tilde{Ma}^3)] = \\ &= f_0\,g_0 + (f_1\,g_0 + f_0\,g_1)\tilde{Ma} + (f_2\,g_0 + f_0\,g_2 + f_1\,g_1)\tilde{Ma}^2 + O(\tilde{Ma}^3)\,,\end{aligned}$$

equating the terms of the same order in $\tilde{Ma}$, the following relations are obtained,

$$(f\,g)_0 = f_0\,g_0 \tag{10.13}$$

$$(f\,g)_1 = f_1\,g_0 + f_0\,g_1 \tag{10.14}$$

$$(f\,g)_2 = f_2\,g_0 + f_0\,g_2 + f_1\,g_1\,. \tag{10.15}$$

Now we can apply the expansion to the continuity equation (10.8)

$$\begin{aligned}&\frac{\partial(\rho_0 + \rho_1\tilde{Ma} + \rho_2\tilde{Ma}^2 + O(\tilde{Ma}^3))}{\partial t} + \\ &+\boldsymbol{\nabla}\cdot((\rho\boldsymbol{u})_0 + (\rho\boldsymbol{u})_1\tilde{Ma} + (\rho\boldsymbol{u})_2\tilde{Ma}^2 + O(\tilde{Ma}^3)) = 0\end{aligned} \tag{10.16}$$

Assembling the same order terms the continuity equation yields,

$$\begin{aligned}&(\frac{\partial\rho_0}{\partial t} + \boldsymbol{\nabla}\cdot(\rho\boldsymbol{u})_0) + (\frac{\partial\rho_1}{\partial t} + \boldsymbol{\nabla}\cdot(\rho\boldsymbol{u})_1)\tilde{Ma} + \\ &(\frac{\partial\rho_2}{\partial t} + \boldsymbol{\nabla}\cdot(\rho\boldsymbol{u})_2)\tilde{Ma}^2 + O(\tilde{Ma}^3) = 0\end{aligned}$$

In order to verify the mass conservation, each order of the power expansion should be null obtaining the l-th order continuity equation,

$$\frac{\partial\rho_l}{\partial t} + \boldsymbol{\nabla}\cdot(\rho\boldsymbol{u})_l = 0\,, \qquad l = 0,1,2 \tag{10.17}$$

The same procedure is applied to the momentum equation (10.9) obtaining,

$$\begin{aligned}&\frac{\partial((\rho\boldsymbol{u})_0 + (\rho\boldsymbol{u})_1\tilde{Ma} + (\rho\boldsymbol{u})_2\tilde{Ma}^2 + O(\tilde{Ma}^3))}{\partial t} + \\ &+\boldsymbol{\nabla}\cdot((\rho\boldsymbol{u}\boldsymbol{u})_0 + (\rho\boldsymbol{u}\boldsymbol{u})_1\tilde{Ma} + (\rho\boldsymbol{u}\boldsymbol{u})_2\tilde{Ma}^2 + O(\tilde{Ma}^3)) = \\ &= -\tfrac{1}{\tilde{Ma}^2}\boldsymbol{\nabla}(p_0 + p_1\tilde{Ma} + p_2\tilde{Ma}^2 + O(\tilde{Ma}^3)) + \\ &+\tfrac{1}{Re}\boldsymbol{\nabla}\cdot(\boldsymbol{\tau}_0 + \boldsymbol{\tau}_1\tilde{Ma} + \boldsymbol{\tau}_2\tilde{Ma}^2 + O(\tilde{Ma}^3)) + \\ &+\boldsymbol{f}_0 + \boldsymbol{f}_1\,\tilde{Ma} + \boldsymbol{f}_2\tilde{Ma}^2 + O(\tilde{Ma}^3)\end{aligned} \tag{10.18}$$

Performing the product between equation (10.18) and $\tilde{Ma}^2$ the following relations can be obtained,

$$\begin{cases}\text{Order 0:} & \boldsymbol{\nabla}p_0 = 0 \;\Rightarrow\; p_0 = p_0(t) \\ \text{Order 1:} & \boldsymbol{\nabla}p_1 = 0 \;\Rightarrow\; p_1 = p_1(t)\end{cases} \tag{10.19}$$

which highlights the fact that the zeroth- and first-order pressure terms are constant in space, depending only on time. On the other hand the second-order equation reads

$$\frac{\partial(\rho \boldsymbol{u})_0}{\partial t} + \boldsymbol{\nabla} \cdot (\rho \boldsymbol{u}\boldsymbol{u})_0 = \frac{1}{Re}\boldsymbol{\nabla} \cdot \boldsymbol{\tau}_0 - \boldsymbol{\nabla} p_2 + \boldsymbol{f}_0 \tag{10.20}$$

where the viscous term tensor reads $\boldsymbol{\tau}_0 = \mu_0[(\boldsymbol{\nabla}\boldsymbol{u}_0 + (\boldsymbol{\nabla}\boldsymbol{u}_0)^T) - \frac{2}{3}(\boldsymbol{\nabla}\cdot\boldsymbol{u}_0)\,\boldsymbol{I}]$. It is evident that the second-order equation couples the zeroth-order momentum $(\rho\boldsymbol{u})_0$ with the second-order pressure p_2 with important implications on the numerical solution of the new system.

The same procedure is now applied to the equation of state (10.12) and to the energy equation (10.10). For the Van der Waals equation of state the terms of the series expansion read

$$\vartheta_l = \frac{p_l}{\rho_l}\left(1 - b'\rho_l\right) + a'\rho_l\left(1 - b'\rho_l\right) \qquad l = 0, 1, 2\ . \tag{10.21}$$

Dealing with the global internal energy the Low Mach expansion of the non dimensional form of equation (10.7) yields

$$p_0 = \frac{\gamma - 1}{1 - b\rho_0}\rho_0 E_0 + \frac{\gamma - 1}{1 - b\rho_0} a\rho_0^2 - a\rho_0^2\,. \tag{10.22}$$

Since the relation (10.22) reduces to $p_l = (\gamma - 1)(\rho E)_l$ with $l = 0, 1$, in the perfect gas case the zeroth and first order expansion of (ρE) depends as the corresponding pressure term only on time [89]. In the real gas case, instead, the internal energy depends not only on pressure but also on density that is not constant in space. The series expansion of the energy balance equation (10.10) reads

$$\begin{aligned}
\frac{\partial(\rho E)_l}{\partial t} + \boldsymbol{\nabla}\cdot(\rho\boldsymbol{u}H)_l &= \frac{\gamma}{(\gamma-1)RePr}\boldsymbol{\nabla}\cdot(k\boldsymbol{\nabla}\vartheta)_l + \\
&\quad + \left(\sum_\alpha Ce_\alpha\, Da_\alpha\, \omega_\alpha\right)_l \qquad l = 0, 1\,, \qquad (10.23)\\
\frac{\partial(\rho E)_2}{\partial t} + \boldsymbol{\nabla}\cdot(\rho\boldsymbol{u}H)_2 &= \frac{1}{Re}\boldsymbol{\nabla}\cdot(\boldsymbol{\tau}_0\cdot\boldsymbol{u}_0) + \frac{\gamma}{(\gamma-1)RePr}\boldsymbol{\nabla}\cdot(k\boldsymbol{\nabla}\vartheta)_2 + \\
&\quad + \left(\sum_\alpha Ce_\alpha\, Da_\alpha\, \omega_\alpha\right)_2 + \frac{1}{Fr^2}\boldsymbol{f}_0\cdot\boldsymbol{u}_0\,, \qquad (10.24)
\end{aligned}$$

where it is clear the fact that in the zeroth and first order energy equation the viscous stress and external force work do not appear being proportional to the Mach number. At the end, the expansion of the species ρY_α conservation equation 10.11 reads

$$\frac{\partial(\rho Y_{\alpha 0})}{\partial t} + \boldsymbol{\nabla}\cdot(\rho\boldsymbol{u}Y_\alpha)_0 = \frac{1}{ReSc_\alpha}\boldsymbol{\nabla}\cdot(\rho_0 D_\alpha \boldsymbol{\nabla}Y_\alpha)_0 + Da_\alpha\,\omega_{\alpha 0} \tag{10.25}$$

Comparing the zeroth and first-order expansions of equations (10.17), (10.19) and (10.23) the same equation structures is apparent. This observation allows to incorporate in a single term $\tilde{\boldsymbol{f}}_0 = \boldsymbol{f}_0 + \tilde{M}a\boldsymbol{f}_1$ the first two term of the series expansion, $\boldsymbol{f}(\boldsymbol{x}, t) = \tilde{\boldsymbol{f}}_0(\boldsymbol{x}, t) + \boldsymbol{f}_2(\boldsymbol{x}, t)\tilde{M}a^2 + O(\tilde{M}a^3)$.

Since the addressed phenomenon is characterized by a very low Mach number, the high-order equations can be neglected taking care only the zeroth-order equations. To this purpose we consider the system made by equations (10.17), (10.23), (10.21), (10.20) and (10.25) assuming

$\ell = 0$. The new system is made by $N+6$ equations (1 continuity, 3 momentum, 1 energy, 1 state equation, N species equation) and $N+7$ unknown variable, $(\rho \boldsymbol{u})_0$, ρ_0, $(\rho E)_0$, $(\rho Y_\alpha)_0$, ϑ_0 and p_2. An additional equation is necessary and the equation (10.22) is used to provide the relation between the density, temperature and internal energy. We observe that all our simulations deal with open environment so that the thermodynamic pressure p_0 is constant not only in space as demonstrated by equation (10.19) but also in time.

The important feature of the new system is the combination of different order variable, in particular the second order pressure term appears in the zeroth order momentum equation. On the other hand, the second-order pressure does not appear in the other equations, hence the equation system seems to be not closed. Actually the second order pressure looks like the dynamic pressure of the incompressible Navier-Stokes equations. Then a suitable algorithm including a relation for the velocity divergence as occurs in the incompressible equations is necessary. In fact, as in the incompressible Navier-Stokes equations the pressure is used to ensure the continuity equation, $\nabla \cdot \boldsymbol{u}$, here the second order pressure is used to ensure a prescribed value of the velocity divergence. Combining equation (10.22) and the enthalpy relation

$$(\rho H)_0 = (\rho E)_0 + p_0 = \tag{10.26}$$

$$= \frac{(\gamma - b'\rho_0)}{\gamma - 1} p_0 - a'\rho_0^2 + \frac{(1 - b'\rho_0)}{\gamma - 1} a'\rho_0^2 \quad , \tag{10.27}$$

with the zeroth-order energy equation (10.23) the temporal partial derivative and the convective term read

$$\frac{\partial (\rho E)_0}{\partial t} = -\frac{p_0 b'}{\gamma - 1}\frac{\partial \rho_0}{\partial t} + \frac{1 - b'\rho_0}{\gamma - 1}\frac{\partial p_0}{\partial t} - 2a'\rho_0 \frac{\partial \rho_0}{\partial t} + \frac{2\rho_0 - 3b'\rho_0^2}{\gamma - 1}\frac{\partial \rho_0}{\partial t}\,, \tag{10.28}$$

$$\boldsymbol{\nabla} \cdot (\rho H)_0 \boldsymbol{u}_0 = (\rho H)_0 \boldsymbol{\nabla} \cdot \boldsymbol{u}_0 + \boldsymbol{u}_0 \cdot \boldsymbol{\nabla} (\rho H)_0 = (\rho H)_0 \boldsymbol{\nabla} \cdot \boldsymbol{u}_0 \tag{10.29}$$

$$= (\rho H)_0 \boldsymbol{\nabla} \cdot \boldsymbol{u}_0 + \boldsymbol{u}_0 \cdot \boldsymbol{\nabla} \rho_0 \left[-\frac{p_0 b'}{\gamma - 1} - 2a'\rho_0 + \frac{2\rho_0 - 3b'\rho_0^2}{\gamma - 1} a' \right] .$$

where $\boldsymbol{\nabla} \cdot (\rho H)_0 = \boldsymbol{\nabla} \cdot (\rho E)_0$ is used, depending p_0 only on time. Finally, the energy equation reads

$$\begin{aligned} &\frac{1 - b'\rho_0}{\gamma - 1}\frac{\partial p_0}{\partial t} + \frac{2\rho_0 - 3b'\rho_0^2}{\gamma - 1}\frac{\partial \rho_0}{\partial t} - 2a'\rho_0 \frac{\partial \rho_0}{\partial t} - \frac{p_0 b'}{\gamma - 1}\frac{\partial \rho_0}{\partial t} - \\ &\frac{p_0 b'}{\gamma - 1}\boldsymbol{u}_0 \cdot \boldsymbol{\nabla}\rho_0 - 2a'\rho_0 \boldsymbol{u}_0 \cdot \boldsymbol{\nabla}\rho_0 + \frac{2\rho_0 - 3b'\rho_0^2}{\gamma - 1} a' \boldsymbol{u}_0 \cdot \boldsymbol{\nabla}\rho_0 + \\ &\frac{(\gamma - b'\rho_0)}{\gamma - 1} p_0 \boldsymbol{\nabla} \cdot \boldsymbol{u}_0 - a'\rho_0^2 \boldsymbol{\nabla} \cdot \boldsymbol{u}_0 + \frac{(1 - b'\rho_0)}{\gamma - 1} a'\rho_0^2 \boldsymbol{\nabla} \cdot \boldsymbol{u}_0 = Q_0 \end{aligned} \tag{10.30}$$

where the zeroth-order right hand side terms Q_0 are equal to those in the perfect gas formulation [88, 89]. Reordering the different terms, equation (10.30) yields,

$$\begin{aligned} &\frac{1 - b'\rho_0}{\gamma - 1}\frac{\partial p_0}{\partial t} + \frac{\gamma}{\gamma - 1} p_0 \boldsymbol{\nabla} \cdot \boldsymbol{u}_0 - \frac{p_0 b'}{\gamma - 1}\left[\frac{\partial \rho_0}{\partial t} + \boldsymbol{u}_0 \cdot \boldsymbol{\nabla}\rho_0 + \rho_0 \boldsymbol{\nabla} \cdot \boldsymbol{u}_0 \right] - \\ &2a'\rho_0 \left[\frac{\partial \rho_0}{\partial t} + \boldsymbol{u}_0 \cdot \boldsymbol{\nabla}\rho_0 + \frac{\rho_0}{2} \boldsymbol{\nabla} \cdot \boldsymbol{u}_0 \right] + \frac{2a'\rho_0}{\gamma - 1}\left[\frac{\partial \rho_0}{\partial t} + \boldsymbol{u}_0 \cdot \boldsymbol{\nabla}\rho_0 + \frac{\rho_0}{2} \boldsymbol{\nabla} \cdot \boldsymbol{u}_0 \right] - \\ &\frac{3a'b'\rho_0^2}{\gamma - 1}\left[\frac{\partial \rho_0}{\partial t} + \boldsymbol{u}_0 \cdot \boldsymbol{\nabla}\rho_0 + \frac{\rho_0}{3} \boldsymbol{\nabla} \cdot \boldsymbol{u}_0 \right] = Q_0 \,. \end{aligned} \tag{10.31}$$

Here the zeroth-order continuity equation is used to replace the terms in the square brackets,

$$\frac{1-b'\rho_0}{\gamma-1}\frac{d\,p_0}{d\,t}+\frac{\gamma}{\gamma-1}p_0\boldsymbol{\nabla}\cdot\boldsymbol{u}_0+a'\rho_0^2\boldsymbol{\nabla}\cdot\boldsymbol{u}_0- \\ \frac{a'}{\gamma-1}\rho_0^2\boldsymbol{\nabla}\cdot\boldsymbol{u}_0+\frac{2b'a'}{\gamma-1}\rho_0^3\boldsymbol{\nabla}\cdot\boldsymbol{u}_0=Q_0\,. \tag{10.32}$$

This relation can be rewritten assembling the velocity divergence so we obtain an energy equation similar to the treatment adopted in [89],

$$\left[\gamma p_0+(\gamma-2)\,a'\rho_0^2+2a'b'\rho_0^3\right]\boldsymbol{\nabla}\cdot\boldsymbol{u}_0=Q_0\,(\gamma-1)-\left(1-b'\rho_0\right)\frac{d\,p_0}{d\,t}\,. \tag{10.33}$$

The energy equation in the previous form implies for the velocity divergence:

$$\boldsymbol{\nabla}\cdot\boldsymbol{u}=\frac{Q_0\,(\gamma-1)}{p_0\gamma}\left[\frac{1}{1+\frac{(\gamma-2)a'\rho_0}{p_0\gamma}+\frac{2a'b'\rho_0^3}{p_0\gamma}}\right] \tag{10.34}$$

The terms appearing in the perfect gas formulation and a corrective term depending on Van der Waals coefficients (in the square brackets) are evidenced. The additional term depends only on zeroth-order density and pressure. Clearly, the perfect gas formulation is recovered in the limit $a'\to 0$ and $b'\to 0$.

10.1.1 Temporal integration

The *Low Mach number* expansion of the entire Navier-Stokes system coupled with the Van der Waals equation of state reads

$$\frac{\partial\rho_0}{\partial t}+\boldsymbol{\nabla}\cdot(\rho\boldsymbol{u})_0=0 \tag{10.35}$$

$$\frac{\partial(\rho\boldsymbol{u})_0}{\partial t}+\boldsymbol{\nabla}\cdot[(\rho\boldsymbol{u})_0\boldsymbol{u}_0]=\frac{1}{Re}\boldsymbol{\nabla}\cdot\boldsymbol{\tau}_0-\boldsymbol{\nabla}p_2+\frac{1}{Fr^2}\rho_0\boldsymbol{e}_z \tag{10.36}$$

$$\boldsymbol{\nabla}\cdot\boldsymbol{u}_0=\frac{\gamma-1}{\gamma p_0}\left[\frac{\gamma}{(\gamma-1)\,RePr}\boldsymbol{\nabla}\cdot(k\boldsymbol{\nabla}\vartheta)_0+\left(\sum_\alpha Ce_\alpha\,Da_\alpha\,\omega_\alpha\right)_0\right]\left[\frac{1}{1+\dfrac{(\gamma-2)\,a\rho_0^2}{p_0\gamma}+\dfrac{2ab\rho_0^3}{p_0\gamma}}\right] \tag{10.37}$$

$$\frac{\partial(\rho Y_{R0})}{\partial t}+\boldsymbol{\nabla}\cdot(\rho\boldsymbol{u}Y_R)_0=\frac{1}{ReSc_R}\boldsymbol{\nabla}\cdot(\rho_0 D_R\boldsymbol{\nabla}Y_R)_0+Da_R\,\omega_{R0} \tag{10.38}$$

$$\vartheta_0=\frac{p_0}{\rho_0}\left(1+a\frac{\rho_0^2}{p_0}\right)(1-b\rho_0)\,. \tag{10.39}$$

Since, in this context, the combustion process is not considered the terms dealing with the chemical reaction can be neglected here and only one specie equation is evolved to address the dynamics of a passive scalar. The system is made by seven equations and seven unknown

variables, ρ_0, $(\rho\boldsymbol{u})_0$, p_2, $(\rho Y)_{R0}$ and ϑ_0, we highlight that the free jet configuration ensures that the thermodynamic pressure p_0, constant in space, can be considered also constant in time, hence can be assumed as an external parameter, while the chemical reaction rate ω_{R0} depends on the temperature and the reactant concentration as shown by equations (4.2) and (4.3). The peculiar feature of the new system is the presence of the second order pressure p_2 in the momentum equation without a dedicated equation. The system is in this way similar to the incompressible Navier-Stokes equations where the dynamic pressure ensures the zero-divergence field velocity. In this context the pressure p_2 constrains the velocity divergence to the value ascribed by the equation (10.37).

As a matter of fact the numerical integration starts from the all variable fields at the "nth" iteration. The main lines of the solution algorithm, based on a projection method, go as follows.

- The mass conservation equation is used to update the fluid density.
- The momentum equation (deprived of the hydrodynamic pressure term) combined with the density is used to find the unprojected velocity field.
- The species continuity equation is used to advance in time $\rho Y_{\alpha 0}$.
- The velocity is projected enforcing the local value of the divergence which depends on the diffusive temperature flux and combustion heat release.

10.1.2 Parameter Setting

As well known from classical thermodynamics, the heat capacity at constant pressure and volume are obtained by the enthalpy $h^* = e^* + p^*/\rho^*$ and the internal energy e^* variation with temperature at constant pressure and volume, respectively,

$$c_p = \left.\frac{\partial h}{\partial \theta}\right|_p \qquad c_v = \left.\frac{\partial e}{\partial \theta}\right|_v \tag{10.40}$$

hence their ratio evaluated in the dimensionless form yields,

$$\gamma = \gamma^{\,pg}\left[\frac{3}{5} + \frac{2}{5}\frac{1}{1 - 2a\frac{\rho_0}{\theta_0}\,(1 - b\rho_0)^2}\right]. \tag{10.41}$$

where with $\gamma^{\,pg}$ we indicate the perfect gas heat coefficient ratio. In addition we express the non-dimensional Van der Waals constant starting from the relations (3.3),

$$b = \frac{1}{3}\frac{\rho_\infty}{\rho_c} \qquad a = 3\,\frac{p_c}{p_\infty}\left(\frac{\rho_\infty}{\rho_c}\right)^2 \tag{10.42}$$

so that the ratio between the reference, p_∞ and ρ_∞, and critical, p_c and ρ_c, quantities provides the thermodynamic state of the studied phenomenon. We highlight that in this way the choice of the gas properties, critical conditions, do not influence the value of the non-dimensional Van der Waals constant, since they depend on the ratios p_∞/p_c and ρ_∞/ρ_c, which do not depend on the specific fluid considered for the numerical simulation.

10.2 Turbulent round supercritical jet

In this section the dynamics of a simple variable-density jet is addressed in order to exploit the effects of supercritical thermodynamic conditions on the structures of the jet such as the self-similar behavior, spreading rate, velocity and scalar decay.

The simulations involve a jet injected with a density smaller than the critical one, $\rho_j < \rho_c$, where the subscript "j" labels the jet, in an environment at weakly super-critical pressure with density greater than the critical one, $\rho_{ext} > \rho_c$. The equation system presented in the § 10.1 is discretized to perform the direct numerical simulation (DNS).

The Eulerian algorithm discretizes the system in a cylindrical domain. Spatial discretization is based on central second order finite differences in conservative form on a staggered grid while the convective term of scalar equations is dealt with by a bounded central difference scheme to avoid spurious oscillations. Temporal evolution is performed by a low-storage third order Runge-Kutta scheme. Dirichlet (prescribed velocity) conditions are enforced at the inflow, by using a cross-sectional plane of a periodic turbulent pipe flow, obtained by a companion time-evolving DNS. A convective condition is adopted at the outflow, while a traction-free condition is used for the side boundary. More details on the code are available in [22]. Three simulations are performed. The first one reproduces a cold jet of real gas ($S1$) injected in a environment with a pressure weakly supercritical $p/p_c \simeq 1.18$. The density of the environment is one tenth the jet one $\rho_j/\rho_{ext} = 10$, ensuring that $\rho_j < \rho_c < \rho_{ext}$, while the ratio between the jet and environment temperature is $\theta_{ext}/\theta_j \simeq 4.$. The other two simulations $S2$, $S3$ reproduce two perfect gas jets matching either the temperature ratio $\theta_{ext}/\theta_j = \rho_j/\rho_{ext} = 4$ or the density ratio $\theta_{ext}/\theta_j = \rho_j/\rho_{ext} = 10$ of the first one, respectively. All simulations are performed for a Reynolds number based on the jet diameter, equal to $Re_D = U_0 D/\nu_\infty = 6000$, with U_0 the bulk velocity. The thermodynamic parameters mimic one of the experiments with the cold jet of nitrogen in nitrogen environment performed by *Mayer et al.* in [100].

The computational domain, $[\phi_{max} \times R_{max} \times Z_{max}] = [2\pi \times 6.2D \times 10D]$ is discretized by

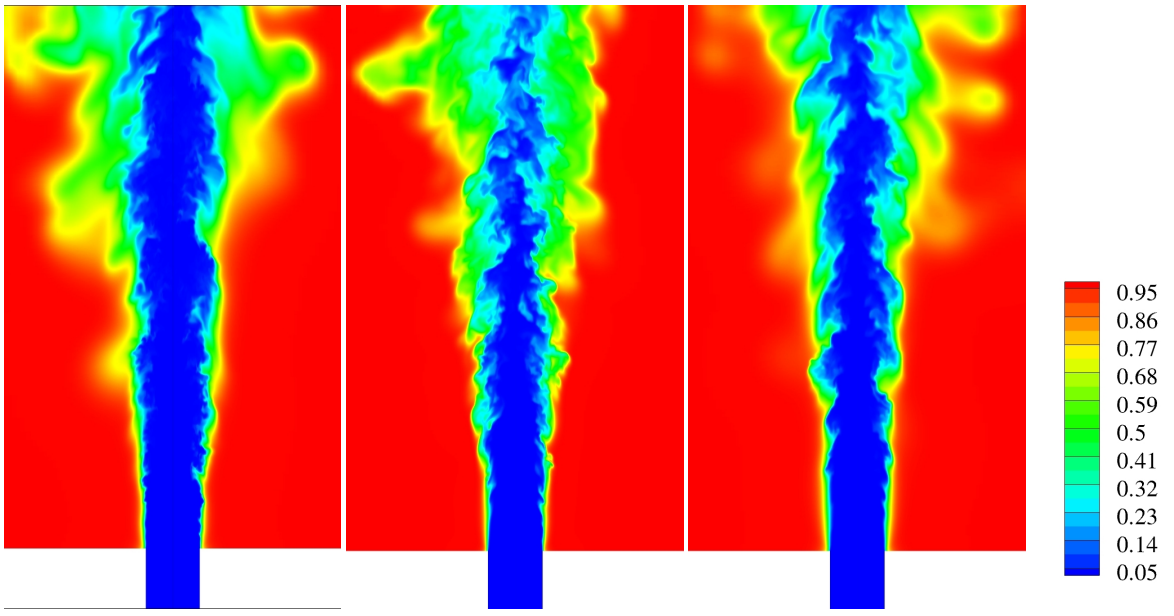

Figure 10.1 Snapshot of normalized temperature $(\theta - \theta_{ext})/(\theta_j - \theta_{ext})$ field of the three simulations. From top-left: real gas with $\rho_j/\rho_{ext} \simeq 10.$, perfect gas with $\rho_j/\rho_{ext} \simeq 4.$, perfect gas with $\rho_j/\rho_{ext} \simeq 10.$.

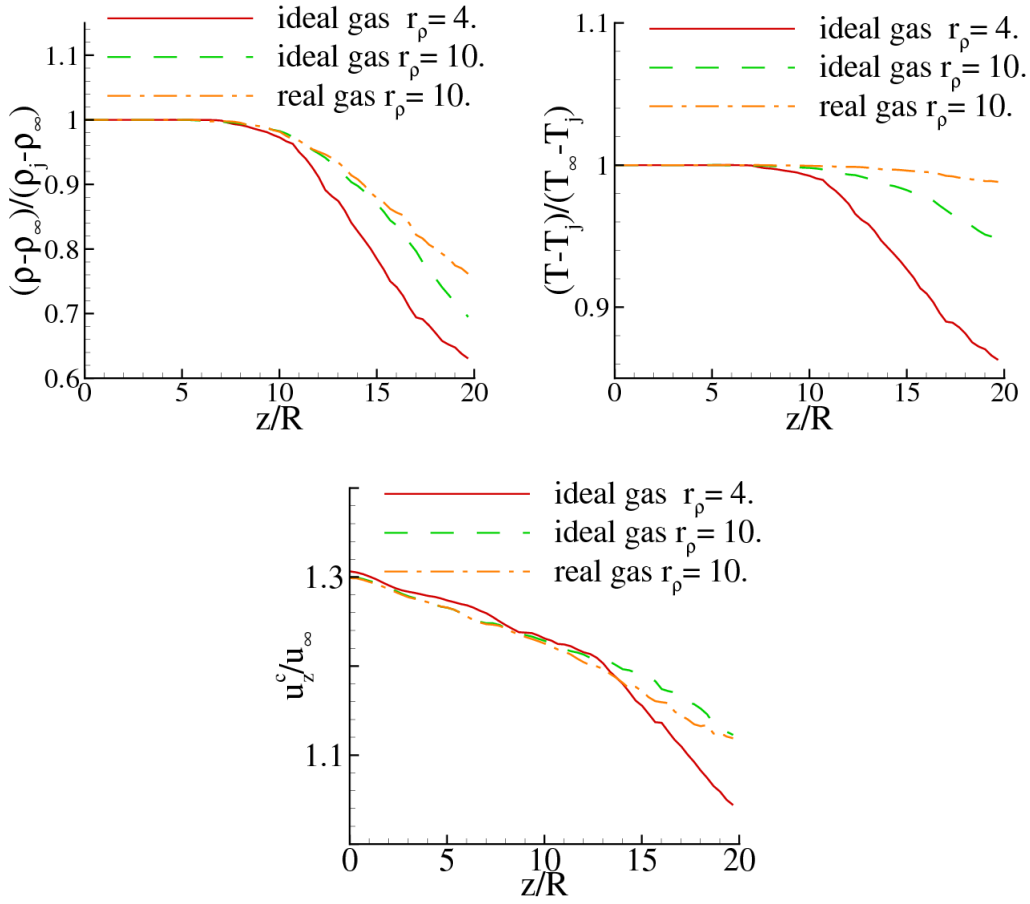

Figure 10.2 Mean axial profiles of density (top-left panel) normalized with the injection and surroundings density $(\rho - \rho_j)/(\rho_{ext} - \rho_j)$, normalized centerline temperature (top-right panel) $(\theta - \theta_{ext})/(\theta_j - \theta_{ext})$ and normalized centerline axial velocity (bottom panel) u_z^c/u_∞

$N_\phi \times N_r \times N_z = 128 \times 201 \times 600$ nodes with a stretched mesh in the radial direction to assure a resolved shear layer. The grid size in the jet region is about two/three times the Kolmogorov scale, and is able to accurately capture the strong density gradients which develops in the flow, [95]. After reaching the statistical steady state, about two hundred complete fields, separated by $0.125\, D/U_0$, are collected for statistical analysis.

In the figure 10.1 the instantaneous field of normalized temperature is presented for the three simulations. Apparently the density ratio has a larger influence on the jet than the temperature ratio. The core of the jet in the $S2$ case (middle panel) exhibits in fact a temperature greater than the real gas jet (left panel). Also the perfect gas jet (right panel) with the same density ratio ($S3$) of the real gas flow, has an instantaneous temperature grater though the difference is sensibly smaller than the previous case $S2$ vs $S1$. The temperature difference in the latter case are probably associated with the thermodynamic properties of the real gas near the critical point.

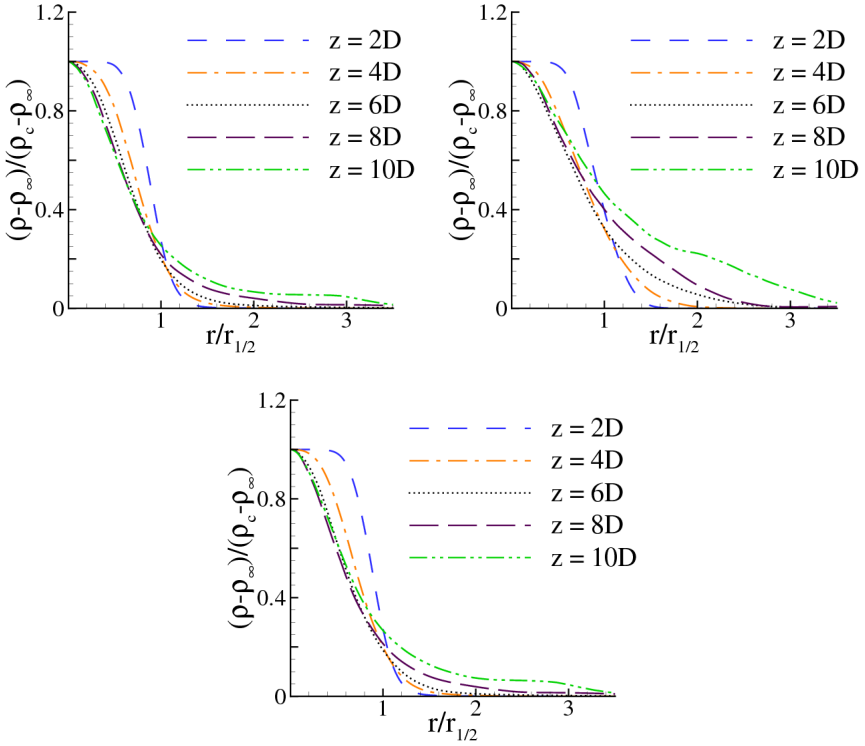

Figure 10.3 Mean radial profiles of density normalized with the centerline and surroundings density, $(\rho - \rho_{ext})/(\rho_c - \rho_{ext})$. The radial coordinate is normalized with the radial distance where the averaged velocity is the half of the corresponding centerline value. From left: real gas with $\rho_j/\rho_{ext} \simeq 10.$, perfect gas with $\rho_j/\rho_{ext} \simeq 4.$, perfect gas with $\rho_j/\rho_{ext} \simeq 10.$.

10.2.1 Results

Figure 10.2 reports the axial profiles of the Reynolds averaged [3] centerline density (left panel), temperature (middle panel) and velocity (right panel). These mean quantities confirm that the density ratio determines the jet dynamics more than the temperature ratio. The decay of density and of the normalized temperature is more rapid in the configuration $S2$. The behavior in the dense-gas simulation, $S1$, and for the perfect gas at matching density ratio, $S3$, is quite similar although in the far field the perfect gas jet presents a weaker reduction of both density and temperature. In the velocity plots, for $S2$ a curve slope variation occurs at $z \simeq 12D$, while the other jets tend to maintain the same profile slope. Figures 10.3 and 10.4 provide the mean density and velocity profiles, respectively, as a function of the radial coordinate at five different axial locations. Mean quantities are normalized by their centerline and surroundings values, while the radial coordinate is normalized by the jet half-width $r_{1/2}$, radial distance where the mean axial velocity is the half of the corresponding centerline value. The density profiles, figure 10.3, highlights once more that the density ratio plays a crucial role in the jet dynamics. Since simulations $S1$ and $S3$ exhibit a similar behavior of the radial profiles, while the $S2$ differs considerably. In addition, only the density profiles of $S1$ and $S3$ seem to collapse on a unique self-similar curve at small axial distances, $z = 8 - 10D$, presenting noticeable differences for radial distances larger than a couple of $r_{1/2}$. The existence of self-similarity is observed also in

[3] starting from an instantaneous quantities $q = q(\varphi, r, z; t)$ the Reynolds averaged is defined as a mean value computed in the time and in the azimuthal direction (which is statistically homogeneous as stated in the chapter 5). The mean value of $q(\varphi, r, z; t)$ is $Q(r, z) = \langle\langle q(\varphi, r, z; t)\rangle_\varphi\rangle_t$.

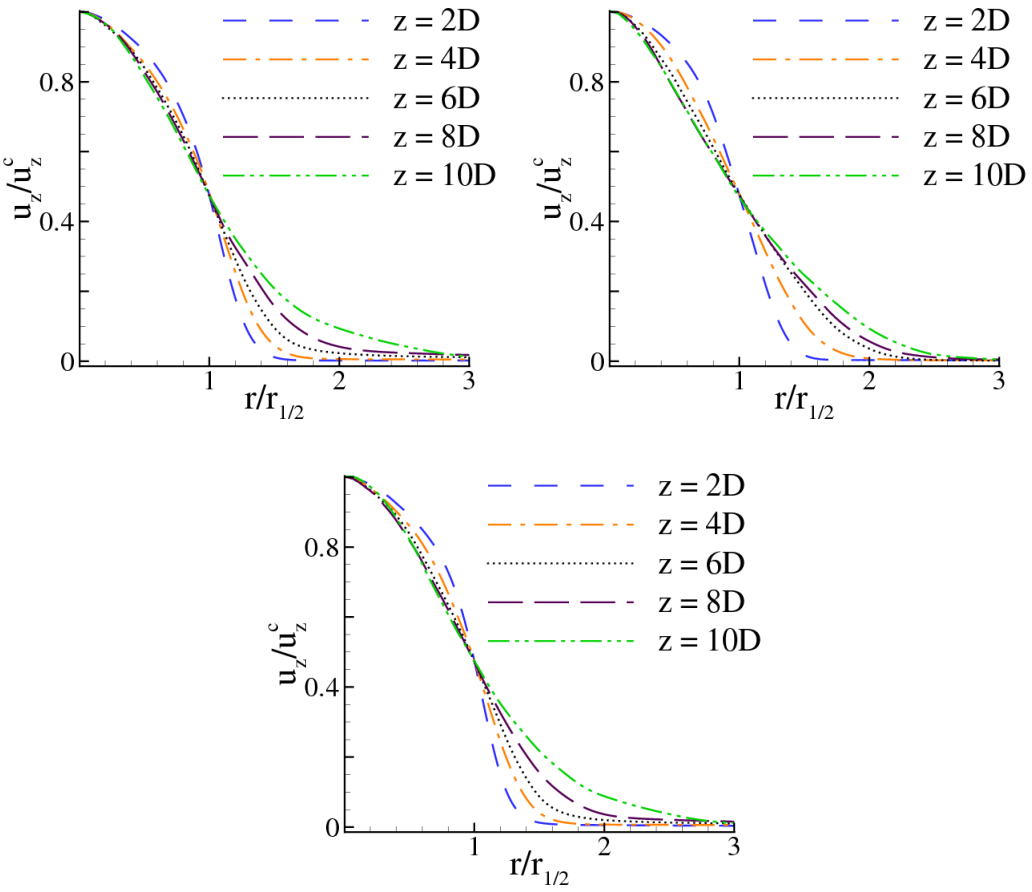

Figure 10.4 Mean radial profiles of axial velocity normalized with the centerline mean velocity, u_z/u_z^c. The radial coordinate is normalized with the radial distance where the averaged velocity is the half of the corresponding centerline value. From left: real gas with $\rho_j/\rho_{ext} \simeq 10.$, perfect gas with $\rho_j/\rho_{ext} \simeq 4.$, perfect gas with $\rho_j/\rho_{ext} \simeq 10.$.

the $2D$ large eddy simulation provided in [101] even if at axial distances quite larger than the present distances. The axial velocity profiles, figure 10.4, tend to collapse on a unique self-similar curve in all jets, also for that with the density ratio of 4 ($S2$, middle panel). Nonetheless also for the velocity appreciable differences emerge at the edge of the jet, more than $r_{1/2}$.

10.2.2 Conclusions

A numerical algorithm to deal with Low-Mach number supercritical flows is proposed and used to perform a DNS of real gas turbulent jet in cryogenic conditions. As a matter of fact the low-Mach number expansion proposed by Majda & Sethian for the ideal gas jet combustion is here generalized at the real gas case, in order to take into account the peculiar effects occurring in the supercritical or near critical thermodynamics conditions. The effect of the real gas EOS is analyzed comparing the results with two simulations of ideal gas matching the density ratio in the first and the temperature ratio in the other. The real gas jet shows a density/temperature core less influenced by the surrounding environment, in respect to perfect gas jets. Hence the mixing in real gas jets appear reduced in respect to ideal conditions. Besides the mean axial velocity and density profiles show a tendency to a self-similar behavior as in the incompressible limit. Nonetheless, difference in the outer region of the jet emerges that could disappear at

larger axial distances.

Chapter 11

Supercritical coaxial jet

The conditions occurring in liquid rocket engines are such that after ignition the thermodynamic conditions of the injected reactants are near or entirely above their critical state.

As stated in the section § II and explained in the previous chapter, the effects of the near critical conditions on the gas behavior and on jet structures and dynamics are addressed by means of a suitable equation system and thermodynamic assumptions.

The injectors display specific geometric characteristic design to have great influence on mixing process and combustion efficiency [30]. In particular, each injector is characterized by two coaxial jet, the inner one discharges a high density, generally liquid-like, oxygen and the outer one introduces the gaseous fuel (hydrogen or methane) in the high pressure and temperature chamber where the combustion process occurs. The most recent injectors induce an additional swirling motion to the external jet to enhance the mixing process which allows to design smaller and smaller combustion chambers [30].

The aim of this chapter is to provide the main results of a Direct Numerical Simulation of a coaxial variable-density nitrogen jet discharging in an environment of gaseous nitrogen at standard temperature ($\theta = 300K$) and pressure high enough to reach the critical thermodynamics conditions of the injected fluids in particular of oxidizer injected in the core of the injector.

11.1 Model and numerical method

The DNS of coaxial real-gas jet is performed employing the cylindrical domain with dimension $[\varphi_{max} \times R_{max} \times Z_{max}] = [2\pi \times 18R \times 20R]$ with $[N_\varphi \times N_R \times N_Z] = [128 \times 281 \times 600]$ collocation points. In the radial direction a grid stretching is applied to resolve the shear occurring at the boundary between the internal and the external jet and between the external jet and the surrounding environment. Since the Kolmogorov scale at the inlet of the jet is of order of $\eta = 0.005D$, the typical grid size, $\Delta r = 0.00625D$, is able to accurately capture the finest scale of turbulence. We highlight that the present discretization also ensures the capturing of the strong density gradients, as shown in § 8.

The simulation performed deals with a coaxial nitrogen jet in the transcritical thermodynamic condition (Simulation A: SA). The geometry and thermodynamic parameters are chosen to reproduce the coaxial jet experiments presented by *Mayer et al.* in [100]. In particular we assume a nitrogen coaxial jet discharging in an environment, filled with gaseous N_2, with a pressure equal to $4.0\,MPa$, slightly greater than the nitrogen supercritical pressure $p \simeq 1.178\,p_c \simeq 4.MPa$. In addition the internal jet is injected with a density greater than the critical one $\rho \simeq 1.04\rho_c$,

	inner jet	outer jet	surrounding environment
p	p_∞	p_∞	p_∞
ρ	ρ_∞	$0.1\,\rho_\infty$	$0.1\,\rho_\infty$
ϑ	ϑ_∞	$4\,\vartheta_\infty$	$4\,\vartheta_\infty$
U_{inj}	U_∞	$4.\,U_\infty$	–
$(\rho U)_{inj}$	$\rho_\infty U_\infty$	$0.234\,\rho_\infty U_\infty$	–
$(\rho U^2)_{inj}$	$\rho_\infty U_\infty^2$	$1.296\,\rho_\infty U_\infty^2$	–

	inner jet	outer jet	surrounding environment
p	p_∞	p_∞	p_∞
ρ	ρ_∞	$0.1\,\rho_\infty$	$0.1\,\rho_\infty$
ϑ	ϑ_∞	$10\,\vartheta_\infty$	$10\,\vartheta_\infty$
U_{inj}	U_∞	$4.\,U_\infty$	–
$(\rho U)_{inj}$	$\rho_\infty U_\infty$	$0.234\,\rho_\infty U_\infty$	–
$(\rho U^2)_{inj}$	$\rho_\infty U_\infty^2$	$1.296\,\rho_\infty U_\infty^2$	–

Table 11.1 Thermodynamic and physical conditions of jets injection and surrounding environment normalized with the reference quantities. The last two rows are the mass and the momentum flow rate, respectively, at the jets inlet divided by πR^2. Top table: real gas jet conditions where the reference quantities, marked with subscript '∞', are: $p_\infty = 1.178 p_c$, $\rho_\infty = 1.0424 \rho_c$ and $\vartheta_\infty = 1.0417 \vartheta_c$. Bottom table: perfect gas jet conditions with reference quantities: $p_\infty = 0.03 p_c$, $\rho_\infty = 3.9 \times 10^{-6} \rho_c$ and $\vartheta_\infty = 2.37 \vartheta_c$.

while the external jet is injected at a density about ten times lower, similar to the surrounding environment, in order to ensure $\rho_j < \rho_c < \rho_{ext}$ (where the subscripts "j" and "c" stand for jet and critical, respectively). The velocity instead is sensibly larger than the internal jet, about four times. We highlight that in order to perform a Direct Numerical Simulation, our Reynolds number is selected sensibly smaller than the experimental one [100]. Non-dimensional features of present simulation are summarized in table 11.1 top panel. In order to address the effects of the supercritical state on the jet dynamics and mixing process, a similar simulation is performed at a thermodynamic condition such that the injected gas can be considered perfect (Simulation B: SB). To this purpose, we consider the same geometry and inlet velocities, but we assume a surrounding pressure of $0.1\,MPa$, inner jet density of $1.0\,kg/m^3$ and temperature of $300\,K$. Table 11.1, bottom panel, summarizes the perfect gas jet non-dimensional parameters. Tables 11.1 highlight that the two simulations are substantially the same; the only difference is in the temperature difference between the inner and the outer jet. In particular, while in the perfect gas case the density ratio $\rho_{inner}/\rho_{outer} = 10$ results in the temperature ratio $\vartheta_{inner}/\vartheta_{outer} = 0.1$, in the real gas jet the temperature ratio is of about $\vartheta_{inner}/\vartheta_{outer} = 0.25$, where the subscripts "inner" and "outer" pertain to the inner and outer jet, respectively. We observe that all the differences in structures or jet dynamics between the two simulations could be ascribed only to this difference in the temperature ratio.

The two simulations are performed at a Reynolds number based on the internal jet diameter, equal to $Re_D = U_\infty D/\nu_\infty = 6000$, with U_∞ the bulk velocity. The coaxial jet has the internal diameter equal to $2.4R$ and the external equal to $3R$; figure 11.1 presents a schematic design of the injector. The dynamic viscosity and thermal and species conductivity functions of pressure and temperature are provided by [102]. The specific heat constant pressure and volume ratio $\gamma = c_p/c_v$ is tuned as described in § 10.1.2 by relation (10.41) where $\gamma^{\,pg}$ is assumed equal to 1.3. The Prandtl and Smith number are equal to $Pr = 4.36$ and $Sm = 0.6$ and to $Pr =$

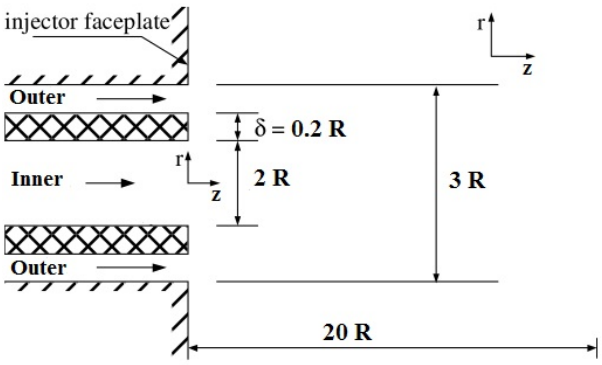

Figure 11.1 Schematic diagram of the shear coaxial injector used in the present simulations. Liquid-like density nitrogen N_2 is injected through the "Inner" jet while the "Outer" jet discharges gaseous nitrogen N_2 in the high pressure environment. All dimension are normalized with the Inner jet radius.

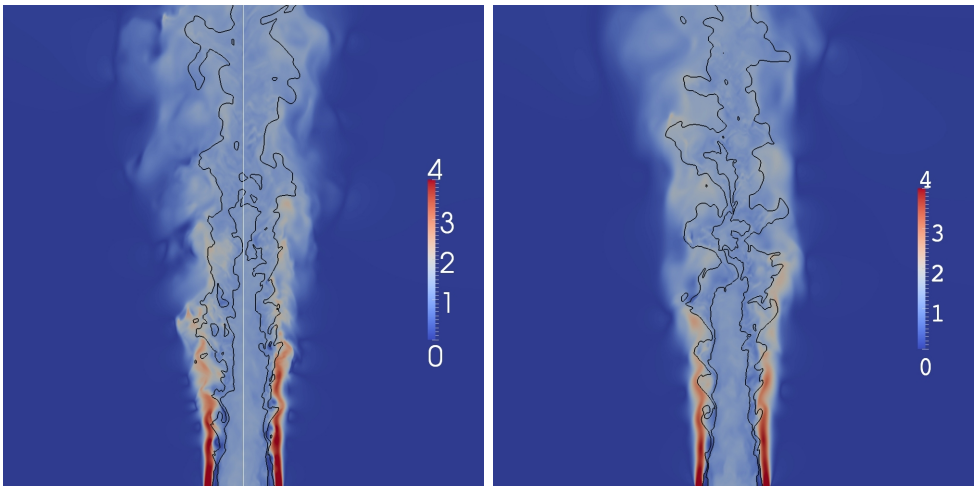

Figure 11.2 Instantaneous configuration of gaseous (left panel) and supercritical (right panel) coaxial jets. Contour denotes the axial velocity while solid line are the constant density isolevel $\rho = .2$ and $\rho = .9$.

0.6 and $Sm = 0.6$ in the real and perfect gas jet, respectively. These dimensionless numbers are determined through the transport coefficients evaluated at the reference thermodynamic conditions, imposed by $\rho_{ratio} = \rho_\infty/\rho_c$ and $p_{ratio} = p_\infty/p_c$. Buoyancy contribution is neglected hence the Froude number is equal to $Fr = 0$.

After reaching the statistical steady state, about two hundred complete fields, separated by $0.125\, D/U_\infty$, are collected for statistical analysis.

11.2 Results

The comparison between the gaseous (left panel) and supercritical (right panel) jets is presented in figure 11.2. The instantaneous field of the velocity is shown with contour style, while the solid lines denote the constant density profiles at $\rho = 0.9$ and $\rho = 0.2$. The formation of specific structures in the supercritical jet can be visually detected in the shear layer rising from the interaction between the two streams, as showed in the experimental snapshot provided in [7, 103]. The same structures are detectable also in the gaseous jet even if their length appears smaller and more corrugated by the turbulent structures.

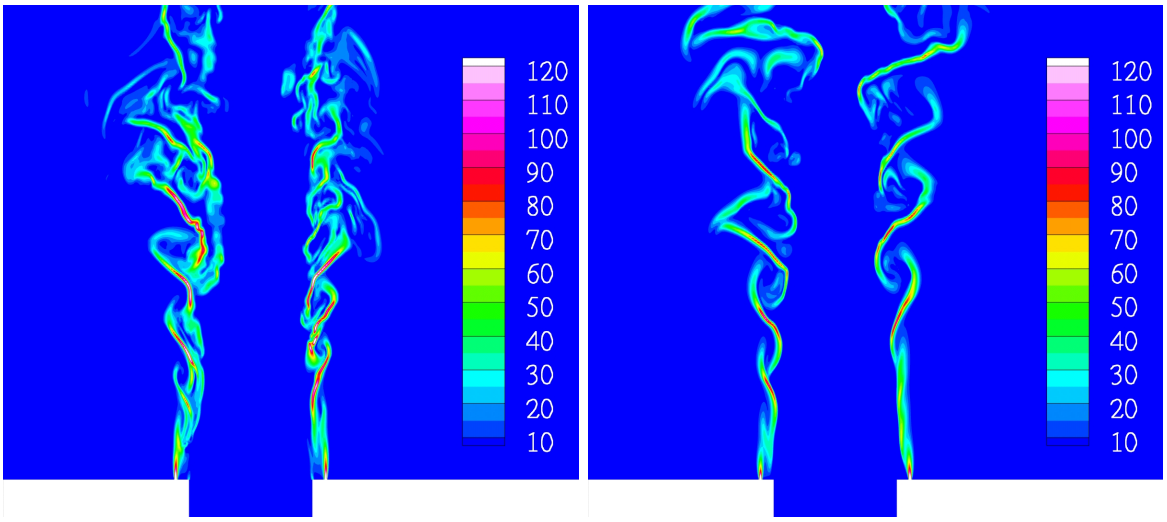

Figure 11.3 Temperature gradient magnitude $\sqrt{\boldsymbol{\nabla}\vartheta \cdot \boldsymbol{\nabla}\vartheta}$ field for the low pressure ideal gas jet (left panel) and for the high pressure supercritical fluid jet (right panel).

The specific structures present in the high pressure jet appear to be similar to ligaments occurring in the breakup of a liquid jets; see [27]. Actually the finger-like structures, also called "ligaments" can be ascribed to similar cinematic mechanism but different chemical phenomenologies. The liquid jet in the same configuration is characterized by two non-miscible phases, liquid and gaseous, and no diffusion into each other occurs. Due to shear forces, the gas stream stretches the liquid, forming finger-like structures which elongate until the capillary instability promoted by the surface tension acting at the liquid-gas interface, induces droplet formation [27, 104]. In the supercritical jet conditions, there is a continuous transition from an high liquid-like density to a low gas-like density fluid, since the interface and the corresponding surface tension do not exist. In this context the finger-like structures observed in figure 11.2 (right panel) are due to different physical reasons. The "ligament" formation is related to the low diffusion of the high density structures persisting in the low density region that depend on the differential effects promoted by temperature gradient. If we consider the continuity equation (10.35) in which the velocity divergence is partially replaced by the energy equation (10.37), it is possible to highlights the diffusion term,

$$\frac{\partial \rho_0}{\partial t} + \boldsymbol{u}_0 \cdot \nabla \rho_0 = -\frac{\rho_0}{p_0} \frac{1}{RePr} \boldsymbol{\nabla} \cdot (k \boldsymbol{\nabla} \vartheta)_0 \left[\frac{1}{1 + \dfrac{(\gamma - 2)\, a \rho_0^2}{p_0 \gamma} + \dfrac{2ab\rho_0^3}{p_0 \gamma}} \right] . \tag{11.1}$$

It is clear as diffusion effects are due to the term on right-hand side depending on the temperature gradients and on a function of pressure and density. As a matter of fact as the thermodynamic state approaches the critical point, the weak diffusion effects are smaller compared to the perfect gas thermodynamic conditions hence the fingers-like structures are able to persist in the gaseous external stream. Instead of the liquid jet break up, the droplets formation is inhibited by the absence of the surface tension promoter of the capillary instability in the liquid jet. Figure 11.3 shows the temperature gradient magnitude, $\sqrt{\boldsymbol{\nabla}\vartheta \cdot \boldsymbol{\nabla}\vartheta}$ in the perfect (left panel) and real gas (right panel) jet. Though the temperature difference between the inner

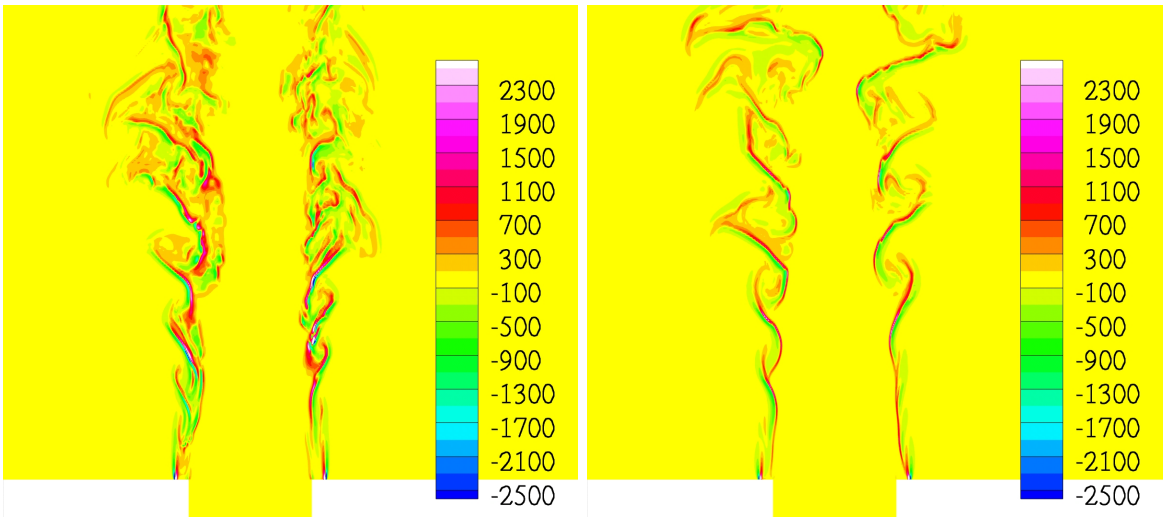

Figure 11.4 Temperature laplacian field for the low pressure ideal gas jet (left panel) and for the high pressure supercritical fluid jet (right panel).

and the outer jet in the real gas case is smaller than the perfect gas jet, the temperature gradients are substantially of the same order of magnitude. This evidence shows that the scales at which the temperature gradients occur are smaller in the supercritical conditions: the boundary between the high/low density regions is thiner in the supercritical jet than in the perfect gas jet. The formation of smaller and smaller scales in the real gas jet is due clearly to the low effects of the temperature diffusion established also in figure 11.4 where the laplacian of temperature field is shown. Some consideration are necessary pertaining the terms in square bracket in equation (11.1). This quantity assumes unity value in the perfect gas jet[1] while it ranges from about 1.01 to about 0.84 in the real gas case, and thus can be assumed irrelevant in the order of magnitude of the diffusion term. The temperature laplacian field 11.4 shows in addition that in the high pressure jet the diffusion process is non negligible in structures thinner than the low pressure case.

This behavior appears clearly in figure 11.5, where the density field and velocity vectors are superimposed. Figure 11.5 shows the magnification of the shear layer region between the two jets, in the left panel the perfect gas jet behavior in the right panel the real one. The presence of structures liquid-like ligaments are visible in the high pressure jet (right panel of figure 11.5), on the other hand the boundary between the two different density region is clearly larger than the expected liquid/gas interface. We highlight that the classical droplet formation occurring in the liquid jet breakup, induced by the surface tension, here is replaced by the gas-like diffusion. The perfect gas jet instead shows the occurrence of shorter structures with a clear diffusion region between the two different density states, see left panel of figure 11.5. Moreover the velocity vectors show the role of the external faster stream in the formation and stretching of the ligaments; the velocity effect seems to be similar between the two investigated configurations and the differences are ascribed to the different temperature ratio between inner and outer jet.

Figure 11.6 shows the instantaneous density isosurface $\rho = 0.5$, denoting the position of two states interface, colored with the local fluid velocity. It is clear as the ligaments with the internal jet density $\rho = 1$ elongate in the external coaxial jet characterized by a greater velocity that stretch them further more. In addition in both cases they present a certain regular spatial

[1] we remember that the perfect gas limit is reached with $a \to 0$ and $b \to 0$

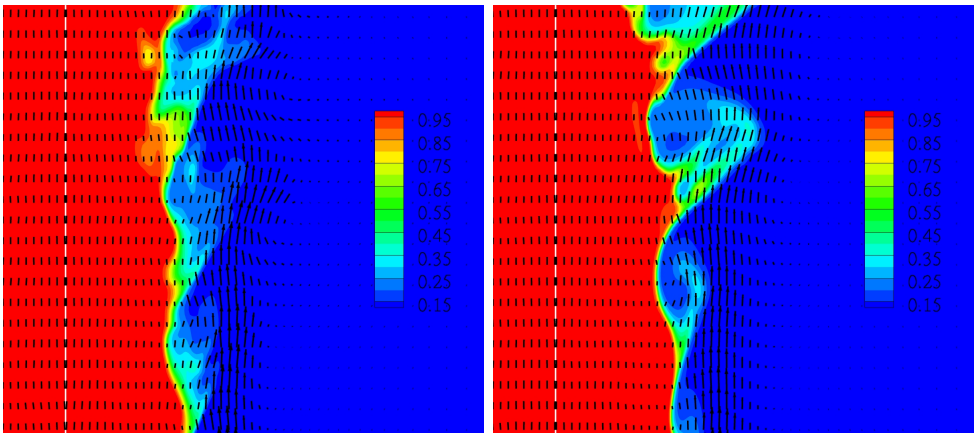

Figure 11.5 Instantaneous density field with in plane velocity vectors. Left panel: perfect gas jet, right panel: real gas jet.

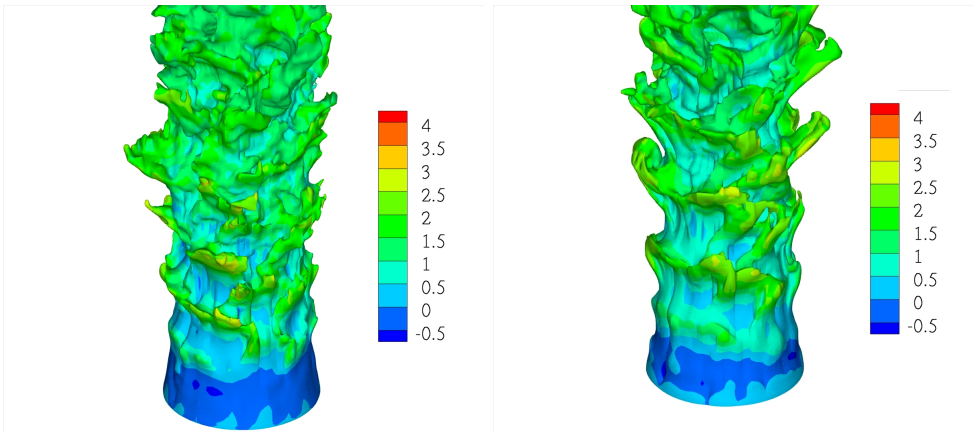

Figure 11.6 Instantaneous density isosurface, color denote the axial velocity. Left panel: perfect gas jet, right panel: real gas jet.

distribution that is maintained well inside in the downstream direction especially for the real gas jet. The same observations are confirmed by figure 11.7 were the isosurface of the axial momentum is colored with the local fluid density. Figure 11.7 shows more clearly that the ligaments in the real gas case (right panel) are more elongated towards the external region respect the perfect gas jet (left panel). In addition the regular distribution of the structures on the jet surface is clear.

The explained mechanism can be well observed in figure 11.8 where five consecutive configurations (from top to bottom) separated by a time gap $\Delta t = 0.25\, R/U_0$ of the near field of supercritical jet are presented. The three columns provide the axial momentum (left column) axial velocity (middle column) passive scalar injected through the external coaxial jet (right panel). In the momentum field it is possible to follow the ligament (indicated by the arrows) formation, growth and evolution. It is clear that the solid trailing edge separating the inner and outer coaxial jets contribute with the velocity difference to generate the classical Kelvin-Helmholtz vortices that are visible in the passive scalar instantaneous fields, right column of figure 11.8. These structures, due to their rotational direction, tend to transport the internal dense gas towards the external environment elongating the structures in the high velocity region. The high velocity stream elongates the ligaments that the vortices extrude from the inner slower

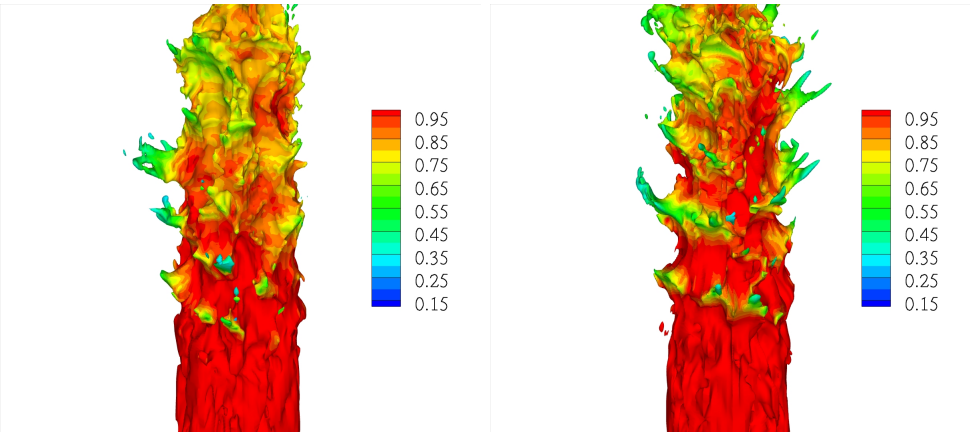

Figure 11.7 Instantaneous axial momentum isosurface, color denote the fluid density. Left panel: perfect gas jet, right panel: real gas jet.

dense jet. In addition figure 11.8 shows that the spatial distribution of the ligaments in the axial direction is mainly influenced by the spatial distribution of the vortex structures generated by the interaction between a variable density shear layer and the geometrical features of the jet inlet.

On the other hand in the perfect gas jet evolution, showed in figure 11.9, the ligament formation is interrupted by the high diffusion process. In fact the dynamics predicted by the external high velocity stream tends also in this case to extrude some high density finger-like filaments from the inner jet. However in this case, unlike the high pressure case, the stretching does not occur due to the diffusion and disappearing of these extruded structures. The structures occurring in the low pressure flow are shorter than those of the high pressure jet, which is ascribed to the different diffusion as demonstrated by the temperature gradient and Laplacian, see figures 11.3 and 11.4.

The characteristic of this phenomenon is the joint effect of the pipe turbulence and the external faster stream which generate a shear layer similar to a Kelvin-Helmholtz instability that is expected to induce the ligaments axial periodicity seen in the instantaneous configurations 11.6 and 11.7.

11.3 Conclusions

The effect of the real gas EOS is analyzed comparing data provided by two simulations. The first one deals with a perfect gas coaxial variable density jet, the second one mimics the coaxial jet of a supercritical high-density nitrogen inner jet surrounded by a high-velocity stream of a gaseous nitrogen.

The supercritical conditions are observed to influence the jet structure and the mixing process. The well known “ligaments” observed in previous experimental images are easily detected in the instantaneous configurations of the jet near field.

The “ligament” formation is clearly due to the coaxial jet geometry and conditions like the momentum ratio between the inner and outer jet and to the specific thermodynamics conditions. The trailing edge separating physically the inner and the outer jet combined with the high velocity ratio between the coaxial jet promotes the formation of the classical vortices characteristic of the Kelvin-Helmholtz instability. This structures extrude finger-shaped structures that the

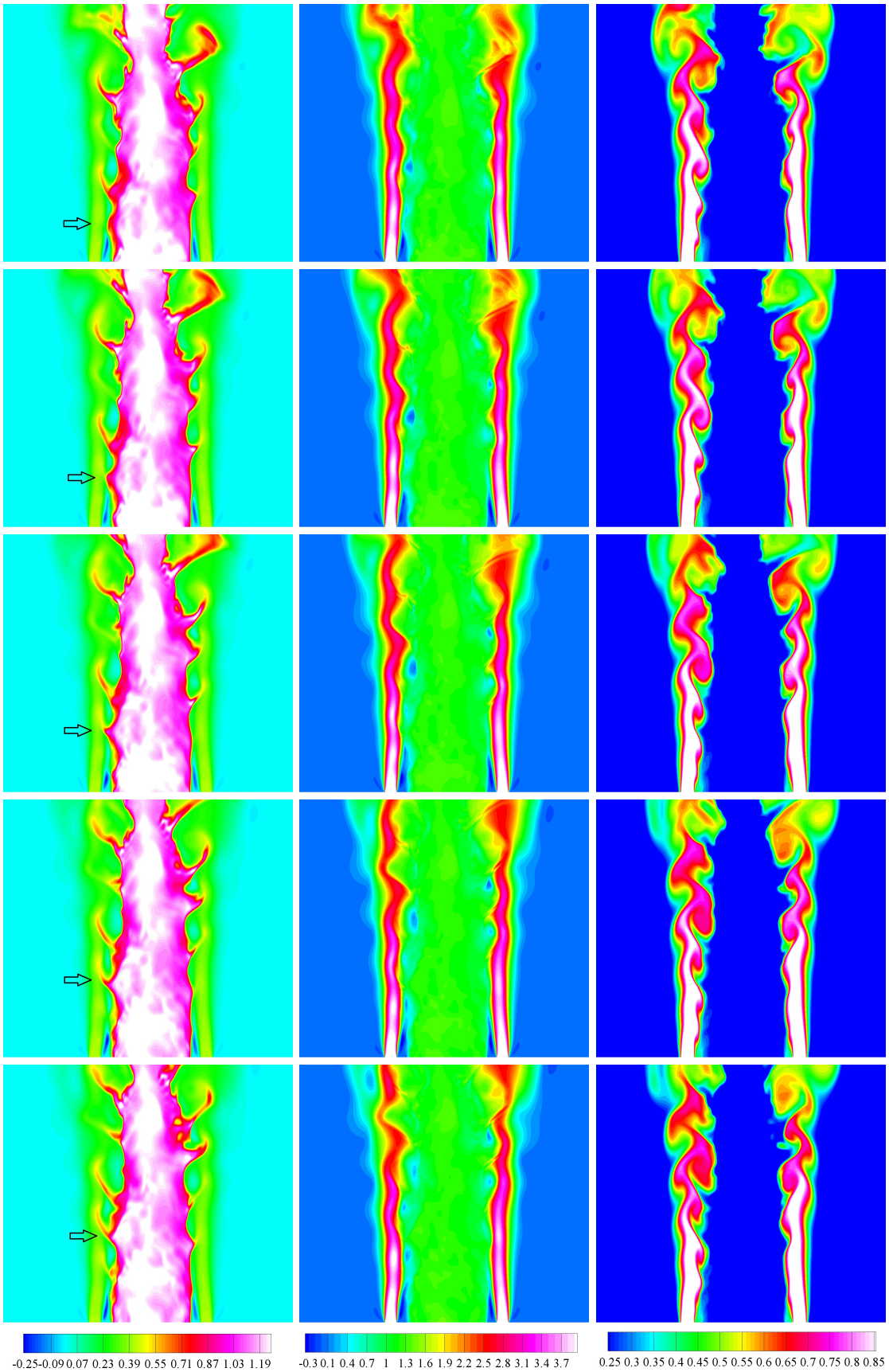

Figure 11.8 Instantaneous configurations of the near field of axial momentum (left column) axial velocity (middle column) and passive scalar (right panel) of the high pressure gas jet. From top to bottom, consecutive instants of time with a gap equal to $0.25R/U_0$. The arrows highlight the "ligaments" evolution.

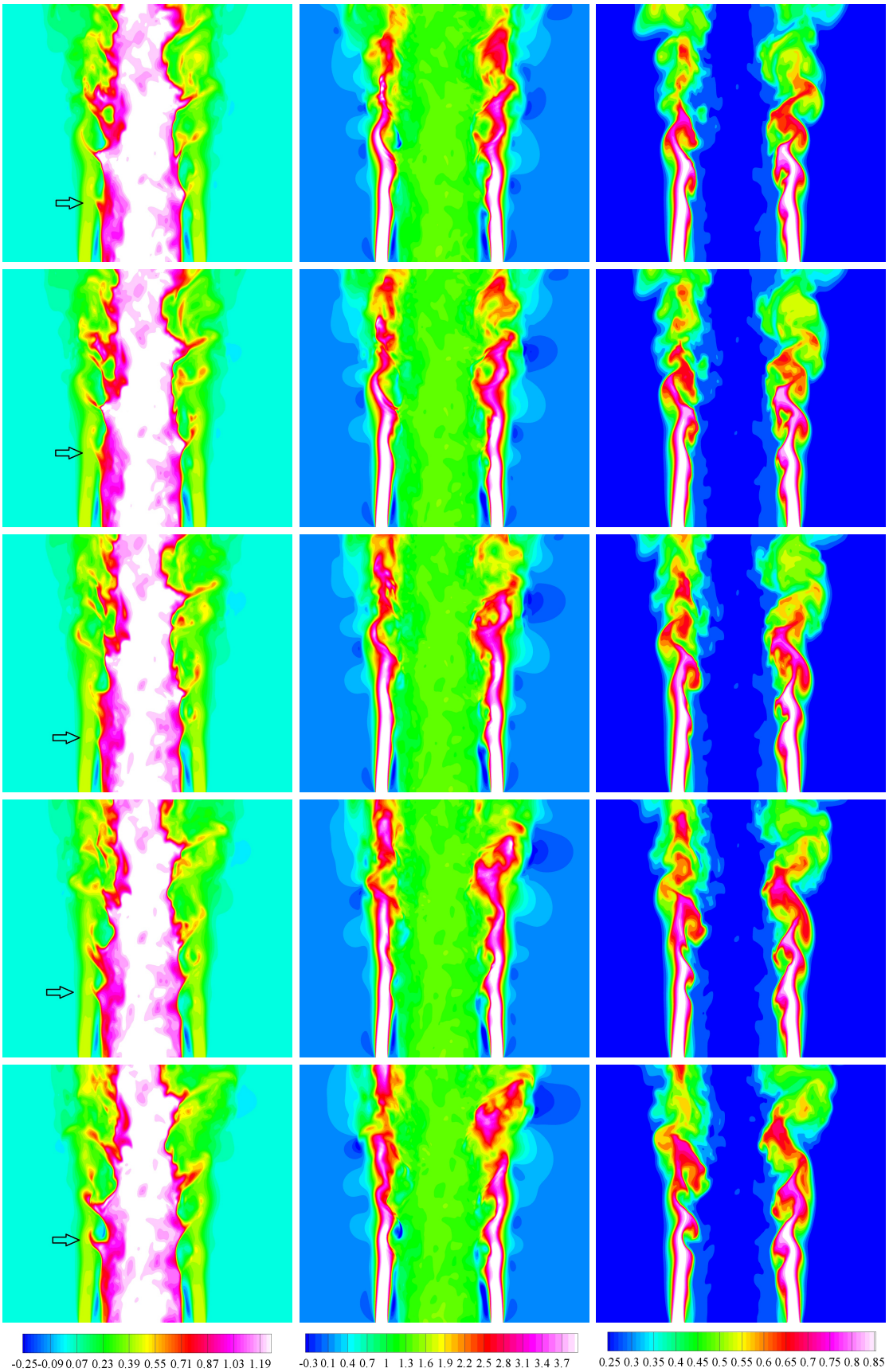

Figure 11.9 Instantaneous configurations of the near field of axial momentum (left column) axial velocity (middle column) and passive scalar (right panel) of low pressure gas jet. From top to bottom, consecutive instants of time with a gap equal to $0.25R/U_0$. The arrows highlight the "ligaments" formation.

high speed stream contributes to elongate well inside the external environment generating the so called "ligaments". This mechanism is promoted in the high pressure jet by the low thermal conductivity demonstrated with temperature gradient and temperature Laplacian instantaneous fields. It is shown that the temperature gradients appears of the same order of magnitude in the high and low pressure jets, albeit the temperature ratio between inner and outer jet in the two investigated configuration is quite different. The consequence is that in the high pressure conditions thiner, but more elongated, structures form respect the perfect gas jet. The temperature Laplacian, on the other side, is useful to explain that the finger-like structures, extruded by the external stream from the inner high density, persist in the high pressure jet while they disappear in the perfect gas conditions.

The instantaneous configurations shows a certain regular spatial distribution of these structures in correspondence of the shear layer generated between the inner and the outer jets. This regular spatial distribution observed mainly in the near field jet is apparent both in azimuthal and in axial direction. The axial direction distribution is mainly correlated with the regular distribution of the Kelvin-Helmholtz vortices, while the azimuthal correlation is expected to be influenced by the streaks structures coming from the pipe turbulence phenomenology.

Chapter 12

Spatial distribution of particle in turbulent Bunsen jet

The purpose of the present chapter is to discuss recent numerical data [95] concerning the effect of the abrupt acceleration induced by a turbulent thin flame front on the statistical properties of inertial particle spatial distributions. The issue may be relevant for evaluating combined inertia/combustion effects on particles collisions and coalescence. Beyond being of interest in itself, the analysis could be useful in estimating the characteristic dimension of soot particles which grow by coalescence in the burned gas region [59] and in providing indications on the behavior of liquid droplet swarms that can found application in flame temperature control systems [105].

In addition to the more familiar effects observed in cold flows, e.g. ejection from persistent vortical structures and concentration in large strain regions, inertial particles present further interesting characteristics in turbulent premixed combustion. Some of these are more or less known, or expected, e.g. thermophoresis as unbalanced thermal drift in presence of extreme temperature gradients, or abrupt mean concentration decrease, induced by the strong thermal expansion across the flame front. Others are new, or at least much less discussed in the scientific literature, and associated with the sudden acceleration across a thin fluctuating turbulent front.

In order to address these combined effects of inertia and combustion on particle motion and preferential concentration, a direct numerical simulation (DNS) of a turbulent premixed Bunsen flame at Reynolds number $Re_D = 6000$ has been performed [95]. The flow is endowed with four different particle populations evolved by a Lagrangian tracking method. The system consists of the low-Mach number formulation of the Navier-Stokes equations equipped with an Arrhenius one-step reaction model which reproduces a lean CH_4/Air premixed flame. In order to isolate the effects of inertia from concurrent phenomena, thermophoresis and gravitational forces are neglected; in the conditions addressed here, they are easily shown to be substantially irrelevant. Because the rough modeling of the chemical kinetics, experimental data from a turbulent Methane/Air Bunsen flame seeded with Alumina particles are used to validate the conclusions drawn on the basis of the numerical simulation.

A suitable Stokes number St_{fl}, called the flamelet Stokes number, expressed in terms of the characteristic time scale of the flame front, is found to properly parameterize the particle dynamics [95]. On top of the expected average density reduction across the front, we find that the front fluctuation leads to strong intermittency of the particle population. Two observables, namely the clustering index [71] and a suitable generalization of the radial distribution function [65] proposed here, are used to quantitatively address the particles tendency to be concentrated in

clusters of variable dimension depending on their inertia. As the main conclusion we find that the particles manifest a strong tendency towards anomalous clustering in the region spanned by the instantaneous turbulent flame front. The effect is found to peak at the flamelet Stokes number of order one. The combined numerical and experimental analysis allows to identify the cause of this phenomenon in the abrupt expansion due to the heat release in the fluctuating flame front coupled with the particle inertia.

The basic modeling background introduced in the next section, assumes that the reader is familiar with the numerical method already briefly illustrated in § 8. The analysis in terms of the clustering index is described in § 12.2, which provides the relevant numerical and experimental observations completed by a short description of the experimental set-up [9]. Section 12.3 is devoted to the radial distribution function and finally a general discussion of the main findings is provided in § 12.4.

12.1 Particle dynamics across the flame front

In order to gain insight into particle motions and to discuss the issues arising from finite inertia effects, the simplified equation of particle dynamics reads as relation (7.3). In most PIV applications, small spherical particles at low concentration are employed such that inter-particle collisions and force feedback on the fluid can be neglected. For applications to turbulent combustion, the typical density ratio between particles and fluid ρ_p/ρ_f is order 10^3, e.g. Alumina or glass particles in air, hence all terms of equation (7.2) proportional to ρ_f/ρ_p can be neglected. In addition, under common conditions, gravity does not affect the accuracy of PIV measurements. On the contrary, thermophoretic motions, negligible for particles with diameter larger than 1 μm [62, 9], may become an issue for submicrometric seedings [82]. In the following we will focus on the sole effects of particle inertia.

Dealing with the features of particles employed in PIV implementations, the particle relaxation time must be small with respect to the smallest characteristic time scale of the flow if extreme accuracy down to the instantaneous gradients is demanded. In fully turbulent flows, the width of the continuous spectrum of time scales is order of the square root of the Reynolds number [1], implying τ_p smaller than the Kolmogorov time scale of the flow $\tau_k = \sqrt{\rho_f \nu/\epsilon}$, with ϵ the energy dissipation rate, corresponding to the fastest frequency of the system,

$$St_K = \tau_p/\tau_K < 1. \tag{12.1}$$

.

In the case of turbulent premixed combustion the abrupt density variation across the instantaneous flame front produces strong fluid accelerations that result in even more restrictive limitations on the relaxation time. For example, when the thermochemical conditions are such to have an instantaneous flame front comparable with the Kolmogorov scale, $\eta = \sqrt[4]{\rho_f \nu^3/\epsilon}$, of the incoming turbulence (flamelet regime), the fastest time scale is defined in terms of the laminar characteristics of the front, i.e.

$$\tau_{fl} = \frac{\delta_L}{\Delta u_{fl}}\,, \tag{12.2}$$

where δ_L is the thermal thickness of the laminar flame and Δu_{fl} the velocity jump across the front. The thermal thickness is defined as $\delta_L = (T_b - T_u)/|\nabla T|_{sup}$, where $|\nabla T|_{sup}$ is the maximum module of the temperature gradient within the flame front and T_b and T_u are the temperature of

burned and unburned mixture, respectively. The thermal expansion, instead, drives the velocity jump $\Delta u_{fl} = S_L\,(T_b/T_u - 1)$, with S_L the laminar flame speed. Using the time scale of the flame τ_{fl}, the relevant Stokes number becomes

$$St_{fl} = \frac{\tau_p\, S_L\,(T_b/T_u - 1)}{\delta_L}\,. \tag{12.3}$$

The proper τ_p should be based on the density and viscosity calculated at a characteristic temperature of the process. In particular, as the temperature experiences a large variation across the front, a suitable choice is the average between hot and cold gases, $T_m = (T_b + T_u)/2$. Since usually $\tau_{fl} < \tau_K$, such flamelet Stokes number controls the ability of the particles to reproduce the velocity statistics of a premixed turbulent flame.

We stress that the flamelet Stokes number defined above depends on the particle relaxation time τ_p and on thermo-chemical properties of the flame, namely temperature ratio T_b/T_u and flamelet thickness δ_{fl}.

We are now in the position to quantify the relevance of gravity for our system. The relative particle/fluid velocity is of the order of the fluid velocity jump across the flame front, $v_{_{REL}} \sim \Delta u_{fl}$. Hence, for a density ratio, $\rho_p/\rho_f = 4. \times 10^3$, we have

$$\left(1 - \frac{\rho_f}{\rho_p}\right)\frac{g\,\tau_p}{v_{_{REL}}} \sim \frac{g\,\tau_p}{\Delta u_{fl}} = \frac{g\,\tau_p}{\mathrm{S}_{fl}\,(T_b/T_u - 1)}\,.$$

With the parameters used in the present simulation, see § 8, $S_{fl}\,(T_b/T_u - 1) \sim 1$, which, for our largest particles, corresponding to Alumina particles of 20μm, yields $g\tau_p/v_{_{REL}} \sim 6. \times 10^{-2}$, suggesting that in the worst case gravity is at least one order of magnitude smaller than Stokes drag. Clearly, the influence of gravity scales with particle diameter squared, hence for 5μm particles the figure decreases to about $3. \times 10^{-3}$.

12.2 Clustering index

12.2.1 Numerical analysis

Figure 12.1 provides the instantaneous configuration of the four particle populations. Colors encode the fluid density at particle positions to help detecting the flame front. The huge variations in the particle concentration between fresh and exhaust gas regions is induced by the sudden expansion due to heat release. According to their inertia, the particles can differently comply with the abrupt fluid acceleration. The effect is not confined to the front proximity and, depending on particle mass, it can influence the particle distribution well into the burned gas region.

A distinguishing feature of the particle distributions is the presence of particle clusters, figure 12.1. Clusters takes place at smaller and smaller scales as the Stokes number is reduced. In the burned region they are particularly well defined for intermediate particle mass, $St_{fl} = 0.54$ and 2.16, with the typical length scale of the voids large enough to be clearly appreciated at first sight. The lightest particles are more evenly distributed both in the burned and unburned regions recovering the tracer-like behavior characterized by a sharp jump of the particle number density across the front.

Particle segregation can be measured by the deviation of the actual particle distribution with respect to randomly distributed independent positions. These reference conditions are

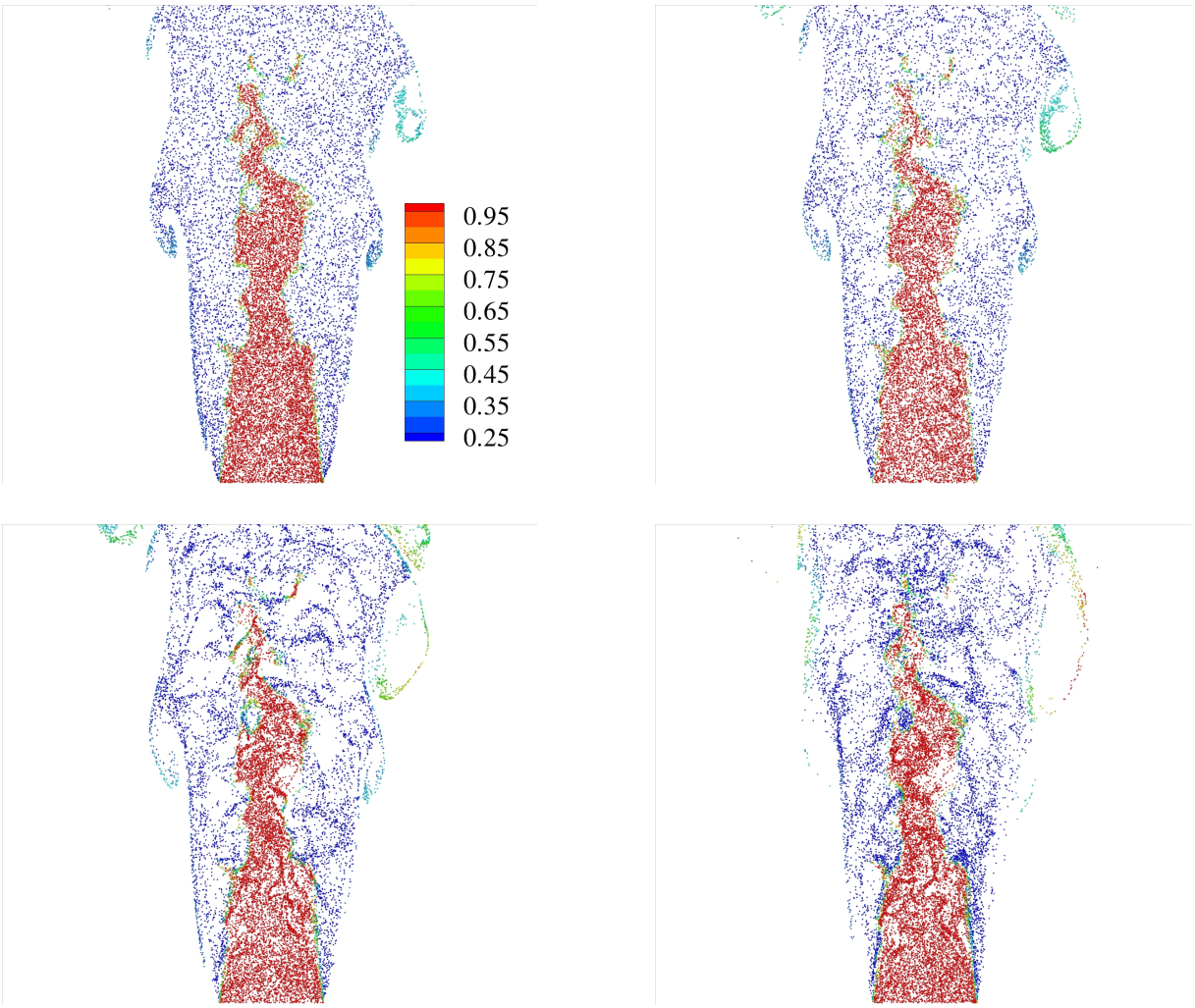

Figure 12.1 Instantaneous particle configuration in a thin slice of width $R/20$ through the axis. Top-left: $St_{fl} = 0.022$; Top-right: $St_{fl} = 0.54$; Bottom-left $St_{fl} = 2.16$; Bottom-right $St_{fl} = 8.65$. Colors encode the fluid density at particle positions, see legend.

expressed by the Poisson distribution which gives the probability $p(n)$ to find n particles in a certain domain Ω of volume ΔV with characteristic length $\ell = \sqrt[3]{\Delta V}$. Once the average particle number $\bar{n}$ is known, the probability density function (pdf) reads:

$$P\left(n, \bar{n}\right) = \frac{\bar{n}^n e^{-\bar{n}}}{n!}. \tag{12.4}$$

A well known feature of Poisson processes is that the variance $\sigma_n^2 = \overline{(n - \bar{n})^2} = \overline{(\delta n)^2}$ equals the mean value $\bar{n}$. When the particles are distributed according to the Poisson distribution they do not segregate. Particle segregation can then be quantified in terms of the departure from the Poisson distribution measured by the clustering index [71]

$$K = \frac{\overline{(\delta n)^2}}{\bar{n}} - 1. \tag{12.5}$$

From the definition it is clear that a Poisson distribution implies $K = 0$, consistently with the absence of any clustering or preferential localization effect. The smaller the ratio of variance to mean value is, the more uniformly distributed the particle are. This corresponds to a negative

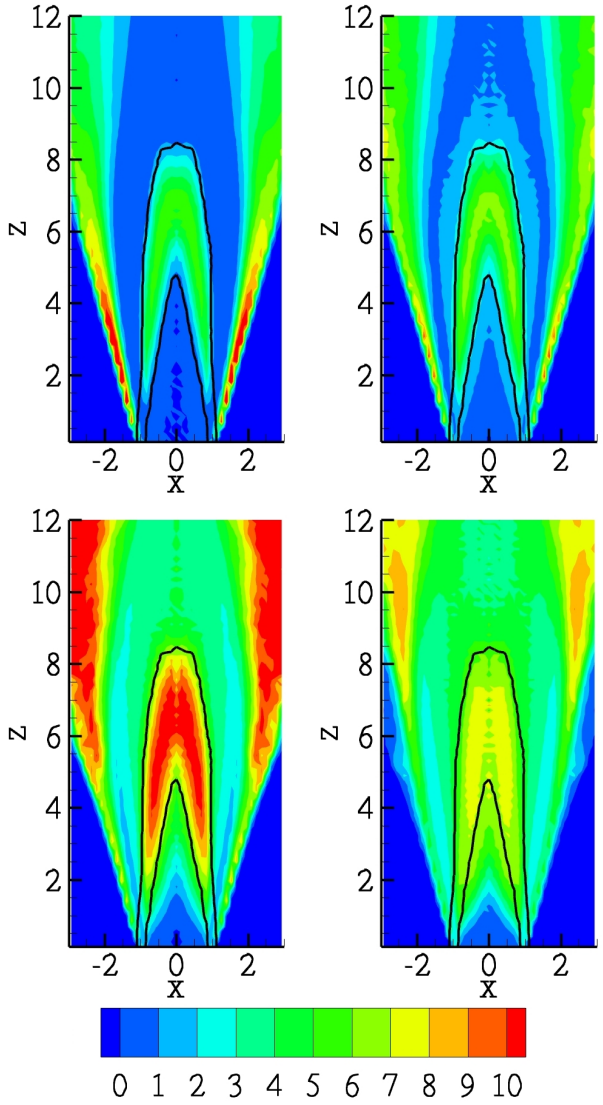

Figure 12.2 Clustering index contours K, eq. (12.5). Top-left $St_{fl} = 0.022$, top-right $St_{fl} = 0.54$, bottom-left $St_{fl} = 2.16$ and bottom-right $St_{fl} = 8.65$. The clustering index is evaluated on control volumes of characteristic size $\ell = 0.125\, R$. The solid lines ($Y_R/Y_R^0 = 0.05$ and $Y_R/Y_R^0 = 0.95$) delimit the flame brush.

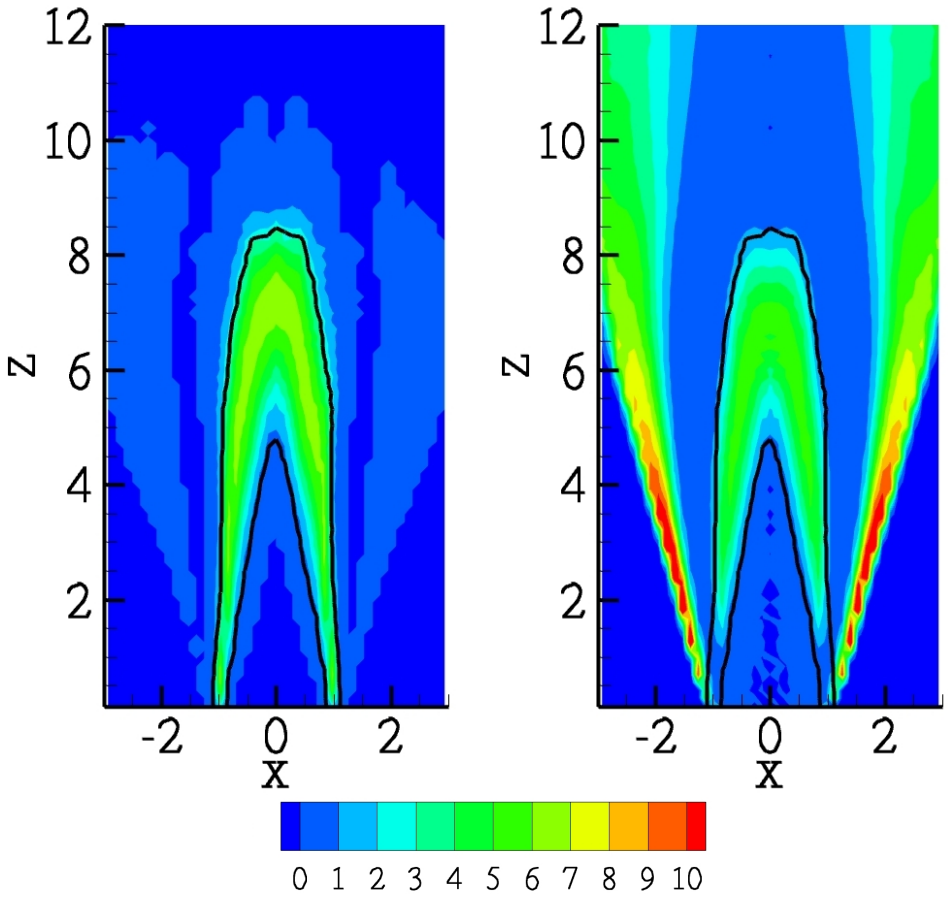

Figure 12.3 Clustering index K_0 for almost Lagrangian particles: the model (12.9) for tracers, left panel, is compared with the numerical results for particles at $St_{fl} = 0.022$, right panel. See caption of figure 12.2 for control volume dimensions and definition of the flame brush.

clustering index $K < 0$. On the contrary, if particles preferentially aggregate in clusters, the variance exceeds the mean value, yielding a positive clustering index, $K > 0$. Since the clustering index depends on the length scale ℓ, $K(\ell)$, via $\bar{n}(\ell)$ and $\overline{(\delta n)^2}(\ell)$, all the above features are scale dependent. Additionally for inhomogeneous processes the clustering index becomes a field since it depends on the position of the control domain $\Omega(\boldsymbol{x})$, $K = K(\boldsymbol{x}, \ell)$.

The clustering index field can be exploited to quantify the amount of particle segregation induced by a fluctuating turbulent flame front. The clustering index for each particle population is shown in figure 12.2.

The region spanned by the flame front is called the flame brush. It can be defined in terms of the average progress variable $\bar{c}$, where the instantaneous progress variable $c = 1 - Y_R/Y_R^0$ ranges from 0 in the reactants to 1 in the products. The flame brush is then the region where $0 < \bar{c} < 1$ the boundaries of which are shown as thick lines in figure 12.2. The clustering index K, shown by colors in the same figure, is positive in the flame brush and in the outer region of the jet. In the outer region, the increased value of K is indeed induced by the intermittency of the boundary between the hot jet seeded with particles and the external, particle-free, cold environment. From our present point of view the most significant feature is that even extremely small particles, $St_{fl} = 0.022$, which behave like tracers under every respects, show large values of K in the flame brush region. While clustering of finite mass particles is more or less expected, this behavior of tracer-like particles needs to be properly understood before the clustering properties of finite mass particles are addressed.

To try explaining this effect of the flame, we resort to the Bray-Moss-Libby (BML) description of the flamelet [106] where the field is decomposed in two nearby regions, pertaining to burned ($c = 1$) and unburned ($c = 0$) gases respectively, separated by the thin instantaneous front. Though not strictly necessary, for simplicity we further assume that the probability to find n particles in a domain of size ℓ conditioned to the burned and unburned state, $p(n|c = 0/1)$, is independent of position. We highlight that for vanishing flamelet Stokes number such conditional pdf's should approach a Poisson distribution with suitable mean value. This assumption, exact for tracers, is reasonably accurate also for sufficiently small particles ($St_{fl} \ll 1$).

As anticipated, in the flamelet context, the state of the mixture is either $c = 0$ (unburned) or $c = 1$ (burned), and the probability distribution for the state is bimodal, $p(\boldsymbol{x}, c) = [\alpha(\boldsymbol{x})\delta(c) + \beta(\boldsymbol{x})\delta(1 - c)]$, where α and β are the probability to find the unburned or burned gases at $\boldsymbol{x}$. By evaluating $\bar{c}$ from the above pdf it follows $\beta(\boldsymbol{x}) = 1 - \alpha(\boldsymbol{x}) = \bar{c}(\boldsymbol{x})$; see [9, 106]. Assuming that the scale ℓ is sufficiently smaller than the characteristic scale of variation of the average progress variable (the flame brush characteristic dimension) $b = 1/|\nabla\bar{c}|$, the joint probability distribution of the particle number in V, n, and of the instantaneous progress variable, c, is $p(\boldsymbol{x}; c, n) = p(\boldsymbol{x}, c)\, p(n|c)$, which on the basis of our assumption follows as

$$p(\boldsymbol{x}; c, n) = \{[1 - \bar{c}(\boldsymbol{x})]\, \delta(c) + \bar{c}(\boldsymbol{x})\delta(1 - c)\}\; p(n|c). \tag{12.6}$$

Starting from 12.6, the first and second order moments of the particle number pdf read,

$$\bar{n}(\boldsymbol{x}) = [1 - \bar{c}(\boldsymbol{x})]\overline{n_u} + \bar{c}(\boldsymbol{x})\overline{n_b} \tag{12.7}$$

$$\overline{n^2}(\boldsymbol{x}) = [1 - \bar{c}(\boldsymbol{x})]\overline{n_u^2} + \bar{c}(\boldsymbol{x})\overline{n_b^2} \tag{12.8}$$

where $\bar{n}_{u/b} = \langle n|c = 0/1\rangle$ is the mean particle number in the volume V corresponding to fully unburned/burned conditions and analogously $\overline{n^2}_{u/b} = \langle n^2|c = 0/1\rangle$.

For tracers, the average particle number ahead and behind the front are not independent since they are related to the respective fluid density. Hence, the ratio $\bar{n}_u/\bar{n}_b$ equals the gas

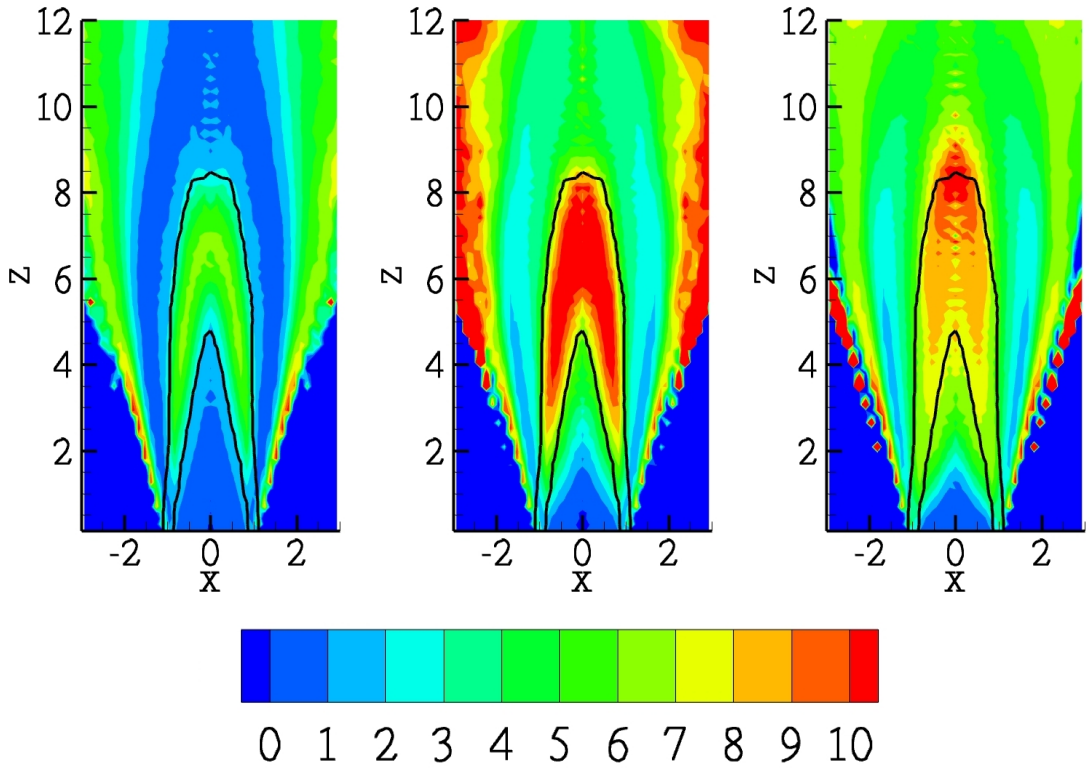

Figure 12.4 Clustering index field reconstructed from relation (12.12). From left to right, $St_{fl} = 0.54$, $St_{fl} = 2.16$ and $St_{fl} = 8.65$. See caption of figure 12.2 for control volume dimensions and definition of the flame brush.

density ratio across the thin flame front which is estimated by the expansion ratio $\tau = T_b/T_u$, $\bar{n}_u/\bar{n}_b = \tau$. Considering equations (12.5), (12.7) and (12.8), the clustering index reads,

$$K_0(\boldsymbol{x}, \ell) = \frac{\overline{n}_u(\ell)}{\tau} \frac{\bar{c}(\boldsymbol{x})[1 - \bar{c}(\boldsymbol{x})]\,(\tau - 1)^2}{\bar{c}(\boldsymbol{x}) + \tau[1 - \bar{c}(\boldsymbol{x})]}. \tag{12.9}$$

Hence, according to the flamelet model, the clustering index of purely Lagrangian tracers deviates from zero in the flame brush where $0 < \bar{c} < 1$, to vanish in the burned and unburned region where the statistics comes back to that of Poisson type.

Relation (12.9) highlights that for light particles, a positive clustering index, $K_0 > 0$, is mainly due to the fluctuation of the thin flame front which locally induces an intermittent state switching between unburned (higher particle concentration) and burned (lower concentration) conditions. The intermittency results in local density fluctuations which correspond to $K_0 > 0$. It is worth emphasizing that $K_0 > 0$ is here due to the alternation between two purely Poisson states, which show no clustering when taken separately. As we will see, this effect occurs also for inertial particles where the phenomenology is much more rich due to flame front fluctuations/corrugations interacting with the typical response time of the particle.

The bimodal description for the flame brush can be easily extended to model the intermittent region separating the burned gas and the external particle-free environment. To this purpose we shall assume that the instantaneous interface between hot gas and environment is sufficiently thin, as expected of high Reynolds number flows. Borrowing the notion from the classical description of cold jets, [107], we will refer to this thin interface as the instantaneous viscous super-layer and will call super-layer brush the region spanned by the fluctuating super-layer.

Across the instantaneous interface the average particle number jumps from $\bar{n}_b$ to $\bar{n}_e = 0$. After considering the limit $\tau_e = \bar{n}_b/\bar{n}_e \to \infty$, the empty external region is formally characterized by a limiting Poisson process with vanishing average particle number. According to the model the clustering index pertaining to the super-layer brush is described by relation (12.9) in the limit $\tau \to \infty$ with $\bar{n}_u$ replaced by $\bar{n}_b$, i.e. $K_0 = \bar{n_b}\bar{c}_e(\boldsymbol{x})$. In full analogy with the flame brush, the instantaneous indicator function $c_e(\boldsymbol{x})$ is a singular bi-modal distribution which takes the value 0 in the fully burned region and 1 in the external fluid. Its average $\bar{c}_e$ goes smoothly from zero to unity and its transition defines the super-layer brush. The very large value of K, seen in figure 12.2 in the outer part of the jet, can actually be interpreted in this framework, after noting that the relevant Stokes number should be defined in terms of the local time scale of the super-layer which is typically larger than the flamelet characteristic time.

Figure 12.3 concerns the comparison between the numerical results for the smallest, almost Lagrangian particles ($St_{fl} = 0.022$) and the model prediction (12.9). Despite the crudeness of the model, the agreement is excellent.

When the particle inertia is significant, the particle interaction with the flame introduces additional effects depending on St_{fl}; see figure 12.2. The clustering index for these inertial particles is in general larger than the tracers'. The peak clustering occurs within the flame brush, though a significant value is also found in the burned gas region. Indeed the maximum peak clustering intensity takes place for particles with $St_{fl} = 2.16$. The observation that peak clustering is achieved at flamelet Stokes numbers of order unity confirms that St_{fl} is the actual parameter controlling particle localization effects in turbulent premixed flames. Furthermore it shows that the increased localization is associated with the increased relaxation time of the particles.

The model for tracers, equation (12.9), can be extended to inertial particles by assuming that the fluctuating flame front separates two states, now both not belonging to a Poisson distribution and characterized by $\bar{n}_{u,b}$ and $\overline{\delta n^2_{u,b}}$ (hence $K_{u,b} = \overline{\delta n^2_{u,b}}/\bar{n}_{u,b} - 1$) for the unburned and burned mixtures, respectively. From the flamelet model, the same procedure used for equations (12.7) and (12.8) yields

$$\begin{aligned}
\overline{\delta n^2} &= (1-\bar{c})(\overline{n_u^2} - \overline{n_u}^2) + \bar{c}(\overline{n_b^2} - \overline{n_b}^2) - 2\bar{c}(1-\bar{c})\overline{n_u}\,\overline{n_b} \\
&= (1-\bar{c})\overline{\delta n^2}_u + \bar{c}\overline{\delta n^2}_b + \bar{c}(1-\bar{c})(\overline{n_u} - \overline{n_b})^2 \\
&= (1-\bar{c})\overline{n_u}K_u + \overline{cn_b}K_b + \bar{c}(1-\bar{c})(\overline{n_u} - \overline{n_b})^2 + \bar{n}\,.
\end{aligned}$$

Hence the clustering index becomes,

$$K = K_0 + \frac{K_u\tau + (K_b - K_u\tau)\bar{c}}{(1-\tau)\bar{c} + \tau} \tag{12.10}$$

where K_0 is the clustering index for tracers with a maximum in the flame brush, while the second contribution accounts for the effect in the flame brush of the clustering occurring in the pure states ($K_{u,b}$). In the range $0 \le \bar{c} \le 1$, the latter is a monotone function of $\bar{c}$.

The data we have available show that $(K - K_0)$ does exhibit a maximum inside the flame brush, suggesting that additional effects should be present beside the fluctuation between two pure non-Poisson states. To investigate these effects, it is convenient to assume the tracer behavior as the reference condition. By defining the deviation of mean and variance of particle

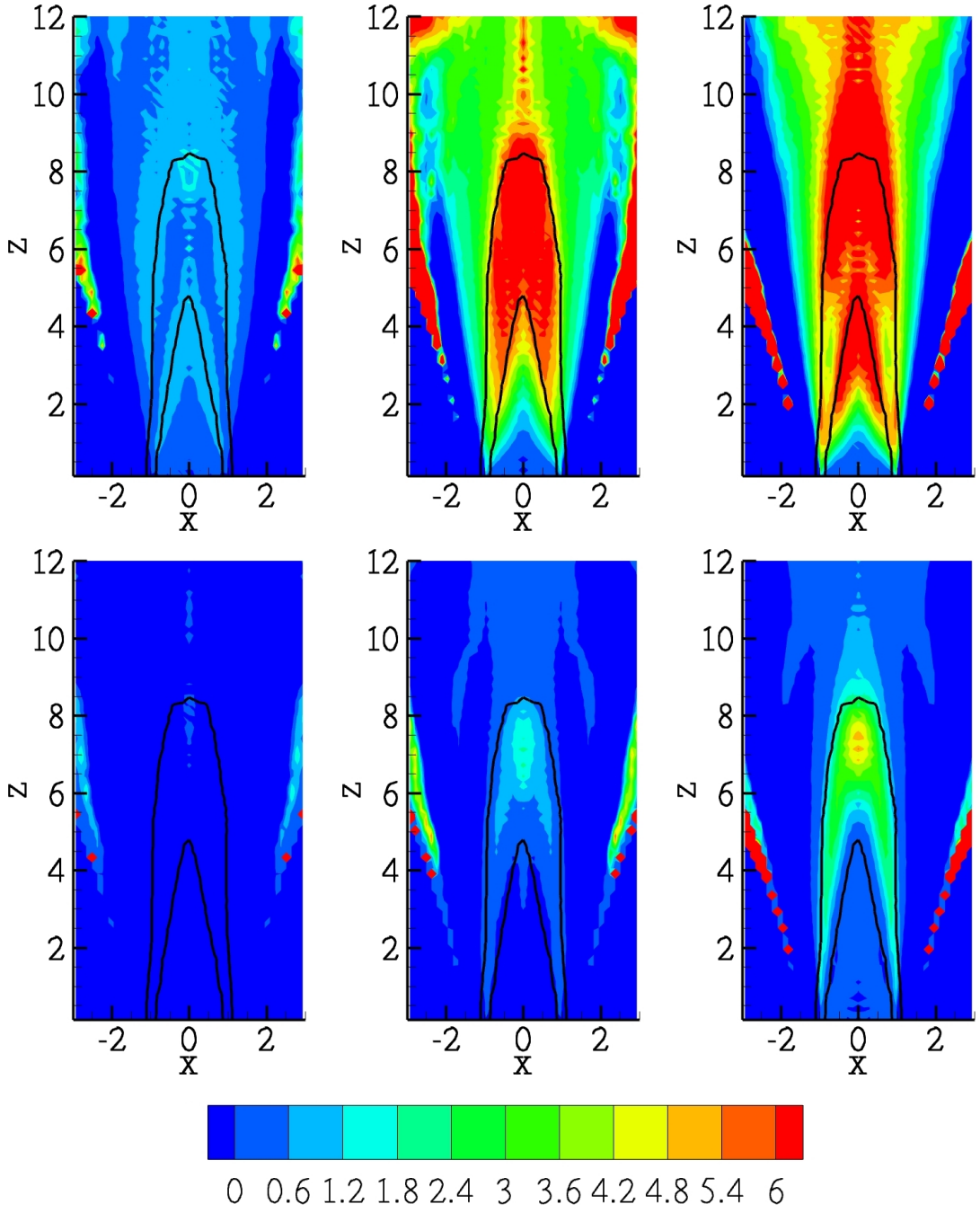

Figure 12.5 Contributions to the clustering index from the two last terms in right-hand-side of equation (12.12). Top line: $\Delta\overline{\delta n^2}/\bar{n}_0$. Bottom line: $(K_0+1)\Delta\bar{n}/\bar{n}_0$. From left to right, $St_{fl}=0.54$, $St_{fl}=2.16$ and $St_{fl}=8.65$. See caption of figure 12.2 for control volume dimensions and definition of the flame brush.

number from the local $\bar{c}$-dependent value pertaining to the tracers, $\bar{n}_0$ and $\overline{\delta n_0^2}$, respectively,

$$\begin{aligned} \bar{n} &= \bar{n}_0 + \Delta\bar{n} \\ \overline{\delta n^2} &= \overline{\delta n_0^2} + \Delta\overline{\delta n^2}\,, \end{aligned} \tag{12.11}$$

to first order in the corrections, the Clustering index $K(\ell)$ reads,

$$K(\ell) \simeq K_0 + \frac{\Delta\overline{\delta n^2}}{\bar{n}_0} - (K_0+1)\frac{\Delta\bar{n}}{\bar{n}_0}\,. \tag{12.12}$$

In this approximation, the effects of inertia are lumped in the last two terms in right-hand-side of equation (12.12). The first term, $\Delta\overline{\delta n^2}/\bar{n}_0$, takes care of the inertia-induced alteration of the variance of the particle number in the control volume. The second term, $-(K_0+1)\Delta\bar{n}/\bar{n}_0$, accounts for the variation of the mean particle number. The agreement between the approximate clustering index estimated by equation (12.12) and the exact one reported in figure 12.2 is excellent. Figure 12.5 reports $\Delta\overline{\delta n^2}/\bar{n}_0$ and $(K_0+1)\Delta\bar{n}/\bar{n}_0$ for particles with $St_{fl} = 0.54;\ 2.16;\ 8.65$. Concerning the particle most prone to segregation, $St_{fl} = 2.16$, $\Delta\overline{\delta n^2}/\bar{n}_0$ is large in the flame brush region, especially near the burned gas side. We infer that the interaction between the corrugated flame front and inertial particles is a source of particle clustering via the increase of the particle number fluctuation. The small positive value of $(K_0+1)\Delta\bar{n}/\bar{n}_0$ tends to slightly mitigate the increase of the clustering index which, for this kind of particles ($St_{fl} = 2.16$), is quite large. For particles with larger inertia, e.g. $St_{fl} = 8.65$, both corrections increase to a comparable value resulting in a less intense global clustering. Consistently, maximum clustering is actually achieved at intermediate Stokes number.

The data discussed so far show that a wrinkled, thin flame front has a more complex impact on the particle distributions than the simple alternation between two simple, non-Poissonian states. Specifically, the effect of inertia is to significantly enhance the fluctuation of the particle number found in a given (small) volume, $\Delta\overline{\delta n^2}$, leading to the increase of the clustering index over the value which pertains to purely Lagrangian tracers.

12.2.2 Experimental analysis

The results discussed in the context of DNS can be extended to actual experimental data. To this purpose an air/methane stoichiometric mixture, seeded with Alumina ($\rho_p \simeq 4000$ Kg/m^3) particles with diameter of $10\,\mu$m, has been injected into a Bunsen device with nozzle diameter $D = 18$ mm at Reynolds number $Re_D = 8000$. The characteristic time scale of the corresponding laminar flame front is of the order of $\tau_{fl} \simeq 0.16$ ms [95] leading to a flamelet Stokes number $St_{fl} = 4.4$.

Snapshots of the particle distributions are obtained adopting a commercial PIV system based on a 532 nm, 54 mJ Nd:YAG laser with a pulse-to-pulse delay of 70 μs. As usual, the laser beam goes through a cylindrical lens to generate a light sheet of thickness 0.45 mm. The camera is equipped with a 60 mm focal length lens and with a 1280×1024 pixel CCD corresponding to a field-of-view of 110.7 mm $\times$ 88.52 mm. More details on the experimental setup can be found in [95, 9].

The left panel of figure 12.6 shows the raw data corresponding to a Mie scattering image. An image analysis algorithm is used to extract the particle positions and to count the particle numbers in control volumes of dimension of $1.26 \times 1.26 \times 0.45\,mm$ ($0.14 \times 0.14 \times 0.05\,R$) centered

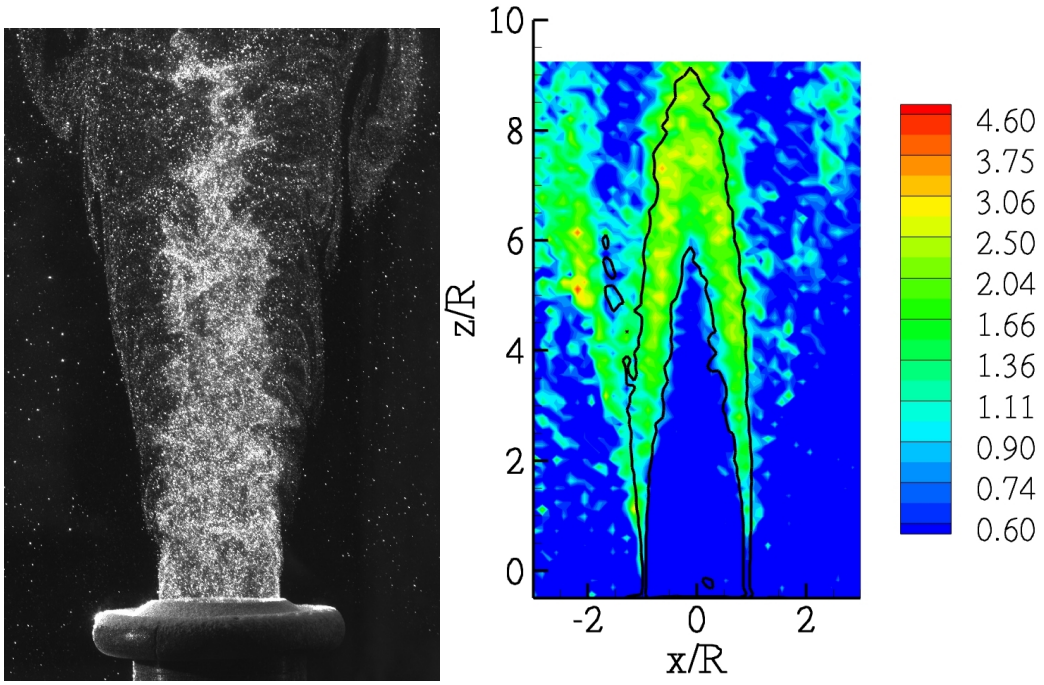

Figure 12.6 Experimental determination of the clustering index in a Bunsen turbulent stoichiometric methane flame at $Re_D = 8000$ endowed with Alumina particles of diameter $d_p = 10\mu m$, $St_{fl} = 4.4$. Mie scattering image, left panel, and clustering index, right panel. The solid lines demarcate the flame brush region.

at different positions within the field of view of the system. The box counting algorithm allows to determine the clustering index field K by evaluating for each box mean particle number and variance. The clustering index field is reported in the right panel of figure 12.6. An estimate of the flame brush is obtained by looking at the iso-levels of mean particle concentration. Its boundary is reported as thick black solid lines shown superimposed on the clustering index field. The typical particle density in the experiments is nearly half the value used in the DNS. The correspondence between numerics and experiments is qualitatively excellent; see figures 12.2 and 12.6, respectively. The quantitative discrepancy is fully explained by considering that the clustering index depends strongly on the local particle density through the average particle number in the control volume. This effect is particularly apparent in equation (12.9) for tracers. Accounting for the factor two in the particle density between numerics and experiments allows to conclude that, also in quantitative terms, the agreement is reasonable.

As a note, the significant clustering found in the numerical simulation in correspondence of the boundary between hot fluid and external environment (super-layer brush) does not show up in the experiment. The reason is that in the simulations we are computing an unbound jet with no particles in the external region. On the contrary, in the experiment, the Bunsen flame is placed inside a cylindrical vessel the lateral boundary of which is far enough from the jet axis to prevent the alteration of the flame dynamics. Nevertheless the particles get trapped in the vessel and sample the field also in the external part. As a consequence, no substantial particle density contrast occurs between the hot jet and its environment.

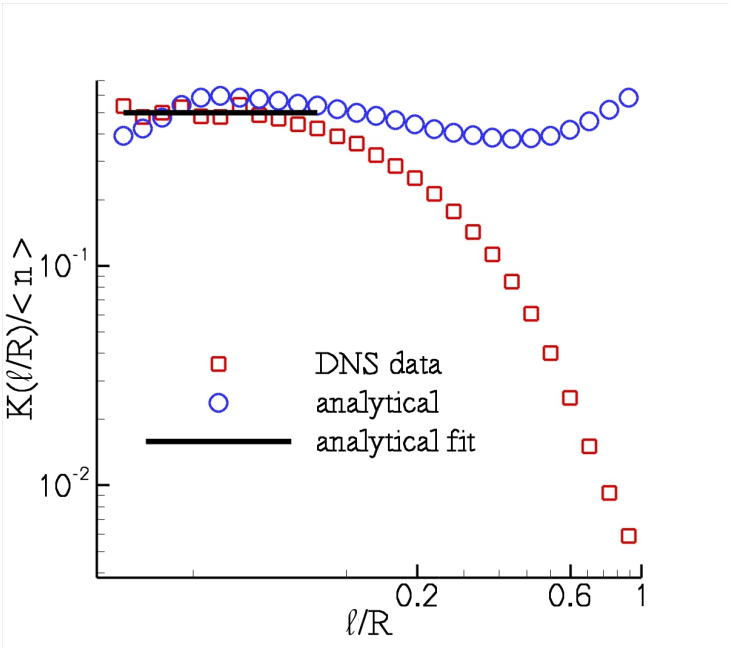

Figure 12.7 Normalized clustering index, $K(\ell)/\bar{n}(\ell)$, vs scale ℓ/R for quasi-Lagrangian particles, $St_{fl} = 0.022$, at axial station $z = 7R$. Red squares, DNS data; blue circles, estimate from equation (12.9); solid line, fit of data from equation (12.9).

12.3 The radial distribution function

An alternate description of the clustering index as a deviation from the reference Poisson distribution, is the radial distribution function $g(\ell)$; see [49, 68]. It provides the probability to find a couple of particles with distance in the interval $[\ell, \ell + d\ell]$ normalized with the probability that would result from a purely random spatially independent arrangement of particles. In presence of small scale clustering, the probability to have a second particle in the vicinity of a previous unity is much larger than expected on the basis of the random distribution, hence the increase above one of $g(\ell)$ at the given scale. Classically, the radial distribution function is introduced [49, 108] in the context of homogeneous flows as

$$g(\ell) = \frac{1}{4\pi\ell^2} \frac{d\mathcal{N}(l)}{d\ell} \frac{V^T}{\mathcal{N}^T}, \tag{12.13}$$

where $\mathcal{N}^T = 0.5N(N-1)$ is the total number of particle pairs in the system of volume V^T and $\mathcal{N}(\ell)$ is the number of pairs in the system with distance less or equal to ℓ. As shown in Appendix A in full detail, this definition can be generalized to inhomogeneous flows as

$$g(\boldsymbol{x}, \ell) = \frac{d\langle n_c(\boldsymbol{x}, \ell)\rangle}{d\ell} \frac{d\ell}{d\langle n_c(\boldsymbol{x}, \ell)\rangle_0}, \tag{12.14}$$

where $\langle n_c(\boldsymbol{x}, \ell)\rangle$, eq. (A.25), is the number of pairs found on average in a ball of radius ℓ centered at $\boldsymbol{x}$ and $\langle n_c(\boldsymbol{x}, \ell)\rangle_0$ is the corresponding number of pairs for a distribution with the same particle density and vanishing pair correlation; see Appendix.

It is well known [49] that for homogeneous turbulent flows $g(\ell)$ displays a scaling law at small separation, $g(\ell) \sim \ell^{-\zeta}$. The scaling exponent ζ is known to be a function of the Stokes number and quantifies the intensity of small scale clustering. All these considerations extend to the present case where the radial distribution function depends on position.

There is a direct connection between radial distribution function and clustering index. In homogeneous flows given the pair correlation function $\eta(\ell) = g(\ell) - 1$ one readily finds, see Appendix A,

$$K = \frac{4\pi\bar{n}}{V}\int_0^\ell \eta(\tilde{\ell})\tilde{\ell}^{\,2}d\tilde{\ell}. \tag{12.15}$$

where the control volume is taken as a ball of radius ℓ.

For tracers the flamelet model (12.9) predicts that $K_0/\bar{n}$ is independent of the scale ℓ, implying from (12.15)

$$g_0 = 1 + \frac{K_0(\ell)}{\bar{n}(\ell)}. \tag{12.16}$$

We expect that prediction (12.16) holds only at sufficiently small scales since the model relies on control volumes of scale ℓ much smaller than the flame brush thickness b.

Figure 12.7 shows $g_0 - 1 = K_0(\ell)/\bar{n}(\ell)$ vs ℓ/R for spheres centered on the axis of the jet at $z = 7R$. The squares are DNS data for almost Lagrangian particles with $St_{fl} = 0.022$. As apparent from the figure, $g_0 - 1$ is nearly constant at small scales as expected from equation (12.16). The circles are the estimate obtained from relation (12.9)

$$g_0 - 1 = \frac{K_0}{\bar{n}} = \frac{1}{\tau}\frac{\bar{c}(\boldsymbol{x})[1-\bar{c}(\boldsymbol{x})]\,(\tau-1)^2}{(\bar{c}(\boldsymbol{x}) + \tau[1-\bar{c}(\boldsymbol{x})])^2}\,, \tag{12.17}$$

where $\bar{c}$ is taken from the DNS. The behavior at large scale, where the inhomogeneity of the flow is dominant, is irrelevant to our purposes. The small departure from the constant value at small scale evidenced by the fit ($0.02R < \ell < 0.07R$, solid line) is related to numerical inaccuracies in the interpolation of $\bar{c}$ from the cylindrical grid to the small spheres centered on the axis of the jet. Nonetheless, as apparent from the figure, the agreement is quite reasonable in the range of scales where we expect the theory to work properly. We stress that the kind of behavior just described is limited to purely Lagrangian tracers. For inertial particles instead we should expect $g(\ell) \propto \ell^{-\zeta}$, hence $K(\ell) \propto \ell^{3-\zeta}$.

The radial distribution function $g(\boldsymbol{x}, \ell)$ at three different axial positions along the jet axis is presented in fig. 12.8 for four particle populations. The three positions are selected to check the particle system in the reactants $z = 3R$, in the flame brush $z = 7R$ and in the product region $z = 12R$, respectively. The three positions are best visualized in figure 12.2 where the thick lines denote the boundary of the flame brush. The generalized definition of radial distribution function complies with the requirement that it should approach unity for large ℓ/R. In the reactants (top panel of figure 12.8, $z = 3R$) $g(\ell/R)$ slightly exceeds unity at small scales $\ell/R \ll 1$. The slope of the logarithmic plot increases with the Stokes number. At this station, in the reactant region, the behavior is entirely consistent with the picture of particle clustering in cold flows [49, 68].

The middle panel of figure 12.8 more or less corresponds to a position well inside the flame brush, $z = 7R$. Noteworthy $g(\boldsymbol{x}, \ell/R)$ gives evidence of substantial intermittency for all the particle populations, as also for the lightest ones $St_{fl} = 0.022 - 0.54$. At small scales, the g value considerably exceeds unity, with a significantly increased slope. As for the clustering index, the basic effect already occurs for tracers (compare e.g. the open squares in the reactants and in the flame brush, top and middle panel of figure 12.8, respectively), it is enhanced by inertia and peaks for order unity flamelet Stokes number. In fact, the radial distribution function confirms that particles with $St_{fl} = 2.16$ present maximum clustering consistently with the conclusion based on the analysis of K, seen in figure 12.2.

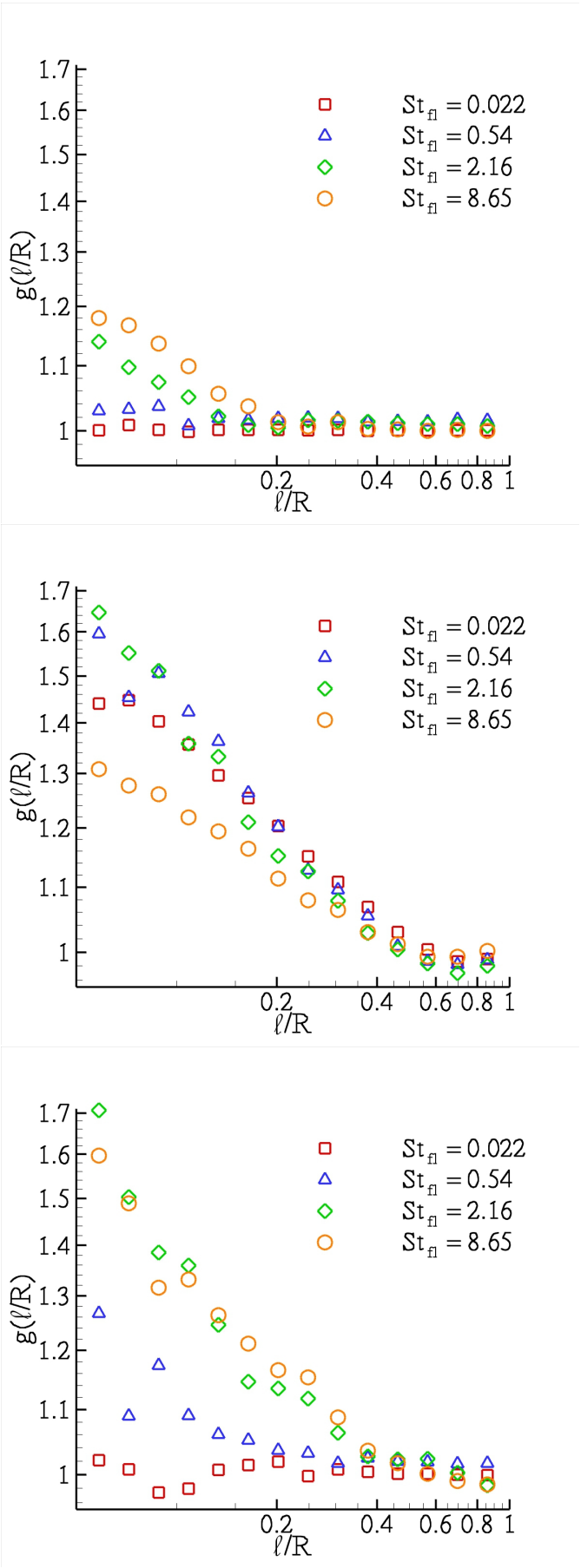

Figure 12.8 Radial Distribution Function $g(\ell/R)$ for the different particles populations at different axial stations. From top to bottom: $z = 3R$, $z = 7R$ and $z = 12R$.

St_{fl}	0.022	0.54	2.16	8.65
St^u_η	0.01	0.25	1.	4.
St^b_η	0.00125	0.03125	0.125	0.5

Table 12.1 Different possible definitions of the Stokes number for the four particle populations. From top to bottom: flamelet Stokes number, eq. (12.3) and Kolmogorov Stokes number, eq. (12.1), based on unburned and burned conditions, respectively. The relevant Kolmogorov time scale is evaluated for conditions on the jet axis in the fully unburned and burned regions, respectively.

Based on the radial distribution function, further downstream, at $z = 12R$ the lightest particles recover a more regular spatial arrangement. The visual inspection of the instantaneous configurations in figure 12.1 confirms this trend showing a reduced occurrence of particle clusters. The radial distribution function of the heaviest particles instead still shows intense clustering effects, see the instantaneous field of figure 12.1 with intense aggregates separated by definite voids.

We conclude that combustion has a strong influence on particle cluster formation also for tiny particles. The effect of inertia is significant and, as understood by the fact that peak clustering takes place at order one flamelet Stokes number, it is related to the typical time scale of the flame front which is considerably shorter than the turbulent time scale.

12.4 Remarks and discussion

The turbulent fluctuations of thin flame fronts, like those occurring in turbulent premixed flames, have been here shown to strongly affect the instantaneous spatial distribution of the particles, inducing intermittent effects which cannot be predicted in terms of mean fields. Specifically, data of a direct numerical simulation of a Bunsen premixed flame endowed with a particulate phase exhibit strong particle clustering in the region spanned by the instantaneous flame (flame brush). With respect to standard localization effects in cold flows [49, 65, 64], a peculiarity of this system is that even Lagrangian tracers which are purely advected by the flow manifest intermittent distributions which lead to an overall non-Poisson statistics in the flame brush. To isolate this effect from that of particle inertia, a simple model of the tracer behavior in turbulent premixed flames has been proposed to explain the observations. The model shows that the fluctuations of the instantaneous turbulent flame front induce the alternation between two states characterized by two different tracer densities which result in a positive clustering index. Inertia introduces additional effects which lead to large intensification of the clustering especially in the flame brush region. The relevant parameter controlling clustering is the flamelet Stokes number, ratio of the particle relaxation time and the characteristic time scale of the flame front.

Table 12.1 provides a comparison between the flamelet Stokes number of the particle populations we have addressed in comparison with the corresponding Stokes numbers based on the Kolmogorov time scale of the turbulence both in the fresh and in the burned gases. In reading the data one should be aware of the decrease of the Kolmogorov time scale associated with the change of density, viscosity and dissipation induced by the flame. In the fresh gases, the observed clustering is consistent with the classical picture [49, 109] for cold flows where Kolmogorov like turbulent fluctuations lead to small scale particle clustering for order unity St_η, where the Kolmogorov-Stokes number is based on the characteristic time associated with the

Kolmogorov scale. Due to temperature increase, St_η decreases substantially in the flame brush clearly indicating that the relevant time scale associated with the clustering process in that region is significantly shorter than the Kolmogorov time scale. Table 12.1 also shows that the appropriate time scale is here provided by the flame front characteristic time, leading to order unity flamelet Stokes number for the most segregating particles. The clear conclusion is that the effect is associated with the strong expansion of the flow across the flame. The phenomenology is however substantially more complex than expected on the basis of the behavior of tracers, as understood from the fact that the spatial variation of the net segregation cannot be described by the simple random alternation between two pure elementary states. We expect an interaction between the flame corrugations and the particles dynamics, a conjecture that we are presently unable to check with the data available to us which pertains to a single turbulent flame.

We are convinced that the phenomenology we describe is rather robust and, as an overall check, we have been able to produce experimental data taken from a premixed turbulent Bunsen flame seeded with $10\,\mu m$ diameter Alumina particles which confirm the numerical results. The present qualitative correspondence between numerics and experiments could be made quantitatively acceptable by considering the difference in average particle density between experiment and numerics. A more refined data analysis in terms of radial distribution function confirms the global picture and allows to account for the scale dependence of the clustering process.

To conclude, we have shown that flows with strong density gradients, like flames or shock waves, give rise to strong intermittent features in inertial particle distributions which are essentially different from the classical segregation phenomena found in cold turbulence interacting with inertial particles.

We stress that the present findings are expected to have a certain relevance for applications like PIV for turbulent flames [95] and combustion control through fuel/water droplets. Concerning PIV, cross-correlation algorithms for velocity measurements require the presence of a minimum number of particles in both of the interrogation windows considered during analysis of images. Particle voids with dimensions comparable to the window would drastically reduce the particle number, increase noise and uncertainty, and make the estimate of higher order moments, e.g. velocity rms, extremely difficult. In this respect, it should be noted that the operating conditions may be very usually close to the most critical situation.

Chapter 13

Effects of particle inertia on PIV measurements

Many fields of engineering are characterized by reacting flows where particles with different inertia and dimensions are transported. Dispersed particles are found, e.g., in solid-propellant rockets where metal powder is used to enhance the specific impulse or in reciprocating engines where soot may form due to combustion.

Small particles are also used to probe the flow velocity by measuring their displacements, e.g. Particle Image Velocimetry (PIV). In turbulent combustion, PIV is the leading technique to obtain the velocity field since other sensors hardly survive in chemically and thermodynamically harsh environments and present strong sensitivity to temperature variations [9, 110, 111].

In the experimental study of reacting flows, PIV combines non-intrusiveness (common to the other optical techniques), spatial resolution and the capability to obtain information concerning interactions between turbulent fluctuations and combustion. The understanding of particle dynamics in turbulent reactive flows is necessary to select a seeding able to adequately tag the velocity field, particularly because real particles, unlike perfectly Lagrangian tracers, do not follow exactly the flow trajectories. The inertia and finite dimensions of real particles induce different non-trivial phenomena such as small-scale clustering [49, 112, 68] or preferential accumulation (turbophoresis) [67, 113, 114, 115].

As well established, in turbulent flows the particle characteristic time–proportional to inertia–must be small compared to the Kolmogorov time scale in order to correctly capture the finest details of the flow. In turbulent combustion, the interaction between particles and thermal expansion adds, however, new phenomenologies. The limitations concerning the ability of particles to accurately follow the fluid become particularly severe for premixed flames, due to the abrupt heat release concentrated in a very thin region. To describe these implications, we limit here our discussion to premixed reacting flows in the *flamelet regime* [116], which is the most common condition for turbulent premixed flames. According to this classification, the reacting flow can be locally considered as a two-fluid flow where fresh reactants and burnt gases are separated by a thin interface–the flame front–where chemical reactions take place. This interface locally behaves more or less as a thin laminar flame, although the inner structure and the local flame speed may differ slightly from the pure laminar case due to the straining induced by turbulent fluctuations [117]. Since the reactions and the heat release occur in a thin region, the flame front induces abrupt fluid accelerations which particles can not easily accommodate due to their small but finite inertia.

The aim of the present chapter is to address the effects of the finite inertia and to provide a criterion for the appropriate selection of the PIV seeding in turbulent premixed flames with special emphasis on the region near the instantaneous flame front. As it will be shown, depending on the nature and thermodynamics conditions of the flame, the proposed criterion may easily lead to the selection of very small particles, if high accuracy is desired on all but the most simple observables. It often happens that such particles may be prone to strong thermophoretic effect [82]. In such cases optimal particle sizes should minimize the probing error formed by the combination of inertial and thermophoretic components. It is thus crucial to estimate beforehand the inertial inaccuracy in view of minimizing the global error; see [110, 111] for recent high accuracy measurements with sub-micrometric particles.

To evaluate inertial errors, the most straightforward approach would be the comparison between the actual fluid velocity and its estimate based on particle velocity. Since the fluid velocity is clearly experimentally unavailable, we are forced to exploit the direct numerical simulation (DNS) of a turbulent premixed Bunsen flame endowed with finite mass probing particles able to reproduce the main characteristics of actual PIV seedings.

The DNS data support a criterion based on a suitable *flamelet Stokes number* St_{fl}, defined in terms of the particle relaxation time and the characteristic time scale of the flame front, which, in the flamelet regime, is set by the expansion rate and is a thermochemical property of the mixture. Our conclusions are supported by PIV data acquired in conditions as close as possible to the numerical simulations. In addition, simple arguments provide a formula able to correct to leading order the estimated mean velocity, shown to work in a significant range of flamelet Stokes numbers.

Compared to mean flow quantities, much more stringent requirements are needed for the accurate reproduction of more complex statistical observables, such as turbulent fluxes, turbulence intensities, probability distribution function of velocity and velocity gradient within the flame front.

13.1 Theoretical considerations and implications for experiments

Before presenting our data, it is worthwhile discussing an a-priori estimate of the difference between particle and fluid velocity in the limit of small τ_p. In this limit the acceleration of particle and fluid closely match, $du/dt \simeq dv/dt$, see e.g. [49, 63]. Hence the Eulerian form of the equation (7.3) yields

$$u - v \simeq \tau_p \frac{Du}{Dt}. \tag{13.1}$$

In the reference frame of the flamelet the normal acceleration is

$$\frac{Du_n}{Dt} \simeq u_n \frac{du_n}{dx}, \tag{13.2}$$

where x is the coordinate normal to the front and u_n the normal velocity. The estimate for the acceleration follows:

$$\frac{Du_n}{Dt} \simeq S_L \frac{\Delta u_{fl}}{\delta_L} = S_L \frac{S_L \left(T_b/T_u - 1\right)}{\delta_L}. \tag{13.3}$$

From relations (13.1) and (13.3) the order of magnitude of the difference between fluid and particle normal velocity in the reaction region is given by:

$$|u_n - v_n| \simeq S_L \, St_{fl}. \tag{13.4}$$

13.1.1 Accuracy enhancement for mean velocity

The accuracy in the measured average fluid velocity may be enhanced by exploiting equation (7.3), rewritten as,

$$u = v + \tau_p \frac{Dv}{Dt} \tag{13.5}$$

where $Dv/Dt = \partial v/\partial t + v \cdot \nabla v$ is the Eulerian expression of the particle acceleration fields; see appendix B for a detailed derivation. Hence a more accurate estimate of the fluid velocity field can be obtained by taking into account the particle acceleration. In terms of mean fields the ensemble average of the equation (13.5) leads to

$$U = V + \tau_p \left[V \cdot \nabla V + \langle v' \cdot \nabla v' \rangle \right], \tag{13.6}$$

an equation that can be used in principle in its complete form (here $U = \langle u \rangle$ and $V = \langle v \rangle$ are the fluid and particle mean velocity, respectively, with angular brackets denoting average and a prime indicating fluctuating quantities). In many cases however the fluctuations provide a minor contribution which can be safely neglected, see § 13.2.5, yielding the simpler correction formula,

$$U \simeq V + \tau_p V \cdot \nabla V. \tag{13.7}$$

The equations discussed in the present subsection are in fact a first order correction to the standard assumption $U \simeq V$ which may be inappropriate when the Stokes number is not negligibly small.

The behavior of particles in a turbulent premixed reactive flow is addressed by means of an Eulerian DNS of a turbulent Bunsen flame coupled with a Lagrangian solver for particle evolution.

The DNS results are in good agreement with the experimental data for the same configuration and Reynolds number, figure 13.1; see [9, 8] for a detailed description of experimental set-up and technique. In the figure, axial and radial mean velocities are represented by the colored iso-levels with left and right part of the images providing experimental and numerical data, respectively.

Before collecting data for statistical analysis, the simulation was ran for $30\, D/U_0$ time units to guarantee the statistical steady state. One hundred complete fields, separated in time by $0.125\, D/U_0$, were gathered in the numerical data acquisition.

The particle configuration corresponding to the snapshot shown in the upper panel of figure 8.2 is shown in the upper panel of figure 13.2 where the effect of thermal expansion on particle density is apparent. A similar behavior is observed in the Mie-scattering experimental image reported in the bottom panel.

13.2 Results

13.2.1 Qualitative analysis

The effect of the variable-density flow on particles with different inertia is qualitatively shown in figure 13.3 where instantaneous configurations are presented. All particle populations exhibit a reduced concentration in the exhaust gas region due to the expansion experienced by the fluid across the flame front. This feature appears also in the experimental image of figure 13.2. Such abrupt change in particle density across the front is a matter of technical concern for PIV applications, since, also for negligible particle inertia, it may induce a bias towards the reactant velocity whenever the interrogation window spans the flame.

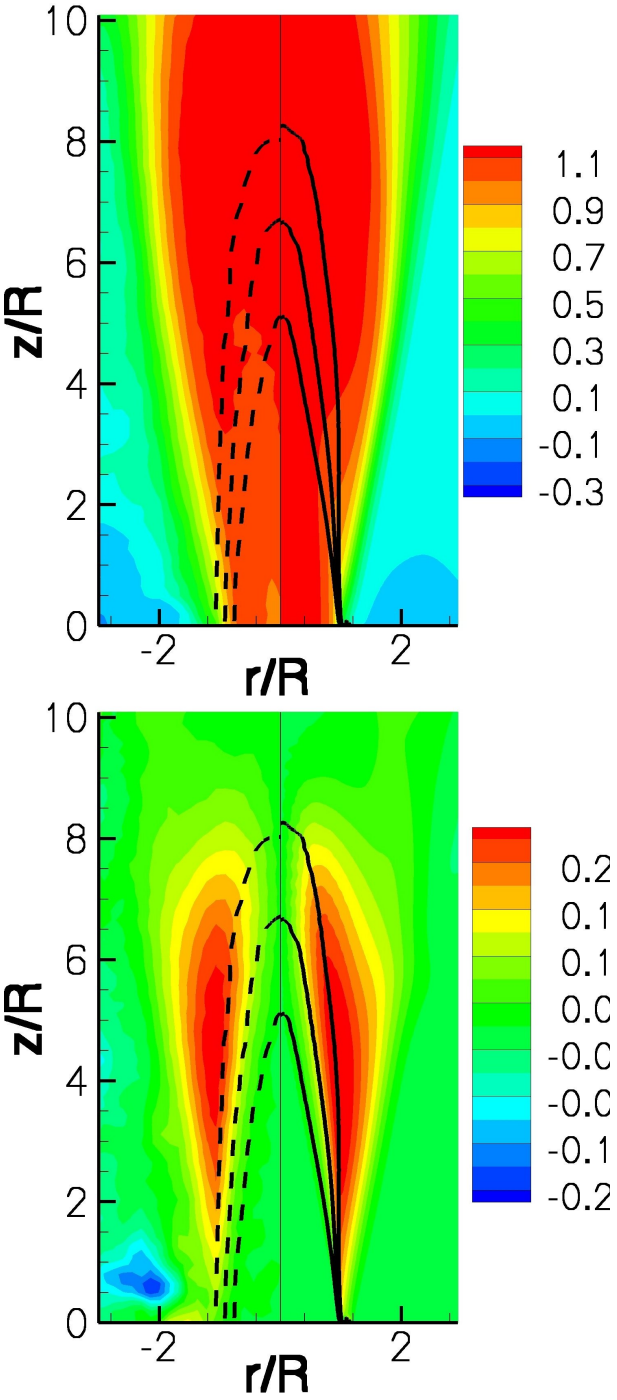

Figure 13.1 Comparison of mean velocity field between present DNS and experimental data obtained at same Reynolds number $Re_D = 6000$ and $S_L/U_0 = 0.05$. Experimental apparatus and techniques (PIV/OH-LIF) are described in Troiani et al. [8, 9]. The mean velocity field normalized by bulk velocity U_0 is represented by flood-contours, while three iso-levels of mean progress variable, namely $C = 0.1$, $C = 0.5$ and $C = 0.9$, are displayed with black lines. In each panel the left half-figure represents experimental data, while the right half-figure the DNS ones. Top panel: axial component; bottom panel: radial component.

At $St_{fl} = 0.022$ and 0.54 the normalized velocity difference $|v - u|/U_0$ shows that the fluid velocity is well reproduced by the particles; see figure 13.3. As the Stokes number increases a progressively increasing mismatch occurs especially beyond the front, after the abrupt acceleration due to heat release. In particular, heaviest particles are not able to follow the basic flow

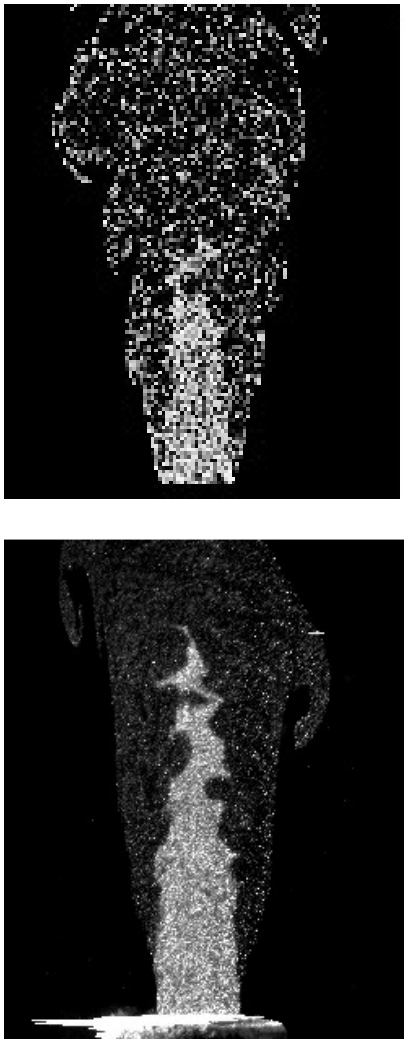

Figure 13.2 Top: slice (slice width $D/40$) of instantaneous particle configuration showing two populations at $St_{fl} = 0.022$ and $St_{fl} = 0.54$. Bottom: experimental raw Mie-scattering image of particles (PIV) [8] with Stokes and Reynolds numbers matching the numerical simulation.

features also when they are far away from the flame front.

Inertia also influences the spatial homogeneity of the instantaneous particle distribution. In all cases particle clusters and intertwined voids are appreciated on a range of smaller and smaller scales as the Stokes number is reduced, see e.g. [68] where the effect is discussed in the context of a homogeneous shear flow. This phenomenon is particularly apparent in the burned gas region, especially for intermediate inertia particles where the typical void dimension is large enough to be clearly seen in the plot. The heaviest particles tend to be more homogeneously distributed due to their inability to comply with the large-scale fluid motions.

Clustering may actually result in a source of noise in the cross-correlation analysis of particle positions, used in PIV to determine the velocity field. In this work, however, we address the accuracy of the velocity field estimate directly in terms of particle velocity. In addition the spatial segregation of probing particles may induce systematic statistical bias associated with preferential sampling of fluid velocity events. We may anticipate that this aspect, briefly addressed in the following, has negligible impact on low order statistical observables.

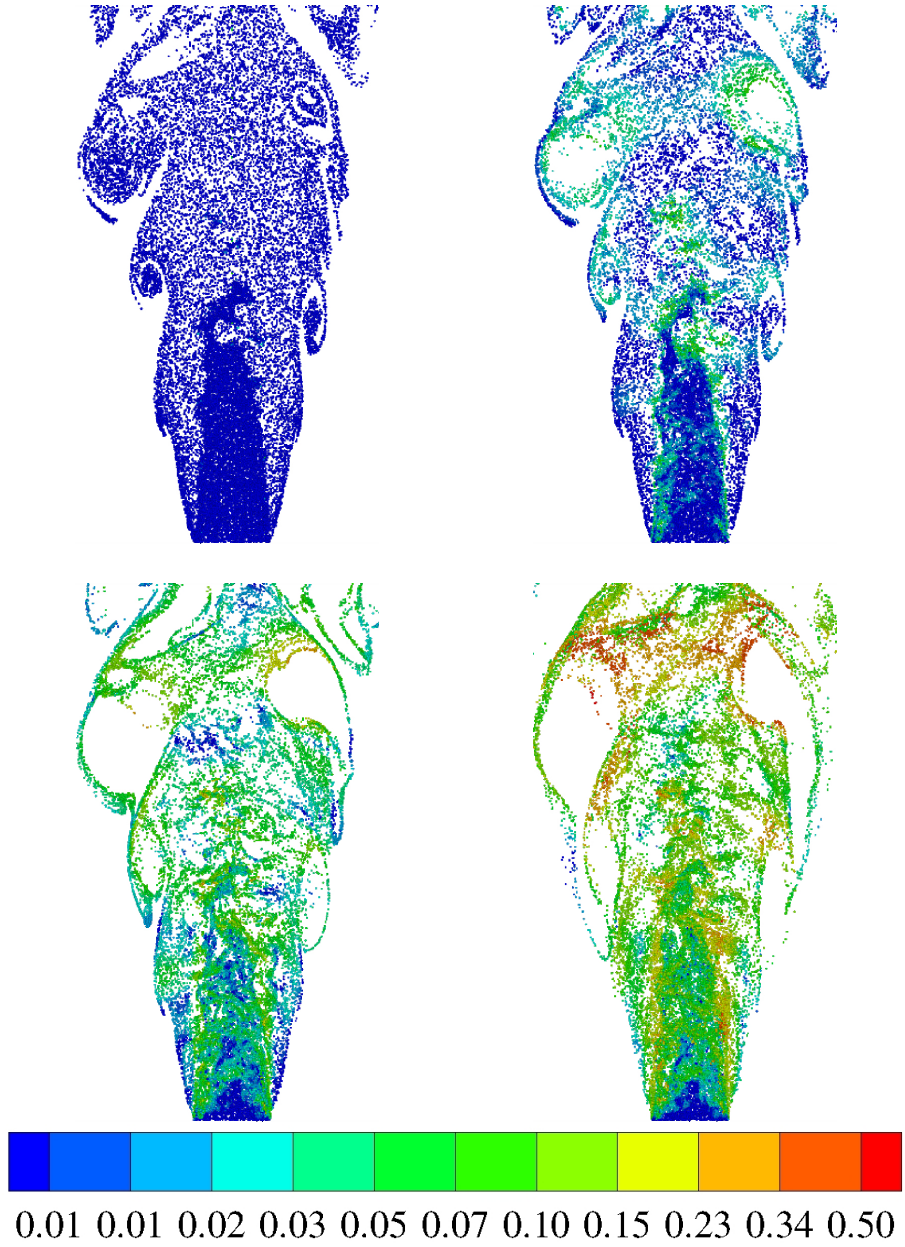

Figure 13.3 Thin slice of width $D/40$ in the axial-radial plane of the instantaneous particle configuration for different Stokes times. Top-left: $St_{fl} = 0.022$; Top-right: $St_{fl} = 0.54$; Bottom-left $St_{fl} = 2.16$; Bottom-right $St_{fl} = 8.65$. Colors denote the norm of the difference between particle and fluid velocity: $|v - u|/U_0$.

13.2.2 Mean velocity field

Figure 13.4 provides mean axial velocity profiles at two axial sections–$z = D$ and $z = 2D$–as a function of radial distance. Axial data are fairly well reproduced by the particles, at least when the Stokes number is not exceedingly large. The region of abrupt variation for the mean progress variable C–dashed line– is the so-called flame brush; see section 8. Here, the heaviest particles can not fully accommodate the steep velocity variations occurring across the front resulting in a slightly biased estimate of mean axial velocity.

A more critical situation concerns the mean radial velocity displayed in figure 13.5. Since the normal to the flame front is mainly aligned with the radial direction, thermal expansion promotes

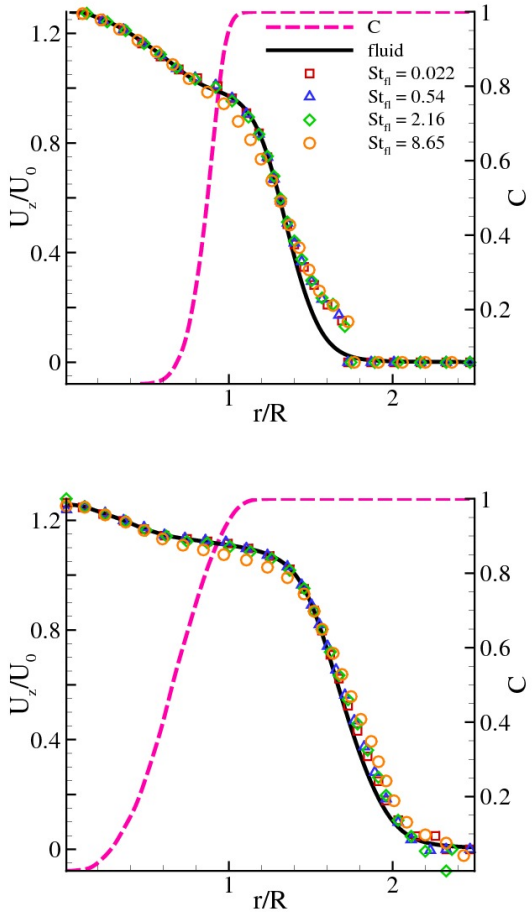

Figure 13.4 Profiles of normalized Reynolds-averaged axial velocity U_z/U_0 as a function of r/R; top panel, $z/D = 1$; bottom panel, $z/D = 2$. Black solid line: fluid velocity; Symbols: particle velocity at different Stokes numbers; dashed line (pink in the electronic version): mean progress variable C.

a sudden radial acceleration of the fluid. In these conditions appreciable errors emerge in the radial velocity estimation even for particles with flamelet Stokes number down to 2.16 (10 μm Alumina particles in a lean methane/air flame). Still considering lean air/methane flames, the accuracy is greatly enhanced reducing the size of the Alumina particles to five or one micron, as shown by the hollow squares and triangles in figure 13.5. As a generic feature, the shift in the peak position towards the burned gas systematically increases with the Stokes number. Shift and attenuation of the peak are clearly associated with the delayed response of the particles to the sudden acceleration through the front.

Since the surrounding environment is not seeded, a mismatch occurs between fluid and particle velocities in the outer part of the jet, where even the lightest particles manifest a substantial bias. This behavior is associated with the dynamics of the interface separating outer irrotational entrainment region and inner turbulent core, namely the highly intermittent viscous super-layer, see [118, 119] for incompressible cold jets. Here the super-layer is external to the flame and separates the burned turbulent gases and the outer irrotational surrounding air. Quasi-Lagrangian (small) particles, injected in the turbulent region, hardly cross the super-layer. As a consequence, the statistics sampled by very light particles is biased by being systematically associated with the fluid in the turbulent state. In other words, quasi-Lagrangian particles

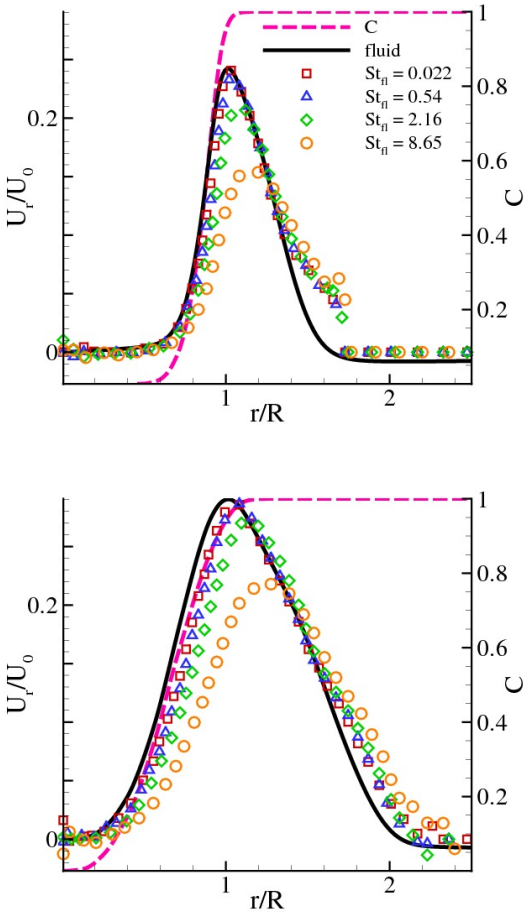

Figure 13.5 Profiles of normalized Reynolds-averaged radial velocity U_r/U_0 as a function of r/R; top panel, $z/D = 1$; bottom panel, $z/D = 2$. Legend as in figure 13.4.

always acquire the local fluid velocity, as shown in figure 13.6 by the uniform agreement of particle-conditioned fluid velocity and average particle velocity. Consistently, the persistent bias observed in figure 13.5 outside the flame brush should be ascribed to the non-uniform sampling of the outer part of the jet. On the contrary, the inner part, up to the entire flame brush region, is correctly sampled, as shown by the coincidence of the particle-conditioned with the unconditioned mean fluid velocity, figure 13.6. We conclude that the inertial errors in the mean radial velocity, figure 13.5, are not ascribed to sampling bias, as concerning the flame brush. Instead, the errors found in the outer part of the jet, outside the flame brush, are essentially associated to the non-uniform seeding of this highly intermittent region of the flow.

The magnitude of average fluid and particle velocity difference $\Delta U_r = \langle |u_r - v_r| \rangle$ is provided

Table 13.1 Maximum error $\Delta U_r|_{max}/U_0$ at $z = 1D$ and $z = 2D$ and its estimate, equation (13.4).

St_{fl}	0.022	0.54	2.16	8.65
Estimated	1.1×10^{-3}	2.7×10^{-2}	0.11	0.43
$z = 1\,D$	1.3×10^{-3}	2.3×10^{-2}	0.07	0.12
$z = 2\,D$	1.5×10^{-3}	2×10^{-2}	0.06	0.12

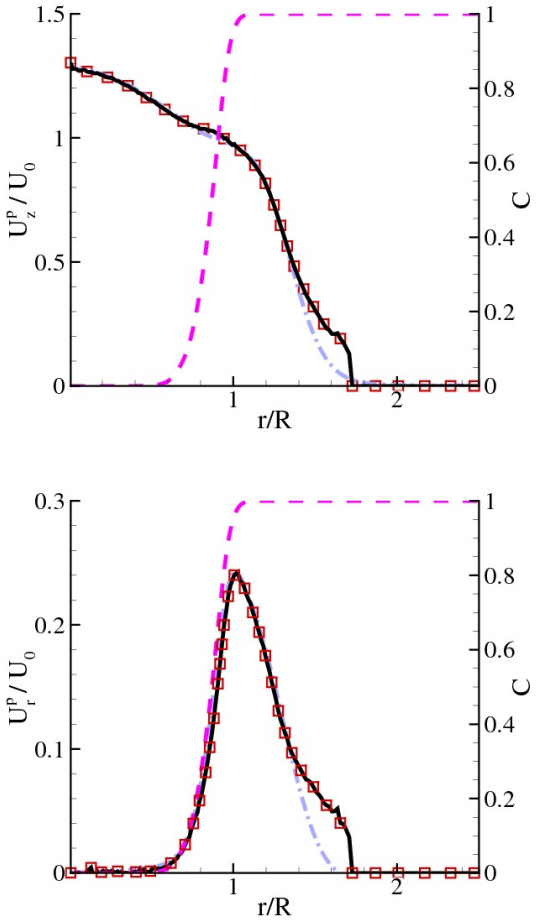

Figure 13.6 $St_{fl} = 0.022$, $z/D = 1$. Mean fluid velocity conditioned to the presence of particles, black solid lines. Unconditioned mean fluid velocity, gray dash-dotted lines. Mean progress variable C, dashed line (pink in the electronic version). Average particle velocity, symbols. Top panel: axial components; bottom panel: radial components.

in figure 13.7, which is focused on the radial, most critical component, mainly aligned with the normal to the flame front. The discrepancy increases monotonically with St_{fl} and it is mainly concentrated in the flame brush. Table 13.1 reports the maximum error $\Delta U_r|_{max}$ for each population in comparison with the order of magnitude estimate, (13.4), based on the small Stokes number approximation. The accuracy of the estimate is satisfactory up to $St_{fl} \leq 2.16$.

13.2.3 Second order statistics

Axial $\langle u_z'^2 \rangle / U_0^2$ and radial $\langle u_r'^2 \rangle / U_0^2$ normal stresses are presented in figure 13.8 and 13.9, respectively. The overall behavior of the fluid is properly reproduced only by the smaller particles, $St_{fl} = 0.022$ and $St_{fl} = 0.54$, although an outward shift and an attenuation of the Reynolds stress peak is still apparent in the radial-radial component, figure 13.9. Particles with $St_{fl} = 2.16$, still acceptably capture the axial normal stress, but fail to reproduce the radial-radial component altogether. The heaviest particles are unfit to provide realistic measurement for the stresses. Clearly, the sampling bias observed in the outer part of the jet (large r/R) for the mean velocity (figure 13.6) is significant also for second order statistics. These data unequivocally show that requirements for accurate reproduction of second order statistics are

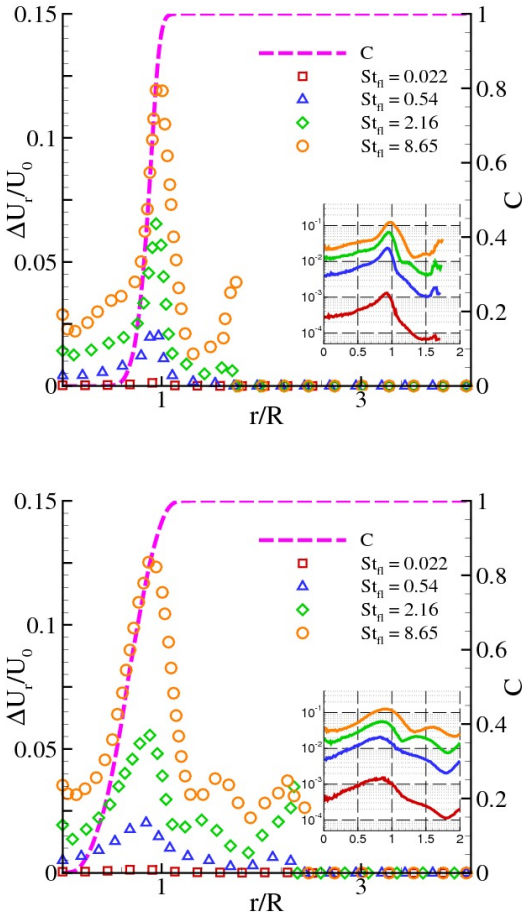

Figure 13.7 Profiles of the averaged absolute values of the differences between particle and fluid radial velocity normalized by bulk velocity: $\langle |u_r - v_r| \rangle / U_0$; top panel at $z/D = 1$, bottom one at $z/D = 2$. In the insets the same statistics is provided in semi-log form. Legend as in figure 13.4.

more stringent than for mean velocity, requiring a flamelet Stokes number St_{fl} order of 0.1.

13.2.4 Front-conditioned statistics

As discussed in the previous sections, we found that the bias emerging in the flame brush is mainly due to the thermal expansion at the flame front. More detailed information can be gathered by looking at front conditioned statistics. Their relevance can be appreciated by addressing the Bray-Moss-Libby (BML) formalism [120], where such statistical objects are used to determine the turbulent fluxes. In the BML context, the turbulent flux of the progress variable c is expressed as $\widetilde{u_i'' c''} = \tilde{c}(1-\tilde{c})(U_i^b - U_i^u)$, where $\tilde{}$ and $''$ denote Favre averaging and fluctuation, respectively. $U_i^b = \langle u_i | c = 1 \rangle$ and $U_i^u = \langle u_i | c = 0 \rangle$ are the mean velocity conditioned to products in the former case and to reactants in the latter. Clearly, turbulent fluxes are central objects in turbulent combustion and the BML model provides one of the few ways to extract them from combined PIV and OH-LIF experiments [9, 62].

The mean radial velocity conditioned to fresh gases U_r^u (numerically the nominal condition $c = 0$ is enforced by requiring $c \leq 0.05$), and conditioned to burned mixture U_r^b ($c \geq 0.95$), are displayed in figures 13.10 and 13.11, respectively. Analogously, we can define the front

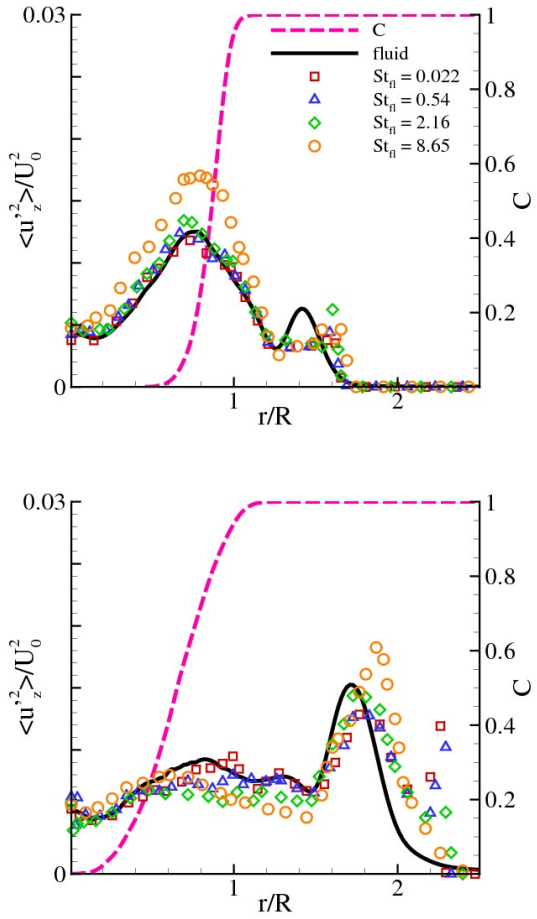

Figure 13.8 Profiles of normalized axial normal stresses $\langle u'^2_z \rangle / U_0^2$ as a function of r/R; top panel, $z/D = 1$; bottom panel, $z/D = 2$. Legend as in figure 13.4.

conditioned mean radial particle velocity V_r^b and V_r^u also reported in the same figures. The fluid unburned-conditioned statistics is reproduced by all particles with the exception of the most massive ones ($S_{fl} = 8.65$). The burned-conditioned velocity is instead much more demanding due to the sudden expansion across the thin flame front. Only the smaller particles, $St_{fl} = 0.022$ and $St_{fl} = 0.54$, provide high quality estimates. Particles with $St_{fl} = 2.16$ fail to reproduce the burned-conditioned radial velocity in the flame brush.

The biased response of the particles in the burned gas region has significant impact on the accuracy of the turbulent fluxes as estimated by the BML formalism, typically leading to an underestimation of the turbulent transport.

Figure 13.12, top panel, provides the pdf's of particle and fluid radial velocities within the flame front at $z = D$. The inner region of the front is here determined by the interval [0.05, 0.95] for the instantaneous progress variable c. Formally, the probability distributions are conditional pdf's $p(u_r|c \in [0.05, 0.95])$. On average the fluid velocity is directed away from the axis ($U_r > 0$), as expected. The process has a significant variance, comparable in magnitude with the mean value, and manifests a substantial intermittency, i.e. extreme events are much more frequent than expected on the basis of a Gaussian distribution with identical variance. It is immediately apparent that only the smallest particles are able to reproduce these rather subtle properties of the fluid pdf. The particles at $St_{fl} = 0.54$ are already unable the follow the right tail of the

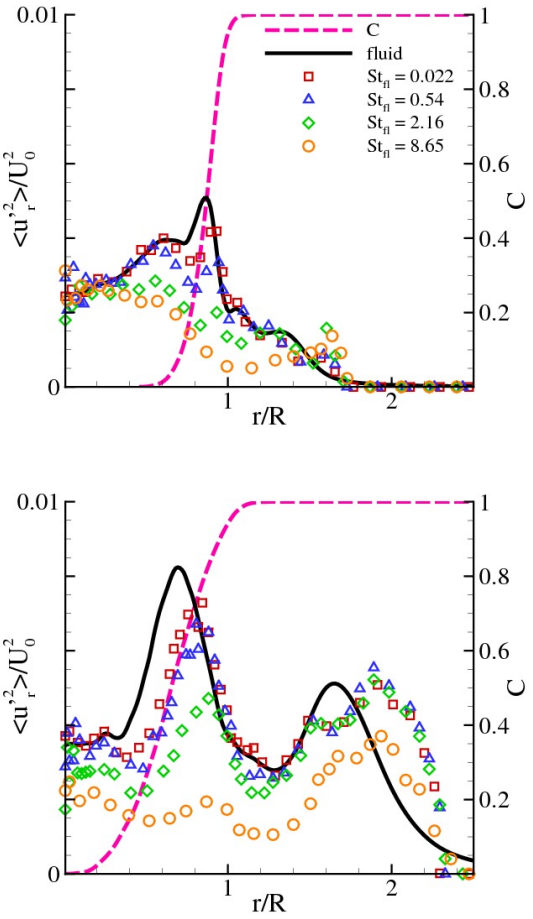

Figure 13.9 Profiles of normalized radial normal stresses $\langle u'^2_r \rangle / U_0^2$ as a function of r/R; top panel, $z/D = 1$; bottom panel, $z/D = 2$. Legend as in figure 13.4.

pdf, corresponding to events induced by the larger outwards accelerations. Increasing inertia, the modal value progressively decreases with a concurrent reduction of the process variance. At the same time, the pdf better approximates a Gaussian distribution.

Within the flame front, the radial-radial component of the fluid velocity gradient manifests a rather flat pdf, see bottom panel of figure 13.12. The figure shows that a significant deviation from the correct pdf is already observed for particles at $St_{fl} = 0.022$ with a significant bias already in the mean and modal value.

13.2.5 Improved estimate of the mean fluid velocity

Equation (13.7) supplies a first order correction to the mean fluid velocity estimate. Figure 13.13 provides a check of this formula by comparing the fluid mean radial velocity with both the mean particle velocity and the simplified form of the corrected expression

$$U_r \simeq V_r + \tau_p V_r \frac{\partial V_r}{\partial r}, \tag{13.8}$$

which retains only the dominating terms of equation (13.7).

As shown by figure 13.13, the corrected formula matches much more closely value and position of the fluid velocity peak for any particle population both at $z = D$ and $z = 2D$.

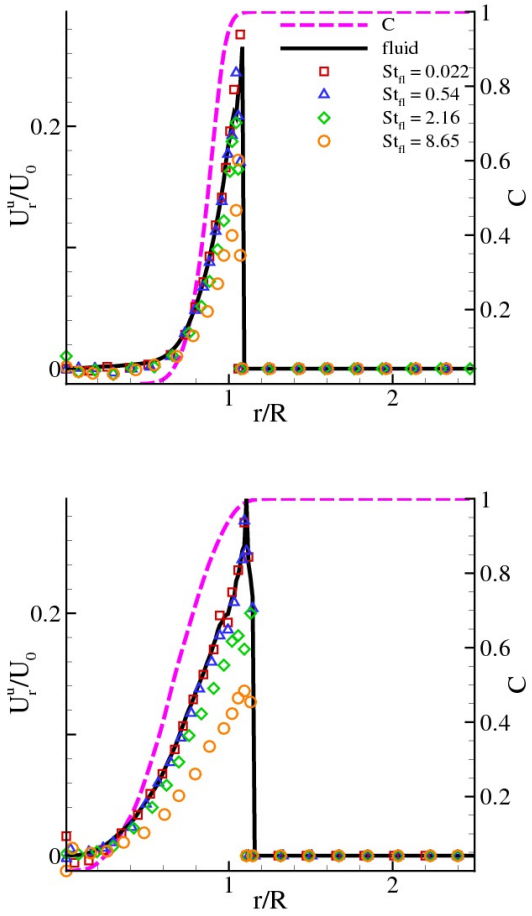

Figure 13.10 Profiles of mean radial velocity conditioned to unburned mixture U_r^u/U_0–$c \leq 0.05$. Black line: fluid velocity; Symbols: particles with different Stokes numbers; dashed line (pink in the electronic version): mean progress variable C. Top panel, $z/D = 1$; bottom panel, $z/D = 2$.

Figure 13.14 gives an overall impression on the accuracy enhancement achieved by applying the correction formula (13.8) to the raw data provided by the particles. The red curves (open symbols) in the top panel of the figure shows, for two axial locations, the error in the position of the radial mean velocity peak as difference (in absolute value) between the estimate based on the particles and the actual position taken from the DNS simulation. The blue curves (closed symbols) provide the difference between the actual position of the peak (DNS simulation) and its estimate based on the correction formula (13.8). The bottom panel of figure 13.14 analogously concerns the error in the intensity of the peak both for raw particle and enhanced data. The ability of the correction formula in estimating the peak position is very significant. The accuracy in the peak intensity also increases, still requiring however sufficiently light particles to achieve a confidence interval below five per cent.

13.3 Experimental validation

In order to analyze the effect of inertia on real particles, PIV measurements have been carried out in a Bunsen burner with three different particle populations varying the flamelet Stokes number. An air/methane stoichiometric mixture, seeded with the particles, has been injected

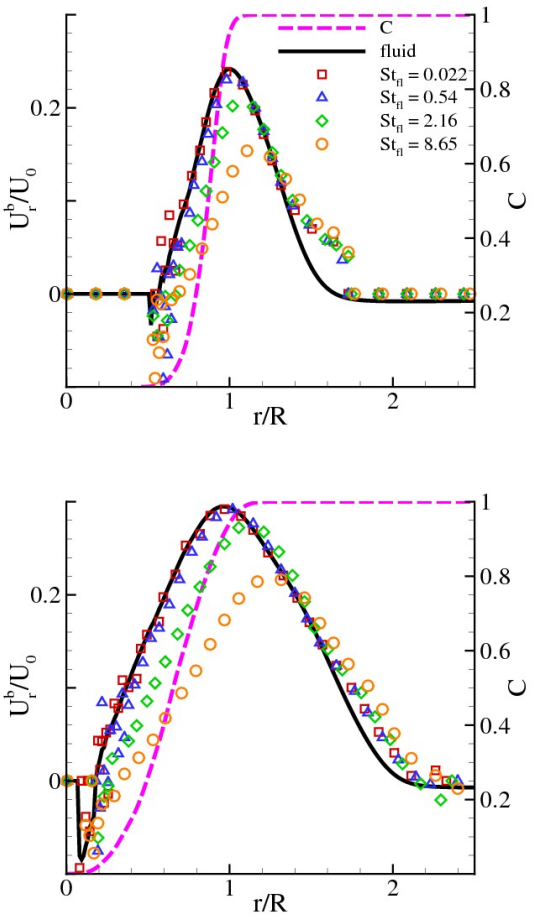

Figure 13.11 Profiles of mean radial velocity conditioned to the burned gases U_r^b/U_0–$c \geq 0.95$. Black line: fluid velocity; Symbols: particles with different Stokes numbers; dashed line (pink in the electronic version): mean progress variable C. Top panel, $z/D = 1$; bottom panel, $z/D = 2$.

into a Bunsen device at a Reynolds number of $Re_D = 8000$ (nozzle diameter of 18 mm). At stoichiometric conditions the characteristic time scale of the laminar front is of the order of $\tau_{fl} \simeq 0.16$ ms, as estimated by standard laminar flame computations [121]. Two populations consist of Alumina particles ($\rho_p \simeq 4000$ Kg/m^3) with nominal diameter $d_p = 5\,\mu$m and $d_p = 10\,\mu$m, leading to $St_{fl} = 1.1$ and $St_{fl} = 4.4$, respectively. The third kind of particles were very large glass spheroids ($\rho_p \simeq 2500$ Kg/m^3, $d_p = 50$ μm) with flamelet Stokes number $St_{fl} = 68.8$.

Concerning the PIV system already described in § 8, a thorough analysis of velocity measurement errors with Alumina particles of 5 μm, here considered as the reference measurement, is reported in [9]. To highlight the effect of the particle inertia, the same setup is used for all particles to keep the same level of optical accuracy (finite size of the interrogation windows).

The flame front induces an abrupt drop in the fluid density due to temperature increase. Moreover, a steep thermal gradient does not necessarily imply the local existence of an actually burning front and conditioning to the presence of radical species is necessary, as possible by the combined PIV/OH-LIF technique already illustrated in § 8. Nonetheless, in the present case, the thermo-chemical conditions and the jet-exit velocity of the flame have been selected to achieve a continuous flame front as expected on the basis of the standard Karlovitz criterion [8]. Under these conditions, the thermal gradient, or equivalently the density gradient, can be accepted as

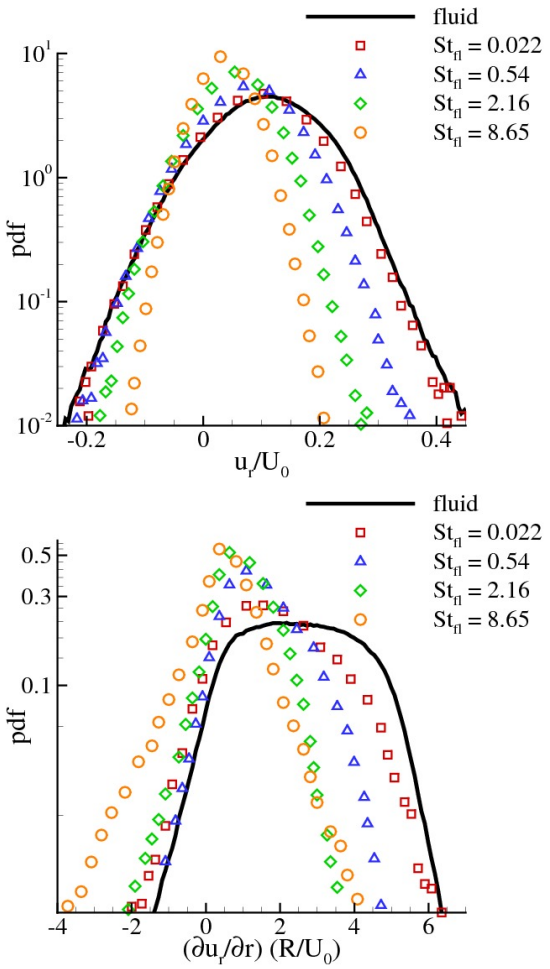

Figure 13.12 Statistics within the instantaneous flame front ($0.05 \leq c \leq 0.95$) at $z = D$. Top panel: pdf of particle and fluid radial velocity conditioned to $c \in [0.05, 0.95]$. Bottom panel: pdf of radial derivative of radial particle and fluid velocity, same conditioning.

a reasonable front-tracker.

Assuming the seeding particles able to follow the fluid motions almost exactly (vanishing τ_p), the change in fluid density induces a corresponding change in the particle density, as shown by equation (B.6) in the appendix, which implies $\nabla \cdot v = \nabla \cdot u + \mathcal{O}(\tau_p)$. This effect is apparent in figure 13.15, where moving from the right toward the left panel, i.e. reducing the particle relaxation time, the particle density contrast increases revealing finer details of the flame.

To quantitatively appreciate this effect, radial distributions of radial velocity have been examined, see figure 13.16 pertaining to $z/D = 2$. The thick dashed line (pink in the electronic version) provides the profile of the mean progress variable C. Open symbols refer to the mean radial particle velocity, showing for all three populations a velocity peak in the proximity of the average flame front. The particle inertia is reflected in the magnitude and position of the peak, which shifts toward the burned gases increasing St_{fl}. The comparison with the numerical results given in figure 13.13 confirms that the above mentioned effect is to be ascribed to the finite mass of the particles. Dash-dotted lines with closed symbols represent data corrected with equation (13.8). The improvement in the results is apparent, compare top panel of figure 13.16 and figure 13.13. As quantified by the correction, the mean velocity as estimated by 5 μm particles is only slightly affected by inertia. A stronger bias is present in the other two cases.

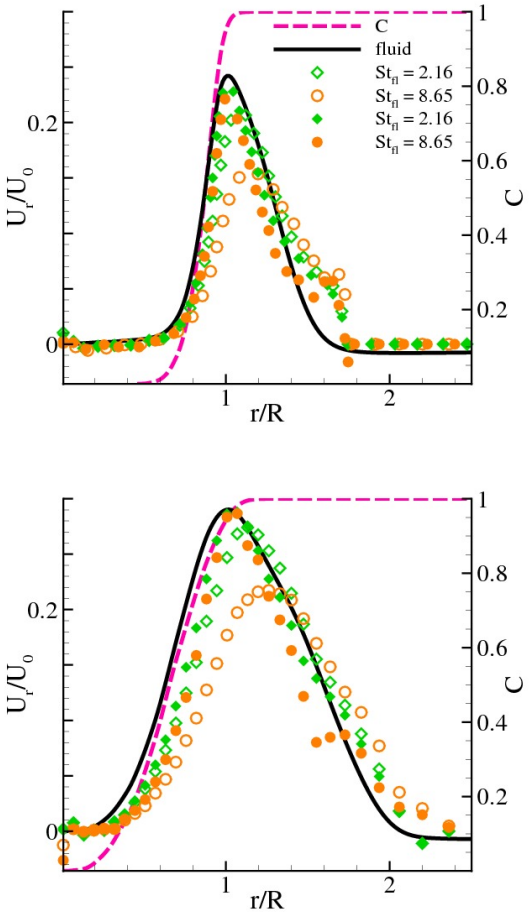

Figure 13.13 Radial profiles of normalized mean radial particle velocity (open symbols) and improvement based on equation (13.8) (filled symbols). Black line: fluid velocity; dashed line (pink in the electronic version): mean progress variable C. Top panel, $z/D = 1$; bottom panel, $z/D = 2$.

Although the correction formula succeeds in restoring the position of the peak as can be clearly observed in the bottom panel of figure 13.16, it still underestimates substantially the amplitudes. Clearly the data obtained with 50 μm particles are hardly representative of the flame behavior. Still equation 13.8 accurately estimates the peak position as can be seen in the bottom panel of figure 13.16.

13.4 Final Remarks

Beyond its fundamental interest, the dynamics of inertial particles in reacting flows is relevant for defining suitable criteria for PIV applications in turbulent premixed combustion. Typically optical velocimetry commonly uses small particles to track the fluid velocity under the assumption of negligible fluid/particle relative velocity. In fact, the finite inertia of the particle always promotes a relative velocity difference, provided the characteristic time scale of the flow is sufficiently small. Though this is not usually an issue in non-reactive turbulent flows, in premixed combustion significant errors may be induced by the fast dynamics across the instantaneous flame front. In this context, the most stringent condition is found to concern the *flamelet Stokes number*, ratio of particle relaxation to flame front time scale. This parameter specifically controls

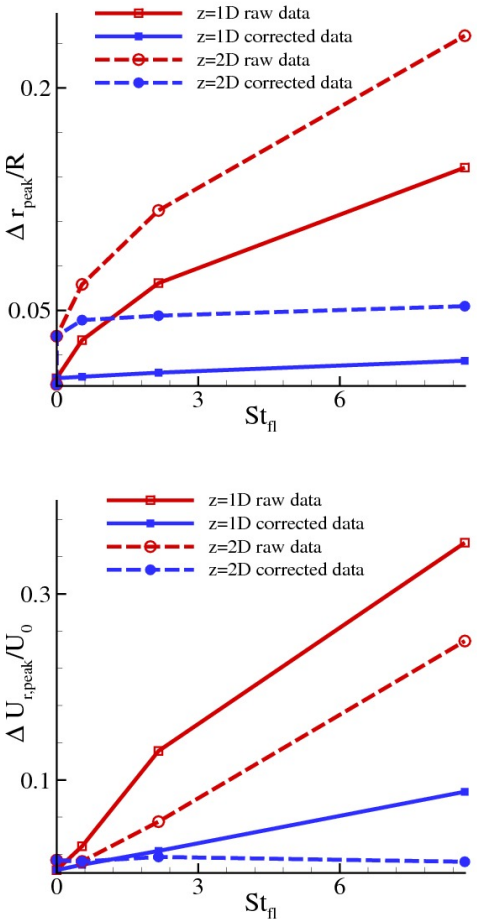

Figure 13.14 Top panel: normalized error in the radial peak position. Bottom panel: normalized error in peak value. Open symbols (red lines in the electronic version), raw data; Closed symbols (blue lines in the electronic version), data corrected via equation (13.8).

the particle response to the fluid velocity fluctuations caused by combustion.

As soon as the flamelet Stokes number is smaller than unity, no significant errors occur on the estimated mean flow velocities. This condition is implicitly satisfied by most of the published papers using standard seeding particles on the order of 1μm diameter for ordinary premixed flames (e.g. air/methane). The accuracy of the results obtained with slightly larger particles can be easily enhanced using the simple first order correction formula discussed in § 13.1.1.

However, turbulent combustion theory generally needs far more complex statistics. Typical examples are the turbulence intensities, the fluid velocity conditioned to the local state of the mixture, which enters, e.g., the expression of the turbulent fluxes according to the Bray-Moss-Libby formalism [120] and the probability distribution of fluid velocity and velocity gradients within the flame front. The present DNS results unequivocally show that the accurate estimate of these higher order statistics calls for a much lower limit on the admissible flamelet Stokes number, which may even be reduced of two orders of magnitude. Given the definition of the relevant parameter, the flamelet Stokes number $St_{fl} = \rho_p \, d_p^2/(18\,\mu)\,(S_L/\delta_L)\,(T_b/T_u - 1)$, chemical composition and thermochemical properties of the flame have a significant impact on the dimension of particles suited for accurate measurements, as direct consequence of the different flame speed, adiabatic flame temperature and front thickness.

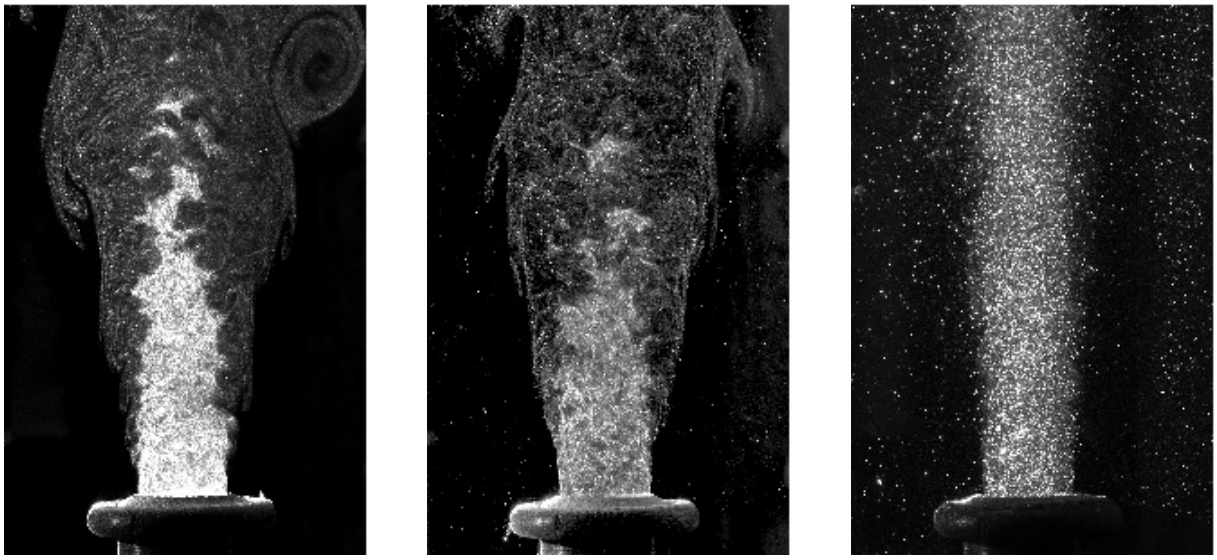

Figure 13.15 Mie scattering of seeding particles for increasing inertia: left, Alumina 5 μm; center, Alumina 10 μm; right, glass 50 μm.

As possible examples let us address a first case, where the mean velocity is the target of the measurement (design Stokes number $St_{fl} = 0.5$), and a second case targeting the much more demanding statistics within the flame front (design flamelet Stokes $St_{fl} = 0.01$). Considering a stoichiometric H_2/Air mixture at ambient conditions ($S_L \simeq 2.25\,\mathrm{m/s}$, $\delta_L \simeq 400\,\mu\mathrm{m}$, $T_b/T_u \simeq 7.5$, $\mu \simeq 4 \times 10^{-5}\mathrm{Kg/(ms)}$ [122]) the particle seeding diameter appropriate for mean velocity measurements is $d_p \simeq 1.5\,\mu\mathrm{m}$, which is reduced down to $d_p \simeq 0.2\,\mu\mathrm{m}$ if accurate information within the front is desired. Increasing the pressure to 2 MPa the flame speed and thickness change to $S_L \simeq 1.25\,m/s$, $\delta_L \simeq 10\,\mu\mathrm{m}$ [122], yielding $d_p \simeq 0.3\,\mu\mathrm{m}$ for the first and $d_p \simeq 0.05\,\mu\mathrm{m}$ for the second case.

We remark that accuracy requirements based only on the inertial lag, induces the selection of such small seeding particles that thermophoretic effect become substantial. In these conditions, the criterion here proposed could be used in principle to determine the largest particles compatible with the constraint on the inertial lag, at the same time minimizing the thermophoretic drift.

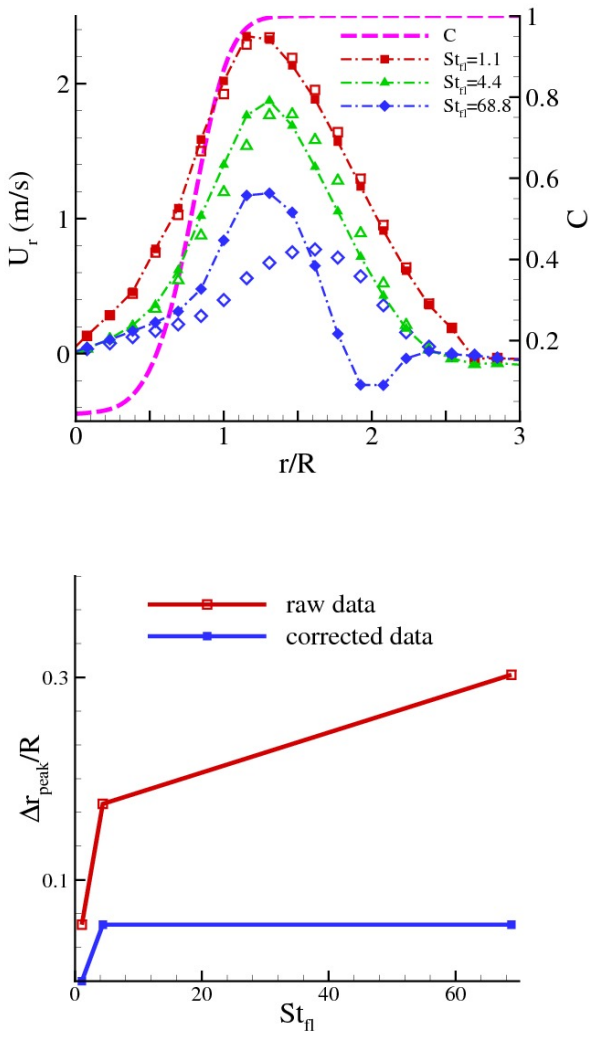

Figure 13.16 Top panel: radial profiles of mean radial velocity (m/s) of particles measured by PIV for different particles (open symbols) and those given by the correcting formula (13.8) (closed symbols). Dashed line (pink in the electronic version): mean progress variable C. Velocities have been measured at $z/D = 2$. Bottom panel: normalized error in the radial peak position at $z/D = 2$. Open symbols (red lines in the electronic version), raw data; closed symbols (blue lines in the electronic version), corrected data.

Chapter 14

Final Remarks and Future Perspectives

The purpose of the present work is to study turbulent jet flows which are widely employed in engineering applications and occur in many natural phenomena.

The scientific research, in the past, has been devoted to the study of the simple incompressible turbulent jet providing a lot of improvement in the understanding of this specific flow. On the other hand, in our opinion, more restricted attention has been reserved to complex jet configurations encountered both in engineering applications and in natural phenomena.

The aim of this work is then to stress two aspects of the some complex jets occurring in the engineering applications: the variable-density turbulent jet experiencing thermodynamic conditions near the critical one, and the turbulent reacting jet seeded with inertial particles.

The modern liquid rocket engines are characterized by injectors consisting in variable-density jet discharging in the combustion chamber where the pressure is high enough to reach and surpass the critical pressure of the injected fluids. These specific conditions have been demonstrated to strongly influence the mixing process [37, 123] and the subsequent combustion phenomenon [100, 124]. Both the classical variable-density jet and the variable-density coaxial jet are here investigated. In the former case, the existence of the self-similar behavior of the variable density jet is argued in the far field similar to that which occurs in the ideal incompressible jet [1]. In the latter case the classical configuration of the liquid rocket engine injectors is reproduced. The peculiar dynamics of ligaments formation is observed as previously evidenced in experimental studies and Direct Numerical Simulations of supercritical mixing layer [37, 39]. A qualitative observations of instantaneous field highlights the evolution of the ligaments in the shear layer between the inner and outer jet. The coaxial jet geometry influences the regular distribution of ligaments in the streamwise direction, while the angular distribution originates from the turbulent regularly spaces structures characteristics of the pipe turbulent flow and in general of the wall bounded flows, the so-called streaks [125].

The inertial particle dynamics in turbulent premixed flames is investigated in order to assess the effects of particle inertia on PIV measurements and to investigate the effects of turbulent fluctuating flame on particle spatial distribution. The issue is addressed both with direct numerical simulations and with PIV/OH-LIF experimental measurements. The numerical simulation reproduces a turbulent premixed flame mimicking a lean methane/air combustion reaction in the flamelet regime. The flow is seeded with inertial point particles with features similar to the Alumina particles used in PIV measurements. The physical conditions are such that the particle

dynamics can be assumed to be only influenced by the viscous drags. The present configuration is employed to address the effects of particle inertia on PIV (Particle Image Velocimetry) measurements and to study the influence of the particle inertia and turbulent flame front interaction on the particle spatial distribution.

Dealing with the PIV measurements, small particles are used as transducers of the fluid velocity, hence they have to be able to follow all fluid fluctuations. In the reacting flows the main fluid velocity fluctuations are induced by the combustion process in the flame front. The abrupt fluid velocity increase is followed by particles with a certain time lag depending on their inertia. The main parameter to describe the particle dynamics across the flame front is found to be the *flamelet Stokes number* St_{fl} in which the proper fluid time is defined through the flame thickness and the velocity jump across the flame. The effects of inertia on the fluid/particle velocity difference is addressed, showing that for small particles it is proportional to St_{fl}. In addition, for particles with $St_{fl} \simeq 1$, a correction depending on particle velocity gradient is introduced in order to reduce the fluid/particle velocity difference. In addition, the spatial distribution of particle in the flame brush region and in the burned gas zone is addressed. The cluster formation is stressed by means the clustering index [71] and the radial distribution function [49]. A peculiar behavior of the quasi-Lagrangian particles across the flame front is observed, in particular the flame front intermittent nature produces a positive clustering index denoting the presence of particle clustering also for these very tiny particles. When considering the inertial particles, the interaction between the corrugating flame front, the sudden expansion and the particle inertia produces the maximum clustering index for $St_{fl} \simeq 1$ in the flame brush region. All results are confirmed by experimental data provided by PIV/OH-LIF measurements of a laboratory Bunsen jet seeded with Alumina/glass particle of several size and at different flow conditions, i.e. Reynolds number and chemical features.

The results presented in this thesis are considered of great interest and usefulness for understanding how the thermodynamic conditions or the presence of a solid phase or chemical reaction influences the jet dynamics and the related phenomena. Despite progress, we believe that further investigations are necessary and additional topics are of interest for engineering applications and natural phenomena understanding.

In particular dealing with the real gas jets we expect that additional effects on mixing layer structures are introduced by different diffusion coefficient and molar mass pertaining to different fluid, e.g. hydrogen/oxygen as investigated in [39, 126]. To this purpose the numerical code will be improved by employing more accurate thermodynamic models for real gas jet and and physical coefficients. We consider very interesting and useful to develop model for sub grid terms deriving by LES equation filtering, which are expected to be as important as the thermodynamic pressure increase and reaches the critical state [44, 45, 46]. Another issue considered will be the direct numerical simulation of diffusive combustion process occurring in the shear layer between the inner and the outer jet in a coaxial geometry. The aim is to understand how the pressure and the inlet conditions influence the chemical reaction. To this purpose some challenging developing was necessary, first of all the transport properties, i.e. viscosity, diffusion or thermal conductivity, close to the critical point as a function of temperature and species mass fractions are not always available in literature, or in many case empirical or semi-empirical models are present. Moreover chemical kinetic models are necessary for the combustion at very high pressure; only in the last years several models for chemical reaction occurring in high pressure environment have been developed.

Considering inertial particles in turbulent premixed flames, in the future we will introduce in

the particle dynamic equation the thermophoresis force that for very small particles is proved to be as larger as the Stokes drag. In addition, it could be interesting to study particulate formation and evolution in a turbulent reacting flame; hence the introduction of a kinetic model to include the soot formation, through pyrolysis for example, will be necessary. On the other hand it is also considered interesting to study the droplet evolution in jet flow. Although the present code does not include a model for particle evaporation, are necessary only an equation for the particle radius evolution and an energy equation for the evaporation; in the literature several models are provided [28]. The first purpose will the investigation of the effects of turbulence and droplet distribution, concentration and size on the evaporation. In the following the evolution of droplets in reacting flow will be addressed. Two issues will be investigated: the effects of water droplet on the turbulent premixed flame and the evaporation mixing and reaction of fuel droplet. In particular, recent studies demonstrate that the introduction of the water droplet in the premixed flame inhibits high temperature fluctuations, hence inhibits the NO_x formation [127, 128]. A systematic investigation of the pollutant emission in relation to the droplet concentration and size will be conducted. Our purpose will be to study the effects of droplets size and distribution on combustion efficiency.

Part IV

Appendix

Appendix A

Considering N particles in a domain $\mathcal{D}$ with volume $V_{\mathcal{D}}$, the probability to find the particles in the configuration $\boldsymbol{x}_1, \ldots, \boldsymbol{x}_N$ is

$$p(\boldsymbol{x}_1, ..., \boldsymbol{x}_N; \omega) = \langle \delta[\boldsymbol{x}_1 - \hat{\boldsymbol{x}}_1(\omega)] ... \delta[\boldsymbol{x}_N - \hat{\boldsymbol{x}}_N(\omega)] \rangle \tag{A.1}$$

where ω is the stochastic variable belonging to a space $\mathcal{S}$ which determines the instantaneous configuration of the particles. The characteristic function of a certain domain, a sphere $\mathcal{B}_\ell$ of radius ℓ, say,

$$H(\boldsymbol{x}) = \begin{cases} 1 & \boldsymbol{x} \in \mathcal{B}_\ell \\ \\ 0 & \boldsymbol{x} \notin \mathcal{B}_\ell \end{cases} , \tag{A.2}$$

allows to count the instantaneous number of particles in the domain,

$$n(\mathcal{B}_\ell, \omega) = \sum_{p=1}^{N} H[\hat{\boldsymbol{x}}_p(\omega)] \ . \tag{A.3}$$

The r^{th} statistical momentum of the particle number in the domain is

$$\begin{aligned} \langle n^r \rangle &= \int_{\mathcal{S}} \left(\sum_{p=1}^{N} H[\hat{\boldsymbol{x}}_p(\omega)] \right)^r p(\omega) d\omega = \\ &= \int_{\mathcal{D}^N} \left(\sum_{p=1}^{N} H(\boldsymbol{x}_p) \right)^r p(\boldsymbol{x}_1, ..., \boldsymbol{x}_N) d\boldsymbol{x}_1 ... d\boldsymbol{x}_N \end{aligned} \tag{A.4}$$

where $\mathcal{D}^N = \overbrace{\mathcal{D} \times \ldots \times \mathcal{D}}^{N}$ is the N-fold Cartesian product of $\mathcal{D}$, which specifies the phase space of the particle system. From (A.4), the mean particle number in the sphere $\mathcal{B}_\ell$ is

$$\begin{aligned}\langle n\rangle &= \int_{\mathcal{D}^N}\left(\sum_{p=1}^{N} H(\boldsymbol{x}_p)\right) p(\boldsymbol{x}_1,...,\boldsymbol{x}_N)d\boldsymbol{x}_1...d\boldsymbol{x}_N = \\ &= N\int_{\mathcal{D}^N} H(\boldsymbol{x}_1)p(\boldsymbol{x}_1;...,\boldsymbol{x}_N)d\boldsymbol{x}_1...d\boldsymbol{x}_N = \\ &= N\int_{\mathcal{D}^N} H(\boldsymbol{x}_1)p(\boldsymbol{x}_1)d\boldsymbol{x}_1 = \\ &= N\int_{\mathcal{B}_\ell} p(\boldsymbol{x}_1)d\boldsymbol{x}_1\,,\end{aligned} \tag{A.5}$$

where the second line follows from the identity of all the particles. The second moment of the number of particles in $\mathcal{B}_\ell$ is

$$\begin{aligned}&\langle n^2\rangle = \\ &\int_{\mathcal{D}^N}\left[\sum_{p=1}^{N} H(\boldsymbol{x}_p)\right]\left[\sum_{q=1}^{N} H(\boldsymbol{x}_q)\right] p(\boldsymbol{x}_1,...,\boldsymbol{x}_N)d\boldsymbol{x}_1...d\boldsymbol{x}_N = \\ &= \sum_{p,q=1}^{N}\int_{\mathcal{D}^N} H(\boldsymbol{x}_p)H(\boldsymbol{x}_q)p(\boldsymbol{x}_1,...,\boldsymbol{x}_N)d\boldsymbol{x}_1...d\boldsymbol{x}_N = \\ &= N\int_{\mathcal{D}^N} H(\boldsymbol{x}_1)^2 p(\boldsymbol{x}_1;...,\boldsymbol{x}_N)d\boldsymbol{x}_1...d\boldsymbol{x}_N + \\ &+ N(N-1)\int_{\mathcal{D}^N} H(\boldsymbol{x}_1)H(\boldsymbol{x}_2)p(\boldsymbol{x}_1,\boldsymbol{x}_2;...,\boldsymbol{x}_N)d\boldsymbol{x}_1...d\boldsymbol{x}_N = \\ &= N\int_{\mathcal{B}_\ell} p(\boldsymbol{x}_1)d\boldsymbol{x}_1 + (N^2-N)\int_{\mathcal{B}_\ell\times\mathcal{B}_\ell} p(\boldsymbol{x}_1,\boldsymbol{x}_2)d\boldsymbol{x}_1 d\boldsymbol{x}_2\,.\end{aligned} \tag{A.6}$$

Since $p(\boldsymbol{x}_1,\boldsymbol{x}_2) = p(\boldsymbol{x}_1)p(\boldsymbol{x}_2)[1+\eta(\boldsymbol{x}_1,\boldsymbol{x}_2)]$, with $\eta(\boldsymbol{x}_1,\boldsymbol{x}_2)$ the pair correlation function, equation (A.6) reads,

$$\begin{aligned}&\langle n^2\rangle = N\int_{\mathcal{B}_\ell} p(\boldsymbol{x}_1)d\boldsymbol{x}_1 \\ &+ N^2\left[\int_{\mathcal{B}_\ell} p(\boldsymbol{x}_1)d\boldsymbol{x}_1\right]^2 - N\left[\int_{\mathcal{B}_\ell} p(\boldsymbol{x}_1)d\boldsymbol{x}_1\right]^2 + \\ &+ N^2\int_{\mathcal{B}_\ell\times\mathcal{B}_\ell} p(\boldsymbol{x}_1)p(\boldsymbol{x}_2)\eta(\boldsymbol{x}_1,\boldsymbol{x}_2)d\boldsymbol{x}_1 d\boldsymbol{x}_2 + \\ &- N\int_{\mathcal{B}_\ell\times\mathcal{B}_\ell} p(\boldsymbol{x}_1)p(\boldsymbol{x}_2)\eta(\boldsymbol{x}_1,\boldsymbol{x}_2)d\boldsymbol{x}_1 d\boldsymbol{x}_2 = \langle n\rangle + \langle n\rangle^2 \\ &- \frac{\langle n\rangle^2}{N} + N(N-1)\int_{\mathcal{B}_\ell\times\mathcal{B}_\ell} p(\boldsymbol{x}_1)p(\boldsymbol{x}_2)\eta(\boldsymbol{x}_1,\boldsymbol{x}_2)d\boldsymbol{x}_1 d\boldsymbol{x}_2\,.\end{aligned} \tag{A.7}$$

Considering the definition of Clustering Index, eq. (12.5), and expression (A.5), the change of variables $\boldsymbol{x}_1 = \boldsymbol{x}$ and $\boldsymbol{x}_2 = \boldsymbol{x} + \boldsymbol{\ell}$, yields:

$$K = -\frac{\langle n\rangle}{N} + \frac{N(N-1)}{\langle n\rangle}\int_{\mathcal{B}_\ell\times\mathcal{B}_\ell} p(\boldsymbol{x})p(\boldsymbol{x}+\boldsymbol{\ell})\eta(\boldsymbol{x},\boldsymbol{\ell})d\boldsymbol{x}d\boldsymbol{\ell}\ . \tag{A.8}$$

For homogeneous systems $p(\boldsymbol{x}) = p(\boldsymbol{x}+\boldsymbol{\ell}) = p_0$. Hence (A.8) reads,

$$\begin{aligned} K =& -\frac{\langle n\rangle}{N} + \frac{N(N-1)}{\langle n\rangle}\int_{\mathcal{B}_\ell\times\mathcal{B}_\ell} p_0^2\eta(\boldsymbol{\ell})d\boldsymbol{x}d\boldsymbol{\ell} = \\ =& -\frac{\langle n\rangle}{N} + \frac{N(N-1)}{\langle n\rangle}\left(\frac{\langle n\rangle}{NV_{\mathcal{B}_\ell}}\right)^2 V_{\mathcal{B}_\ell}\int_{\mathcal{B}_\ell}\eta(\boldsymbol{\ell})d\boldsymbol{\ell}\,, \end{aligned} \tag{A.9}$$

where we used (A.5) to express p_0. When the volume $V_{\mathcal{B}_\ell}$ of $\mathcal{B}_\ell$ is much smaller than $V_{\mathcal{D}}$, the average number of particles in $\mathcal{B}_\ell$ is much smaller than the total number of particles, $\langle n\rangle \ll N$ which is assumed to be a significantly large number, $N \gg 1$. Hence the relation between Clustering Index and pair correlation function $\eta(\boldsymbol{\ell})$ becomes,

$$K = \frac{\langle n\rangle}{V_{\mathcal{B}_\ell}}\int_{\mathcal{B}_\ell}\eta(\boldsymbol{\ell})d\boldsymbol{\ell}. \tag{A.10}$$

Under the same assumptions concerning the volume $V_{\mathcal{B}_\ell}$ and the total number of particles, the general expression (A.8) for the clustering index for non-homogeneous statistics reduces to

$$K = \frac{N^2}{\langle n\rangle}\int_{\mathcal{B}_\ell\times\mathcal{B}_\ell} p(\boldsymbol{x})p(\boldsymbol{x}+\boldsymbol{\ell})\eta(\boldsymbol{x},\boldsymbol{\ell})d\boldsymbol{x}d\boldsymbol{\ell}\ . \tag{A.11}$$

In order to connect the definition of clustering index with other relevant statistics of the particle system, let's introduce the particle distribution associated with a single particle configuration, which, for conciseness, will be referred to as the instantaneous particle distribution,

$$c_p(\boldsymbol{x}) = \sum_{k=1}^{N}\delta\left[\boldsymbol{x}_k(\omega) - \boldsymbol{x}\right]\ . \tag{A.12}$$

Its average is the particle density

$$\begin{aligned} \mathcal{C}(\boldsymbol{x}) =& \langle\sum_{k=1}^{N}\delta\left[\boldsymbol{x}_k(\omega) - \boldsymbol{x}\right]\rangle = \\ =& N\langle\delta\left[\boldsymbol{x}_1(\omega) - \boldsymbol{x}\right]\rangle = Np_1(\boldsymbol{x})\,, \end{aligned} \tag{A.13}$$

whose volume integral provides the average number of particles in a given domain, (A.5). The instantaneous particle number inside a domain $\mathcal{B}_\ell(\boldsymbol{x})$ centered around $\boldsymbol{x}$ is

$$n\left[\omega;\mathcal{B}_\ell(\boldsymbol{x})\right] = \int_{\mathcal{B}_\ell(\boldsymbol{x})} c_p(\tilde{\boldsymbol{x}})d\tilde{\boldsymbol{x}}\ . \tag{A.14}$$

Under the assumption that the two domains $\mathcal{B}_\ell(\boldsymbol{x})$ and $\mathcal{B}_{\ell'}(\boldsymbol{y})$ are disjoint ($\mathcal{B}_\ell(\boldsymbol{x})\cap\mathcal{B}_{\ell'}(\boldsymbol{y}) = \emptyset$) the number of particle pairs, n_c, with one particle in $\mathcal{B}_\ell(\boldsymbol{x})$ and the other in $\mathcal{B}_{\ell'}(\boldsymbol{y})$ is

$$n_c\left[\omega;\mathcal{B}_\ell(\boldsymbol{x});\mathcal{B}_{\ell'}(\boldsymbol{y})\right] = \int_{\mathcal{B}_\ell(\boldsymbol{x})\times\mathcal{B}_{\ell'}(\boldsymbol{y})} c_p(\tilde{\boldsymbol{x}})c_p(\tilde{\boldsymbol{y}})d\tilde{\boldsymbol{x}}d\tilde{\boldsymbol{y}}\ . \tag{A.15}$$

In general the two sets may have a non empty intersection. In this case we may partition each of them in the form

$$\mathcal{B}_\ell(\boldsymbol{x}) = [\mathcal{B}_\ell(\boldsymbol{x}) \backslash \mathcal{B}_{\ell'}(\boldsymbol{y})] \cup [\mathcal{B}_\ell(\boldsymbol{x}) \cap \mathcal{B}_{\ell'}(\boldsymbol{y})]$$

and

$$\mathcal{B}_{\ell'}(\boldsymbol{y}) = [\mathcal{B}_{\ell'}(\boldsymbol{y}) \backslash \mathcal{B}_\ell(\boldsymbol{x})] \cup [\mathcal{B}_\ell(\boldsymbol{x}) \cap \mathcal{B}_{\ell'}(\boldsymbol{y})] \ ,$$

respectively. The Cartesian product of the two sets can then be rearranged as

$$\begin{aligned}
&\mathcal{B}_\ell(\boldsymbol{x}) \times \mathcal{B}_{\ell'}(\boldsymbol{y}) = \\
&\mathcal{B}_\ell(\boldsymbol{x}) \times \mathcal{B}_{\ell'}(\boldsymbol{y}) \backslash \{[\mathcal{B}_\ell(\boldsymbol{x}) \cap \mathcal{B}_{\ell'}(\boldsymbol{y})] \times [\mathcal{B}_\ell(\boldsymbol{x}) \cap \mathcal{B}_{\ell'}(\boldsymbol{y})]\} \cup \\
&\{[\mathcal{B}_\ell(\boldsymbol{x}) \cap \mathcal{B}_{\ell'}(\boldsymbol{y})] \times [\mathcal{B}_\ell(\boldsymbol{x}) \cap \mathcal{B}_{\ell'}(\boldsymbol{y})]\} = \\
&[\mathcal{B}_\ell(\boldsymbol{x}) \times \mathcal{B}_{\ell'}(\boldsymbol{y})]_{DJ} \cup [\mathcal{B}_\ell(\boldsymbol{x}) \times \mathcal{B}_{\ell'}(\boldsymbol{y})]_J \ ,
\end{aligned}$$

where the last line decomposes the Cartesian product in the joint and disjoint parts.

To avoid counting the same couple twice when dealing with the intersection of the two sets, the expression for the instantaneous number of couples should include a factor $1/2$ in front of the integral over the joint part.

$$\begin{aligned}
n_c\left[\omega; \mathcal{B}_\ell(\boldsymbol{x}); \mathcal{B}_{\ell'}(\boldsymbol{y})\right] = & \\
& \int_{[\mathcal{B}_\ell(\boldsymbol{x}) \times \mathcal{B}_{\ell'}(\boldsymbol{y})]_{DJ}} c_p(\tilde{\boldsymbol{x}}) c_p(\tilde{\boldsymbol{y}}) d\tilde{\boldsymbol{x}} d\tilde{\boldsymbol{y}} + \\
& \frac{1}{2} \int_{[\mathcal{B}_\ell(\boldsymbol{x}) \times \mathcal{B}_{\ell'}(\boldsymbol{y})]_J} c_p(\tilde{\boldsymbol{x}}) c_p(\tilde{\boldsymbol{y}}) d\tilde{\boldsymbol{x}} d\tilde{\boldsymbol{y}} \ .
\end{aligned} \tag{A.16}$$

The correlation of the particle distribution is defined as

$$\begin{aligned}
&\langle c_p(\boldsymbol{x}) c_p(\boldsymbol{y}) \rangle = \langle \sum_{k,r=1}^{N}{}_{r \neq k} \delta\left[\boldsymbol{x}_k(\omega) - \boldsymbol{x}\right] \delta\left[\boldsymbol{x}_r(\omega) - \boldsymbol{y}\right] \rangle = \\
&= N(N-1) \langle \delta\left[\boldsymbol{x}_1(\omega) - \boldsymbol{x}\right] \delta\left[\boldsymbol{x}_2(\omega) - \boldsymbol{y}\right] \rangle = \\
&= N(N-1) p_{12}(\boldsymbol{x}, \boldsymbol{y}) = \frac{(N-1)}{N} \mathcal{C}(\boldsymbol{x}) \mathcal{C}(\boldsymbol{y}) \left[1 + \eta(\boldsymbol{x}, \boldsymbol{y})\right] = \\
&= \mathcal{C}(\boldsymbol{x}) \mathcal{C}(\boldsymbol{y}) \left[1 + \eta(\boldsymbol{x}, \boldsymbol{y})\right] \ ,
\end{aligned} \tag{A.17}$$

where we assume N to be large enough to neglect $1/N$ with respect to 1. Hence the average number of pairs is

$$\begin{aligned}
&\langle n_c\left[\mathcal{B}_\ell(\boldsymbol{x}); \mathcal{B}_{\ell'}(\boldsymbol{y})\right] \rangle = \\
&\int_{[\mathcal{B}_\ell(\boldsymbol{x}) \times \mathcal{B}_{\ell'}(\boldsymbol{y})]_{DJ}} \mathcal{C}(\tilde{\boldsymbol{x}}) \mathcal{C}(\tilde{\boldsymbol{y}}) \left[1 + \eta(\tilde{\boldsymbol{x}}, \tilde{\boldsymbol{y}})\right] d\tilde{\boldsymbol{x}} d\tilde{\boldsymbol{y}} + \\
&\frac{1}{2} \int_{[\mathcal{B}_\ell(\boldsymbol{x}) \times \mathcal{B}_{\ell'}(\boldsymbol{y})]_J} \mathcal{C}(\tilde{\boldsymbol{x}}) \mathcal{C}(\tilde{\boldsymbol{y}}) \left[1 + \eta(\tilde{\boldsymbol{x}}, \tilde{\boldsymbol{y}})\right] d\tilde{\boldsymbol{x}} d\tilde{\boldsymbol{y}} \ .
\end{aligned} \tag{A.18}$$

This allows to introduce the density of pairs with respect to the volume of $\mathcal{B}_\ell(\boldsymbol{x})$,

$$\begin{aligned}\langle \varrho_c \rangle &= \lim_{V_{\mathcal{B}_\ell}\to 0} \frac{\langle n_c \rangle}{V_{\mathcal{B}_\ell}} \\ &= \lim_{V_{\mathcal{B}_\ell}\to 0} \frac{\displaystyle\int_{\mathcal{B}_\ell(\boldsymbol{x})\times\mathcal{B}_{\ell'}(\boldsymbol{y})} f(\tilde{\boldsymbol{x}},\tilde{\boldsymbol{y}})\mathcal{C}(\tilde{\boldsymbol{x}})\mathcal{C}(\tilde{\boldsymbol{y}})\left[1+\eta(\tilde{\boldsymbol{x}},\tilde{\boldsymbol{y}})\right] d\tilde{\boldsymbol{x}}d\tilde{\boldsymbol{y}}}{\displaystyle\int_{\mathcal{B}_\ell(\boldsymbol{x})} d\tilde{\boldsymbol{x}}} \\ &= \int_{\mathcal{B}_{\ell'}(\boldsymbol{y})} f(\boldsymbol{x},\tilde{\boldsymbol{y}})\mathcal{C}(\boldsymbol{x})\mathcal{C}(\tilde{\boldsymbol{y}})\left[1+\eta(\boldsymbol{x},\tilde{\boldsymbol{y}})\right] d\tilde{\boldsymbol{y}}\,,\end{aligned} \tag{A.19}$$

where $f(\boldsymbol{x},\boldsymbol{y}) = 1$ when $(\boldsymbol{x},\boldsymbol{y})$ belong to the disjoined part of the integration domain and $f(\boldsymbol{x},\boldsymbol{y}) = 1/2$ in the complementary set. In fact $f(\boldsymbol{x},\boldsymbol{y}) = 1$ when $\boldsymbol{x} \notin \mathcal{B}_{\ell'}$ and $f(\boldsymbol{x},\boldsymbol{y}) = 1/2$ when $\boldsymbol{x} \in \overset{\circ}{\mathcal{B}}_{\ell'}$.

With $\tilde{\boldsymbol{y}} = \boldsymbol{y} + \tilde{\boldsymbol{\ell}}$ relation (A.19) reads

$$\begin{aligned}&\langle \varrho_c \rangle(\boldsymbol{x},\boldsymbol{y},\ell') = \\ &\mathcal{C}(\boldsymbol{x}) \int_{4\pi} d\hat{\boldsymbol{\ell}} \int_0^{\ell'} f(\boldsymbol{x},\boldsymbol{y}+\tilde{\boldsymbol{\ell}})\mathcal{C}(\boldsymbol{y}+\tilde{\boldsymbol{\ell}}) \left[1+\eta(\boldsymbol{x},\boldsymbol{y}+\tilde{\boldsymbol{\ell}})\right] \tilde{\ell}^2 d\tilde{\ell}\,.\end{aligned} \tag{A.20}$$

We are interested in having $\boldsymbol{x} = \boldsymbol{y}$, i.e. coincident centers of the two spheres $\mathcal{B}_\ell$ and $\mathcal{B}_{\ell'}$ and $f = 1/2$,

$$\langle \varrho_c \rangle = \mathcal{C}(\boldsymbol{x}) \int_{4\pi} d\hat{\boldsymbol{\ell}} \int_0^{\ell'} \frac{1}{2}\,\mathcal{C}(\boldsymbol{x}+\tilde{\boldsymbol{\ell}}) \left[1+\eta(\boldsymbol{x},\tilde{\boldsymbol{\ell}})\right] \tilde{\ell}^2 d\tilde{\ell}\,, \tag{A.21}$$

since we intend to consider the extension, $g(\boldsymbol{x},\ell')$, of the classical concept of radial distribution function [49, 108] to inhomogeneous conditions,

$$g(\boldsymbol{x},\ell') = \frac{d\langle \varrho_c \rangle}{d\ell'} \frac{d\ell'}{d\langle \varrho_c \rangle_0} = \frac{d\langle \varrho_c \rangle}{d\langle \varrho_c \rangle_0}\,, \tag{A.22}$$

where $\langle \varrho_c \rangle_0$ corresponds to a particle distribution with the same concentration $\mathcal{C}$ and vanishing pair correlation η (independently distributed particles in space, characterized by no clustering $K = 0$, (A.11)). Inserting (A.21) in (A.22) we get

$$g(\boldsymbol{x},\ell') = \frac{\displaystyle\int_{4\pi} \mathcal{C}(\boldsymbol{x}+\tilde{\boldsymbol{\ell}}) \left[1+\eta(\boldsymbol{x},\tilde{\boldsymbol{\ell}})\right] d\hat{\boldsymbol{\ell}}}{\displaystyle\int_{4\pi} \mathcal{C}(\boldsymbol{x}+\tilde{\boldsymbol{\ell}}) d\hat{\boldsymbol{\ell}}}\,. \tag{A.23}$$

We note, in passing, that by localizing (A.23) in a specific direction $\hat{\boldsymbol{\ell}}$ we may retain information on the angular dependence by addressing the angular distribution function (see also [68] for this concept in anisotropic homogeneous flows),

$$g(\boldsymbol{x},\ell',\hat{\boldsymbol{\ell}}) = 1 + \eta(\boldsymbol{x},\ell',\hat{\boldsymbol{\ell}})\,. \tag{A.24}$$

The present definition of radial distribution function can be recast in a form better suited for a direct comparison with the classical one used in homogeneous isotropic flows. Let us consider

the number of particle pairs contained in a sphere of radius ℓ. This amounts to considering again (A.18) by taking $\boldsymbol{y} = \boldsymbol{x}$ and $\ell' = \ell$, i.e. $\mathcal{B}_{\ell'}(\boldsymbol{y}) \equiv \mathcal{B}_\ell(\boldsymbol{x})$,

$$\langle n_c \rangle = (4\pi)^2 \int_0^\ell \int_0^\ell \ell_x^2 \ell_y^2 \frac{1}{2} \mathcal{C}(\boldsymbol{x}+\ell_x)\mathcal{C}(\boldsymbol{x}+\ell_y)\left[1+\eta(\boldsymbol{x}+\ell_x, \boldsymbol{x}+\ell_y)\right] d\ell_x d\ell_y \,, \tag{A.25}$$

where the factor is now $f = 1/2$. The derivative of $\langle n_c \rangle$ with respect to the radius of the sphere ℓ reads

$$\frac{d\langle n_c \rangle}{d\ell} = (4\pi)^2 \ell^2 \mathcal{C}(\boldsymbol{x}+\ell) \int_0^\ell \tilde{\ell}^2 \mathcal{C}(\boldsymbol{x}+\tilde{\ell}) \left[1+\eta(\boldsymbol{x}+\ell, \boldsymbol{x}+\tilde{\ell})\right] d\tilde{\ell} \,. \tag{A.26}$$

The corresponding derivative of the number of pairs one would have with same particle density $\mathcal{C}$ and vanishing pair correlation function is

$$\frac{d\langle n_c \rangle_0}{d\ell} = (4\pi)^2 \ell^2 \mathcal{C}(\boldsymbol{x}+\ell) \int_0^\ell \tilde{\ell}^2 \mathcal{C}(\boldsymbol{x}+\tilde{\ell}) d\tilde{\ell} \,. \tag{A.27}$$

Taking the ratio of the two expressions above, by comparison with (A.23), we obtain

$$g(\boldsymbol{x}, \ell) = \frac{d\langle n_c \rangle}{d\ell} \frac{d\ell}{d\langle n_c \rangle_0} = \frac{d\langle n_c \rangle}{d\langle n_c \rangle_0} \,. \tag{A.28}$$

For homogeneous systems the derivative of the number of pairs for zero pair correlation function reduces to

$$\frac{d\langle n_c \rangle_0}{d\ell} = 4\pi\ell^2 \mathcal{C}_0^2 \frac{4\pi\ell^3}{3} = 4\pi\ell^2 \frac{\langle n \rangle^2}{V_{\mathcal{B}_\ell}}, \tag{A.29}$$

where we used that $\mathcal{C}_0 = \langle n \rangle / V_{\mathcal{B}_\ell}$. In conclusion, for homogeneous systems the radial distribution function $g(\ell)$ follows as,

$$g(\ell) = \frac{1}{4\pi\ell^2} \frac{d\langle n_c \rangle}{d\ell} \frac{V_{\mathcal{B}_\ell}}{\langle n \rangle^2} \,. \tag{A.30}$$

Let us show that eq. (A.30) exactly coincides with the definition of radial distribution function provided e.g. in [108] for homogeneous systems. There a system of N particles is considered. Given the position $\boldsymbol{x}_k$ of the k^{th} particle, we denote by $n_k(\ell)$ the number of particles within a ball of radius ℓ centered at $\boldsymbol{x}_k$ excluded the k_{th} particle itself. We call $\mathcal{N}(l) = 1/2 \sum_{k=1}^N n_k(\ell)$ the number of pairs in the whole system whose relative distance is less or equal to ℓ. Clearly

$$\mathcal{N}(l) = \frac{1}{2} N \left(\frac{1}{N} \sum_{k=1}^N n_k(\ell) \right) = \frac{1}{2} N \langle n(\ell) \rangle \,.$$

The number of pairs within a shell of radius ℓ and thickness $d\ell$ is

$$\Delta\mathcal{N}(l) = \frac{1}{2} N \left(\frac{1}{N} \sum_{k=1}^N \Delta n_k(\ell) \right) = \frac{1}{2} N \langle \Delta n(\ell) \rangle \,.$$

The number of pairs in the shell is normalized by the total number of pairs in the system, $\mathcal{N}^T = 1/2N(N-1) \simeq 1/2N^2$,

$$\frac{\Delta\mathcal{N}(l)}{\mathcal{N}^T} = \frac{\langle \Delta n(\ell) \rangle}{N} \,.$$

Let us multiply both members of the equality by $V^T/\Delta V$,

$$\frac{\Delta\mathcal{N}(l)}{\Delta V}\frac{V^T}{\mathcal{N}^T} = \frac{\langle\Delta n(\ell)\rangle}{\Delta V}\frac{V^T}{N} \ .$$

Since $N/V^T = \langle n(l)\rangle/V(\ell) = \mathcal{C}_0$, we have

$$\frac{\Delta\mathcal{N}(l)}{\Delta V}\frac{V^T}{\mathcal{N}^T} = \frac{\langle\Delta n(\ell)\rangle}{\Delta V}\frac{V(\ell)}{\langle n(\ell)\rangle} \ .$$

Let us take the limit for vanishingly small thickness of the shell,

$$\frac{d\mathcal{N}(l)}{dV}\frac{V^T}{\mathcal{N}^T} = \frac{1}{4\pi\ell^2}\frac{d\langle n(\ell)\rangle}{d\ell}\frac{V(\ell)}{\langle n(\ell)\rangle} = \frac{\langle n(\ell)\rangle}{4\pi\ell^2}\frac{d\langle n(\ell)\rangle}{d\ell}\frac{V(\ell)}{\langle n(\ell)\rangle^2} \ .$$

Considering that $\langle n(\ell)\rangle d\langle n(\ell)\rangle = d\langle n_c\rangle$, with $\langle n_c\rangle$ the average number of particles pairs within the ball of radius ℓ, we finally get

$$\frac{1}{4\pi\ell^2}\frac{d\mathcal{N}(l)}{d\ell}\frac{V^T}{\mathcal{N}^T} = \frac{d\mathcal{N}(l)}{dV}\frac{V^T}{\mathcal{N}^T} = \frac{1}{4\pi\ell^2}\frac{d\langle n_c\rangle}{d\ell}\frac{V(\ell)}{\langle n(\ell)\rangle^2} \ .$$

The left hand side of the above expression is the definition of radial distribution function according to e.g. [108], while the right hand side, eq. (A.30), is the form our generalized definition of radial distribution function, eq. (A.28), takes under the assumption of homogeneous particle distribution.

Appendix B

In this appendix we discuss a procedure to derive a continuum particle velocity field in terms of particle velocities in the limit of small τ_p. Starting from equation (7.3), we obtain the fluid velocity along the particle trajectory as the solution of $dx_p/dt = v_p$,

$$u[x_p(t), t] = v_p + \tau_p \dot{v}_p. \tag{B.1}$$

This allows to express the time derivative of the fluid velocity experienced by the particle as

$$\left.\frac{du}{dt}\right|_p = \frac{\partial u}{\partial t} + \dot{x}_p \cdot \nabla u = \dot{v}_p + \tau_p \ddot{v}_p. \tag{B.2}$$

The above expression yields

$$\frac{Du}{Dt} = (u - v_p) \cdot \nabla u + \dot{v}_p + \tau_p \ddot{v}_p, \tag{B.3}$$

which, rearranged as an expression for $\dot{v}_p$ to be inserted in (B.1), provides the fluid velocity as:

$$\begin{aligned} u &= v_p + \tau_p \left[\frac{Du}{Dt} + (v_p - u) \cdot \nabla u - \tau_p \ddot{v}_p \right] \\ &= v_p + \tau_p \frac{Du}{Dt} + \tau_p^2 \left(\dot{v}_p \cdot \nabla u - \ddot{v}_p \right). \end{aligned} \tag{B.4}$$

It follows

$$v_p = u - \tau_p \frac{Du}{Dt} + O(\tau_p^2). \tag{B.5}$$

Since both fluid velocity and acceleration are Eulerian fields, equation (B.5) defines an equivalent Eulerian particle velocity field by neglecting corrections of order τ_p^2,

$$v(x, t) = u(x, t) - \tau_p \frac{Du}{Dt}(x, t). \tag{B.6}$$

In this approximation the particle velocities are treated as a single valued field. In its use, one should be aware of the possible existence of caustics corresponding to a multi-valued particle velocity at the same position [109].

Bibliography

[1] S.B. Pope. *Turbulent flows*. Cambridge Univ Pr, 2000.

[2] R. Borghi, M. Destriau, and G. De Soete. *Combustion and flames: chemical and physical principles*. Editions Technip, 1998.

[3] D. Veynante and L. Vervisch. Turbulent combustion modeling. *Progress in Energy and Combustion Science*, 28(3):193–266, 2002.

[4] F. Picano. *Dynamics of turbulent jets*. PhD thesis, Sapienza, University of Rome, 2007.

[5] H.J. Hussein, S.P. Capp, and W.K. George. Velocity measurements in a high-reynolds-number, momentum-conserving, axisymmetric, turbulent jet. *Journal of Fluid Mechanics*, 258(1):31–75, 1994.

[6] I. Wygnanski, H. Fiedler, and Seattle WA Boeing Scientific Research Labs, Flight Sciences Lab. *Some measurements in the self preserving jet*. Cambridge Univ Press, 1968.

[7] B. Chehroudi, D. Talley, and E. Coy. Visual characteristics and initial growth rates of round cryogenic jets at subcritical and supercritical pressures. *Physics of Fluids*, 14:850, 2002.

[8] G. Troiani. Effect of velocity inflow conditions on the stability of a ch4/air jet-flame. *Combustion and Flame*, 156(2):539–542, 2009.

[9] G. Troiani, M. Marrocco, S. Giammartini, and CM Casciola. Counter-gradient transport in the combustion of a premixed ch4/air annular jet by combined piv/oh-lif. *Combustion and Flame*, 156(3):608–620, 2009.

[10] LF Richardson. Weather prediction by numerical process cambridge university press, 1922.

[11] A.N. Kolmogorov. Dissipation of energy in locally isotropic turbulence [in russian]. In *Dokl. Akad. Nauk SSSR*, volume 32, pages 19–21, 1941.

[12] A.N. Kolmogorov. The local structure of turbulence in incompressible viscous fluid for very large reynolds numbers. In *Dokl. Akad. Nauk SSSR*, volume 30, pages 9–13, 1941.

[13] K. Huang. Statistical mechanics, 2nd. *Edition (New York: John Wiley & Sons)*, 1987.

[14] J.M. Yeomans. *Statistical mechanics of phase transitions*. Oxford University Press, USA, 1992.

[15] O. Redlich and JNS Kwong. On the thermodynamics of solutions. v. an equation of state. fugacities of gaseous solutions. *Chemical Reviews*, 44(1):233–244, 1949.

[16] G. Soave. Equilibrium constants from a modified redlich-kwong equation of state. *Chemical Engineering Science*, 27(6):1197–1203, 1972.

[17] J.O. Valderrama and A. Silva. Modified soave-redlich-kwong equations of state applied to mixtures containing supercritical carbon dioxide. *Korean Journal of Chemical Engineering*, 20(4):709–715, 2003.

[18] K.S. Pitzer. The volumetric and thermodynamic properties of fluids. i. theoretical basis and virial coefficients1. *Journal of the American Chemical Society*, 77(13):3427–3433, 1955.

[19] D.Y. Peng and D.B. Robinson. A new two-constant equation of state. *Industrial & Engineering Chemistry Fundamentals*, 15(1):59–64, 1976.

[20] T. Poinsot, D. Veynante, and S. Candel. Quenching processes and premixed turbulent combustion diagrams. *Journal of Fluid Mechanics*, 228(1):561–606, 1991.

[21] J.F. Driscoll. Turbulent premixed combustion: Flamelet structure and its effect on turbulent burning velocities. *Progress in Energy and Combustion Science*, 34(1):91–134, 2008.

[22] F. Picano and CM Casciola. Small-scale isotropy and universality of axisymmetric jets. *Physics of Fluids*, 19:118106, 2007.

[23] D.R. Dowling. The estimated scalar dissipation rate in gas-phase turbulent jets. *Physics of Fluids A: Fluid Dynamics*, 3:2229, 1991.

[24] D.R. Dowling and P.E. Dimotakis. Similarity of the concentration field of gas-phase turbulent jets. *Journal of Fluid Mechanics*, 218(-1):109–141, 1990.

[25] CD Richards and WM Pitts. Global density effects on the self-preservation behaviour of turbulent free jets. *Journal of Fluid Mechanics*, 254(-1):417–435, 1993.

[26] JC Sautet and D. Stepowski. Dynamic behavior of variable-density, turbulent jets in their near development fields. *Physics of Fluids*, 7:2796, 1995.

[27] J. Eggers and E. Villermaux. Physics of liquid jets. *Reports on progress in physics*, 71: 036601, 2008.

[28] RS Miller, K. Harstad, and J. Bellan. Evaluation of equilibrium and non-equilibrium evaporation models for many-droplet gas-liquid flow simulations. *International journal of multiphase flow*, 24(6):1025–1055, 1998.

[29] RS Miller and J. Bellan. Direct numerical simulation of a confined three-dimensional gas mixing layer with one evaporating hydrocarbon-droplet-laden stream. *Journal of Fluid Mechanics*, 384(1):293–338, 1999.

[30] N. Zong and V. Yang. Cryogenic fluid jets and mixing layers in transcritical and supercritical environments. *Combustion science and technology*, 178(1):193–228, 2006. ISSN 0010-2202.

[31] W. Mayer, A. Schink, C. Schweitzer, and M. Schaffler. Injection and mixing processes in high pressure lox/gh2 rocket combustors. *AIAA*, 1995.

[32] W. Mayer, J. Telaar, R. Braham, G. Schneider, and J. Hussong. Raman measurements of cryogenic injection at supercritical pressure. *Heat and Mass Transfer*, 39(8):709, 2003.

[33] N. Ierardo, A. Congiunti, and C. Bruno. Mixing and combustion in supercritical o2/ch4 liquid rocket injectors. *AIAA*, 1163, 2004.

[34] L. Cutrone, M. Ihme, and M. Herrmann. Modeling of high-pressure mixing and combustion in liquid rocket injectors. In *Proceedings of the Summer Program*, page 269, 2006.

[35] J.C. Oefelein. LES of supercritical LOX-H 2 injection and combustion in a shear-coaxial uni-element rocket. In *41 st AIAA Aerospace Sciences Meeting & Exhibit, Reno, NV*, 2003.

[36] R.S. Miller, K.G. Harstad, and J. Bellan. Direct numerical simulations of supercritical fluid mixing layers applied to heptane-nitrogen. *Journal of Fluid Mechanics*, 436(6):1–39, 2001.

[37] N. A. Okong'o and J. Bellan. Direct numerical simulation of a transitional supercritical binary mixing layer: heptane and nitrogen. *Journal of Fluid Mechanics*, 464:1–34, 2002.

[38] N. Okong'o and J. Bellan. Real-gas effects on mean flow and temporal stability of binary-species mixing layers. *AIAA journal*, 41(12):2429–2443, 2003.

[39] N. A. Okong'o, K. Harstad, and J. Bellan. Direct numerical simulation of o_2/h_2 temporal mixing layers under supercritical conditions. *AIAA journal*, 40(5):914–926, 2002.

[40] W.O.H. Mayer, A.H.A. Schik, B. Vielle, C. Chauveau, I. Gókalp, D.G. Talley, and R.D. Woodward. Atomization and breakup of cryogenic propellants under high-pressure subcritical and supercritical conditions. *Journal of Propulsion and Power*, 14(5):835–842, 1998.

[41] G. Singla, P. Scouflaire, C. Rolon, and S. Candel. Transcritical oxygen/transcritical or supercritical methane combustion. *Proceedings of the Combustion Institute*, 30(2):2921–2928, 2005.

[42] T. Schmitt, L. Selle, B. Cuenot, and T. Poinsot. Large-Eddy Simulation of transcritical flows. *Comptes Rendus Mecanique*, 337(6-7):528–538, 2009. ISSN 1631-0721.

[43] E. Masi and J. Bellan. The subgrid-scale scalar variance under supercritical pressure conditions. *Physics of Fluids*, 23:085101, 2011.

[44] L.C. Selle, N.A. Okong'o, J. Bellan, and K.G. Harstad. Modelling of subgrid-scale phenomena in supercritical transitional mixing layers: an a priori study. *Journal of Fluid mechanics*, 593:57–91, 2007.

[45] E.S. Taskinoglu and J. Bellan. A posteriori study using a dns database describing fluid disintegration and binary-species mixing under supercritical pressure: heptane and nitrogen. *Journal of Fluid Mechanics*, 645(1):211–254, 2010.

[46] E.S. Taşkinoğlu and J. Bellan. Subgrid-scale models and large-eddy simulation of oxygen stream disintegration and mixing with a hydrogen or helium stream at supercritical pressure. *Journal of Fluid Mechanics*, 1(1):1–38, 2011.

[47] S. Elghobashi. On predicting particle-laden turbulent flows. *Applied Scientific Research*, 52(4):309–329, 1994.

[48] S. Elgobashi. An updated classification map of particle-laden turbulent flows. In *IUTAM Symposium on Computational Approaches to Multiphase Flow*, pages 3–10. Springer, 2006.

[49] J. Bec, L. Biferale, M. Cencini, A. Lanotte, S. Musacchio, and F. Toschi. Heavy particle concentration in turbulence at dissipative and inertial scales. *Physical Review Letters*, 98 (8):084502, 2007.

[50] F. Picano, G. Sardina, P. Gualtieri, and CM Casciola. Anomalous memory effects on transport of inertial particles in turbulent jets. *Physics of Fluids*, 22:051705, 2010.

[51] G. Sardina, F. Picano, P. Schlatter, L. Brandt, and C.M. Casciola. Large scale accumulation patterns of inertial particles in wall-bounded turbulent flow. *Flow, turbulence and combustion*, pages 1–14, 2011.

[52] F. Lucci, A. Ferrante, and S. Elghobashi. Modulation of isotropic turbulence by particles of taylor length-scale size. *Journal of Fluid Mechanics*, 650(1):5–55, 2010.

[53] M. Uhlmann. An immersed boundary method with direct forcing for the simulation of particulate flows. *Journal of Computational Physics*, 209(2):448–476, 2005.

[54] F. Odar, Cold Regions Research, and Engineering Laboratory (US). *Forces on a sphere accelerating in a viscous fluid.* Cambridge Univ Press, 1964.

[55] J. Boussinesq. Theorie analytique de la chaleur. *Vol. II*, page 172, 1903.

[56] A.B. Basset. On the motion of a sphere in a viscous liquid. *Philosophical Transactions of the Royal Society of London. A*, 179:43–63, 1888.

[57] M.R. Maxey and J.J. Riley. Equation of motion for a small rigid sphere in a nonuniform flow. *Physics of Fluids*, 26:883, 1983.

[58] F.S. Simmons. *Rocket exhaust plume phenomenology.* Aerospace Press, 2000.

[59] I.M. Kennedy. Models of soot formation and oxidation. *Progress in Energy and Combustion Science*, 23(2):95–132, 1997.

[60] M. Frenklach. Reaction mechanism of soot formation in flames. *Phys. Chem. Chem. Phys.*, 4(11):2028–2037, 2002.

[61] M. Tanahashi, S. Murakami, G.M. Choi, Y. Fukuchi, and T. Miyauchi. Simultaneous ch-oh plif and stereoscopic piv measurements of turbulent premixed flames. *Proceedings of the Combustion Institute*, 30(1):1665–1672, 2005.

[62] J.H. Frank, P.A.M. Kalt, and R.W. Bilger. Measurements of conditional velocities in turbulent premixed flames by simultaneous oh plif and piv. *Combustion and flame*, 116 (1-2):220–232, 1999.

[63] S. Goto and J. C. Vassilicos. Self-similar clustering of inertial particles and zero-acceleration points in fully developed two-dimensional turbulence. *Physics of Fluids*, 18 (11):115103, 2006.

[64] F. Toschi and E. Bodenschatz. Lagrangian properties of particles in turbulence. *Annual Review of Fluid Mechanics*, 41:375–404, 2009.

[65] S. Balachandar and J.K. Eaton. Turbulent dispersed multiphase flow. *Annual Review of Fluid Mechanics*, 42:111–133, 2010.

[66] C. Marchioli and A. Soldati. Mechanisms for particle transfer and segregation in a turbulent boundary layer. *Journal of Fluid Mechanics*, 468(-1):283–315, 2002.

[67] F. Picano, G. Sardina, and CM Casciola. Spatial development of particle-laden turbulent pipe flow. *Physics of Fluids*, 21:093305, 2009.

[68] P. Gualtieri, F. Picano, and CM Casciola. Anisotropic clustering of inertial particles in homogeneous shear flow. *Journal of Fluid Mechanics*, 629, 2009.

[69] J. Chun, D.L. Koch, S.L. Rani, A. Ahluwalia, and L.R. Collins. Clustering of aerosol particles in isotropic turbulence. *Journal of Fluid Mechanics*, 536(1):219–251, 2005.

[70] A. Eidelman, T. Elperin, N. Kleeorin, G. Hazak, I. Rogachevskii, O. Sadot, and I. Sapir-Katiraie. Mixing at the external boundary of a submerged turbulent jet. *Physical Review E*, 79(2):026311, 2009.

[71] A.B. Kostinski and R.A. Shaw. Scale-dependent droplet clustering in turbulent clouds. *Journal of Fluid Mechanics*, 434(-1):389–398, 2001.

[72] P.A. Vaillancourt and MK Yau. Review of particle-turbulence interactions and consequences for cloud physics. *Bulletin of the American Meteorological Society*, 81(2):285–298, 2000.

[73] L.P. Wang and M.R. Maxey. Settling velocity and concentration distribution of heavy particles in homogeneous isotropic turbulence. *Journal of Fluid Mechanics*, 256(-1):27–68, 1993.

[74] L.P. Wang, A.S. Wexler, and Y. Zhou. Statistical mechanical description and modelling of turbulent collision of inertial particles. *Journal of Fluid Mechanics*, 415(-1):117–153, 2000.

[75] E.K. Longmire and J.K. Eaton. Structure of a particle-laden round jet. *Journal of Fluid Mechanics*, 236(-1):217–257, 1992.

[76] A. Eidelman, T. Elperin, N. Kleeorin, G. Hazak, I. Rogachevskii, O. Sadot, and I. Sapir-Katiraie. Mixing at the external boundary of a submerged turbulent jet. *Physical Review E*, 79(2):026311, 2009.

[77] F. Picano, G. Sardina, P. Gualtieri, and CM Casciola. Anomalous memory effects on transport of inertial particles in turbulent jets. *Physics of Fluids*, 22:051705, 2010.

[78] Y. Hardalupas, A. Taylor, and JH Whitelaw. Velocity and particle-flux characteristics of trubulent particle-laden jets. *Proceedings of the Royal Society of London. A. Mathematical and Physical Sciences*, 426(1870):31, 1989.

[79] RS Miller and J. Bellan. Direct numerical simulation of a confined three-dimensional gas mixing layer with one evaporating hydrocarbon-droplet-laden stream. *Journal of Fluid Mechanics*, 384(-1):293–338, 1999.

[80] WP Jones, S. Lyra, and AJ Marquis. Large eddy simulation of evaporating kerosene and acetone sprays. *International Journal of Heat and Mass Transfer*, 53(11-12):2491–2505, 2010.

[81] A. Eidelman, T. Elperin, N. Kleeorin, B. Melnik, and I. Rogachevskii. Tangling clustering of inertial particles in stably stratified turbulence. *Physical Review E*, 81(5):56313, 2010. ISSN 1550-2376.

[82] CJ Sung, CK Law, and RL Axelbaum. Thermophoretic effects on seeding particles in ldv measurements of flames. *Combustion science and technology*, 99(1):119–132, 1994.

[83] JM Bergthorson and PE Dimotakis. Particle velocimetry in high-gradient/high-curvature flows. *Experiments in fluids*, 41(2):255–263, 2006.

[84] A. Stella, G. Guj, J. Kompenhans, M. Raffel, and H. Richard. Application of particle image velocimetry to combusting flows: design considerations and uncertainty assessment. *Experiments in fluids*, 30(2):167–180, 2001.

[85] D. Han and M.G. Mungal. Simultaneous measurements of velocity and ch distributions. part 1:jet flames in co-flow. *Combustion and Flame*, 132:565–590, 2003.

[86] Z. Li and H. Wang. Thermophoretic force and velocity of nanoparticles in the free molecule regime. *Physical Review E*, 70(2):021205, 2004.

[87] CH Chiu, CM Wang, and MC Chiou. Turbulent thermophoresis effect on particle transport processes. *International journal of thermal sciences*, 45(5):475–486, 2006.

[88] A. Majda and J. Sethian. The derivation and numerical solution of the equations for zero mach number combustion. *Combustion science and technology*, 42(3):185–205, 1985.

[89] B. Müller. Low-Mach-number asymptotics of the Navier-Stokes equations. *Journal of engineering mathematics*, 34(1):97–109, 1998. ISSN 0022-0833.

[90] F. Picano, CM Casciola, and K. Hanjalić. Scrutinizing the leray-alpha regularization for les in turbulent axisymmetric free jets. *Direct and Large-Eddy Simulation VII*, pages 169–175, 2010.

[91] N.P. Waterson and H. Deconinck. Design principles for bounded higher-order convection schemes–a unified approach. *Journal of Computational Physics*, 224:182–207, 2007.

[92] C. Willert, C. Hassa, G. Stockhausen, M. Jarius, M. Voges, and J. Klinner. Combined piv and dgv applied to a pressurized gas turbine combustion facility. *Meas. Sci. Technol.*, 17: 1670–1679, 2006.

[93] S.R. Tieszen, T.J. O'Hern, E.J. Weckman, and R.W. Schefer. Experimental study of the effect of fuel mass flux on a 1-m-diameter methane fire and comparison with a hydrogen fire. *Combustion and Flame*, 139(1-2):126–141, 2004.

[94] Y. Shoshin, G. Gorecki, J. Jarosinski, and T. Fodemski. Experimental study of limit lean methane/air flame in a standard flammability tube using particle image velocimetry method. *Combustion and Flame*, 2009.

[95] F. Picano, F. Battista, G. Troiani, and CM Casciola. Dynamics of PIV seeding particles in turbulent premixed flames. *Experiments in Fluids*, pages 1–14, 2010. ISSN 0723-4864.

[96] J. Kim, P. Moin, and R. Moser. Turbulence statistics in fully developed channel flow at low reynolds number. *Journal of Fluid Mechanics*, 177(1):133–166, 1987.

[97] BJ Boersma. Direct numerical simulation of a turbulent reacting jet. *Center for Turbulence Research, Annual Research Briefs*, pages 59–72, 1999.

[98] G. Volpe. Performance of compressible flow codes at low mach numbers. *AIAA journal*, 31(1):49–56, 1993.

[99] K. Huang. Statistical mechanics, 18.3, 1987.

[100] W. Mayer, A. Schik, C. Schweitzer, and M. Schaffler. Injection and mixing processes in high pressure lox/gh2 rocket combustors, aiaa paper no. 96-2620. In *32nd AIAA/ASME/SAE/ASEE Joint Propulsion Conference & Exhibit, Lake Buena Vista, Florida*. –, 1996.

[101] N. Zong, H. Meng, S.Y. Hsieh, and V. Yang. A numerical study of cryogenic fluid injection and mixing under supercritical conditions. *Physics of Fluids*, 16:4248, 2004.

[102] EW Lemmon and RT Jacobsen. Viscosity and thermal conductivity equations for nitrogen, oxygen, argon, and air. *International journal of thermophysics*, 25(1):21–69, 2004.

[103] B. Chehroudi, D. Talley, W. Mayer, R. Branam, JJ Smith, A. Schik, and M. Oschwald. Injection of fluids into supercritical environments, invited review paper, special volume dedicated to supercritical fluids. *Combustion Science and Technology*, 178(1-3):49–100, 2006.

[104] J. Bellan. Supercritical (and subcritical) fluid behavior and modeling: drops, streams, shear and mixing layers, jets and sprays. *Progress in energy and combustion science*, 26(4–6):329–366, 2000.

[105] J. Xia and KH Luo. Direct numerical simulation of diluted combustion by evaporating droplets. *Proceedings of the Combustion Institute*, 32(2):2267–2274, 2009.

[106] KNC Bray, P.A. Libby, and JB Moss. Unified modeling approach for premixed turbulent combustion–part i: General formulation. *Combustion and flame*, 61(1):87–102, 1985.

[107] S. Corrsin and A. Kistler. Free-stream boundaries of turbulent flows. *NACA, Washington DC Rep*, 1244, 1955.

[108] S. Sundaram and L.R. Collins. Collision statistics in an isotropic particle-laden turbulent suspension. Part 1. Direct numerical simulations. *Journal of Fluid Mechanics*, 335:75–109, 1997.

[109] J. Bec, A. Celani, M. Cencini, and S. Musacchio. Clustering and collisions of heavy particles in random smooth flows. *Physics of Fluids*, 17:073301, 2005.

[110] A.M. Steinberg, J.F. Driscoll, and S.L. Ceccio. Measurements of turbulent premixed flame dynamics using cinema stereoscopic piv. *Experiments in Fluids*, 44(6):985–999, 2008.

[111] I. Boxx, M. Stöhr, C. Carter, and W. Meier. Temporally resolved planar measurements of transient phenomena in a partially pre-mixed swirl flame in a gas turbine model combustor. *Combustion and Flame*, 157(8):1510–1525, 2010.

[112] E. Balkovsky, G. Falkovich, and A. Fouxon. Intermittent distribution of inertial particles in turbulent flows. *Physical Review Letters*, 86(13):27902793, 2001.

[113] MW Reeks. The transport of discrete particles in inhomogeneous turbulence. *Journal of aerosol science*, 14(6):729–739, 1983.

[114] M. Righetti and GP Romano. Particle–fluid interactions in a plane near-wall turbulent flow. *Journal of Fluid Mechanics*, 505:93–121, 2004.

[115] D.W.I. Rouson and J.K. Eaton. On the preferential concentration of solid particles in turbulent channel flow. *Journal of Fluid Mechanics*, 428(-1):149–169, 2001.

[116] N. Peters. *Turbulent combustion*. Cambridge University Press, 2000.

[117] T. Poinsot, D. Veynante, and S. Candel. Quenching processes and premixed turbulent combustion diagrams. *Journal of Fluid Mechanics*, 228:561–606, 1991.

[118] S. Corrsin and A.L. Kistler. The free-stream boundaries of turbulent flows. Technical Report 3133, NACA, 1954.

[119] KR Sreenivasan and C. Meneveau. The fractal facets of turbulence. *Journal of Fluid Mechanics*, 173(-1):357–386, 1986.

[120] KNC Bray, P.A. Libby, and JB Moss. Unified modeling approach for premixed turbulent combustion–part i: General formulation. *Combustion and flame*, 61(1):87–102, 1985.

[121] R.J. Kee, F.M. Rupley, E. Meeks, and J.A. Miller. CHEMKIN-III: A FORTRAN chemical kinetics package for the analysis of gas-phase chemical and plasma kinetics. *Sandia National Laboratories Report SAND96-8216*, 1996.

[122] C.K. Law. *Combustion physics*. Cambridge Univ Pr, 2006.

[123] M. Oschwald and A. Schik. Supercritical nitrogen free jet investigated by spontaneous raman scattering. *Experiments in fluids*, 27(6):497–506, 1999.

[124] W. Mayer, A. Schik, M. Schaffler, and H. Tamura. Injection and mixing processes in high-pressure liquid oxygen/gaseous hydrogen rocket combustors. *Journal of Propulsion and Power*, 16(5):823–828, 2000. ISSN 0748-4658.

[125] J. Jimenez and P. Moin. The minimal flow unit in near-wall turbulence. *Journal of Fluid Mechanics*, 225(213-240), 1991.

[126] N. Okong'o and J. Bellan. Turbulence and fluid-front area production in binary-species, supercritical, transitional mixing layers. *Physics of Fluids*, 16:1467, 2004.

[127] O Armas, R Ballesteros, F J Martos, and J R Agudelo. Characterization of light duty Diesel engine pollutant emissions using water-emulsified fuel. *Fuel*, 84:1011–1018, 2005.

[128] David L Daggett, Lars Fucke, Boeing Commercial Airplane, Robert C Hendricks, David J H Eames, and Rolls-royce Corporation. Water Injection on Commercial Aircraft to Reduce Airport Nitrogen Oxides. *Program*, (March), 2010.